國立臺灣大學工學院工程科學及海洋工程學系

碩士論文

Department of Engineering Science and Ocean Engineering

College of Engineering

National Taiwan University

Master Thesis

三維暫態直流電漿火炬模擬

Three-Dimensional Unsteady Simulation of Direct Current Plasma Torch

邱勝瑄

Sheng-Hsuan Chiu

指導教授：趙修武 博士

Advisor: Dr.-Ing. Shiu-Wu Chau

中華民國 110 年 9 月

doi:10.6342/NTU202104312

Abstract

This study develops a numerical framework where a finite volume method is used to discretize the MHD equations consisting of the continuity, momentum, energy, Maxwell's equations and the SST $k-\omega$ turbulence model. A three-dimensional unsteady model is established to simulate a non-transferred direct-current plasma torch equipped with well-type cathode. The investigated torch has a length of 690 mm and a radius of 11 mm. The plasma torch flow is calculated at an inlet flow rate ranging from 100 SLM to 200 SLM and a working current ranging from 100 A to 200 A. The working pressure is 1 atm where the cathode spot is assumed to have a circulation frequency of 1000 Hz. With the help of a regression analysis, the arc length is predicted to grow with $I^{-1.008}$ and $Q^{0.295}$; the mean axial velocity at the outlet is predicted to grow with $I^{-0.754}$ and $Q^{1.691}$; the mean tangential velocity at the outlet is predicted to grow with $I^{-2.061}$ and $Q^{3.491}$; the mean temperature at the outlet is predicted to grow with $I^{-0.415}$ and $Q^{0.427}$.

Keywords: DC Plasma Torch, WTC, Air Plasma, Magnetohydrodynamic Model, Three-dimensional, Unsteady

doi:10.6342/NTU202104312

摘要

本研究使用有限體積法離散基於連續方程式、動量方程式、能量方程式、電磁場方程式及 SST $k-\omega$紊流模型的磁流體動力方程組，建立非傳輸型井式直流電漿火炬的三維暫態數學模型，並開發流場分析程式碼。本研究的火炬長 690 mm，火炬半徑 11 mm，模擬分析工作壓力為 1 大氣壓條件下，流量範圍為 100 SLM 至 200 SLM 間以及工作電流為 100 A 至 200 A 間的空氣電漿火炬特性，並假定陰極弧根以 1000 Hz 頻率環繞火炬內壁移動。本研究利用迴歸分析計算結果顯示電弧長度正比於工作電流的−1.008 次方以及入流流量的 0.295 次方；出口平均軸向速度正比於工作電流的−0.754 次方以及入流流量的 1.691 次方；出口平均旋向速度正比於工作電流的−2.061 次方以及入流流量的 3.491 次方；出口平均溫度正比於工作電流的−0.415 次方以及入流流量的 0.427 次方。

關鍵詞：直流電漿火炬、井式陰極、空氣電漿、磁流體模型、三維、暫態

doi:10.6342/NTU202104312

Contents

Nomenclature v

Acronyms v

Latin Symbols vi

Greek Symbols xi

List of Figures xiii

List of Tables xvii

Chapter 1 Introduction 1

Chapter 2 Method 7

2-1 Governing Equations 7

2-1-1 Magnetohydrodynamic Equations 7

2-1-2 Boundary Conditions 11

(a) Inlet 11

(b) Outlet 11

(c) Wall 12

(d) Symmetry Plane 13

(e) Cathode 13

(f) Anode 14

2-2 Numerical Method 16

2-2-1 Finite Volume Method 16

(a) Transient Term 18

(b) Convection Term 18

(c) Diffusion Term 19

2-2-2 Pressure-correction Equation 21

2-2-3 Wall Distance Calculation 24

doi:10.6342/NTU202104312

2-2-4 Solution Procedure 25
Chapter 3 Study Case 29
3-1 Description of Experiment 29
3-2 Case Description 30
3-3 Computational Domain and Boundary Conditions 31
(a) Cathode 34
(b) Anode 35
3-4 Plasma Properties 38
3-5 Mesh 41
3-6 Grid Dependency 44
Chapter 4 Result and Discussion 48
4-1 Validation 48
4-2 Working Current 52
4-2-1 Time-Averaged Analysis 52
4-2-2 Time History Analysis 62
4-3 Inlet Flow Rate 71
4-3-1 Time-Averaged Analysis 71
4-3-2 Time History Analysis 80
4-4 Discussion 86
Chapter 5 Conclusions and Future Works 95
Appendix 97
References 99

doi:10.6342/NTU202104312

Nomenclature



Acronyms

2D	Two-Dimensional
3D	Three-Dimensional
CDS	Central Differencing Scheme
CFD	Computational Fluid Dynamics
DC	Direct Current
FFT	Fast Fourier Transform
FVM	Finite Volume Method
LTE	Local Thermal Equilibrium
MHD	Magnetohydrodynamic
PDE	Partial Differential Equation
PETSc	the Portable, Extensible Toolkit for Scientific Computation
RTC	Rod-Type Cathode
SIMPLE	Semi-Implicit Method for Pressure Linked Equations
SST	Shear Stress Transport
ultraMPP	ultra-fast Massive Parallel Platform
WTC	Well-Type Cathode

doi:10.6342/NTU202104312

Latin Symbols

A	surface area of a control volume	$[\mathrm{m}^2]$
A_t	tangential component of $\mathbf{A}$	$[\mathrm{T}\cdot\mathrm{m}]$
$\mathbf{A}$	magnetic vector potential	$[\mathrm{T}\cdot\mathrm{m}]$
a_n	equation coefficient of the neighboring cell n	$[-]$
a_p	equation coefficient of the cell p	$[-]$
$\mathbf{a}_f$	surface area vector of the face f	$[\mathrm{m}^2]$
b	current density constant	$[-]$
b_p	source term of the cell p	$[-]$
$\mathbf{b}_p$	source term of the cell p in momentum equations	$[\mathrm{N}/\mathrm{m}^3]$
B_t	tangential component of magnetic flux density	$[\mathrm{T}]$
$\mathbf{B}$	magnetic flux density	$[\mathrm{T}]$
C_f	convective flux	$[-]$
C_p	specific heat capacity	$[\mathrm{J}/\mathrm{kg}\cdot\mathrm{K}]$
C_μ	turbulence model constant	$[-]$
$\mathrm{CD}_{k\omega}$	cross-diffusion constant of turbulence model	$[1/\mathrm{s}^2]$
D_f	diffusive flux	$[-]$
d	wall distance	$[\mathrm{m}]$
$d\mathbf{a}$	surface area vector	$[\mathrm{m}^2]$
$\mathbf{ds}$	displacement vector	$[\mathrm{m}]$
E	total energy	$[\mathrm{J}/\mathrm{kg}]$
E'	logarithmic law offset of turbulence model	$[-]$
E^*	ideal error	$[-]$
E_J	Joule heat	$[\mathrm{W}/\mathrm{m}^3]$

doi:10.6342/NTU202104312

E_R	radiation loss	$[\mathrm{W/m^3}]$
E_ψ	discretization error	$[-]$
E_ψ^n	discretization error of *n*th grid level	$[-]$
$\mathbf{E}$	electric field	$[\mathrm{V/m}]$
e	natural logarithm	$[-]$
F_1	blending function of SST $k-\omega$ turbulence model	$[-]$
F_t	transient term	$[-]$
$\mathbf{F}^\psi$	flux of ψ	$[-]$
f_β	vortex-stretching modification factor	$[-]$
f_{β^*}	free-shear modification factor	$[-]$
$\mathbf{f}_L$	Lorenz force	$[\mathrm{N/m^3}]$
I	working current	$[\mathrm{A}]$
I_t	specified turbulence intensity	$[-]$
J	current density	$[\mathrm{A/m^2}]$
J_{max}	maximum current density at the cathode	$[\mathrm{A/m^2}]$
$\mathbf{J}$	current density vector	$[\mathrm{A/m^2}]$
k	kinetic energy	$[\mathrm{J/kg}]$
k_{in}	kinetic energy at the inlet	$[\mathrm{J/kg}]$
L_{arc}	arc length	$[\mathrm{m}]$
$\dot{m}_f$	mass flow rate at the face f	$[\mathrm{kg/s}]$
$\dot{m}_f'$	correction of mass flow rate at the face f	$[\mathrm{kg/s}]$
$\dot{m}_f^*$	updated mass flow rate at the face f	$[\mathrm{kg/s}]$
$\tilde{\dot{m}}_f'$	mass flow rate calculated from $\tilde{\mathbf{v}}_f'$	$[\mathrm{kg/s}]$
$\dot{m}_{in}$	mass flow rate at the inlet	$[\mathrm{kg/s}]$
$\dot{m}_{out}$	mass flow rate at the outlet	$[\mathrm{kg/s}]$

doi:10.6342/NTU202104312

n_i	outer iteration number	$[-]$
$\mathbf{n}$	unit normal vector of the surface	$[-]$
P_k	production term of k	$[\mathrm{W/m^3}]$
P_ω	production term of ω	$[\mathrm{kg/m^3 \cdot s^2}]$
Pr_t	turbulent Prandtl number	$[-]$
p	pressure	[Pa]
p^*	pressure from the previous iteration	[Pa]
p_f^*	pressure of the face f from the previous iteration	[Pa]
p_p	corrected pressure of the cell p	[Pa]
p_p'	pressure correction of the cell p	[Pa]
p_p^*	pressure of the cell p from the previous iteration	[Pa]
p_n'	pressure correction of the neighboring cell n	[Pa]
Q	inlet flow rate	$[\mathrm{m^3/s}]$
Q_f	coefficient for Rhie-and-Chow interpolation	$[\mathrm{m \cdot s}]$
Re_d	wall-distance Reynolds number	$[-]$
r	distance from the centerline of the torch	[m]
r_c	distance from the center of cathode spot	[m]
S	mean strain rate	$[1/\mathrm{s}]$
S_E	source term in the energy equation	$[\mathrm{W/m^3}]$
S_ψ	source term in the transport equation for ψ	$[-]$
S_{ψ_p}	source term of the cell p in the transport equation for ψ	$[-]$
T_a	anode temperature	[K]
T_c	cathode temperature	[K]
T_in	inlet temperature	[K]
T_t	turbulent time scale	[s]

doi:10.6342/NTU202104312

T^m	mean temperature at the outlet	[K]
T_{w}	wall temperature	[K]
t	time	[s]
u	velocity parallel to wall	[m/s]
u^+	non-dimensional velocity	[−]
u_τ	friction velocity	[m/s]
V	volume	[m³]
V_a	axial velocity	[m/s]
V_C	cathode fall	[V]
V_n	volume of the neighboring cell n	[m³]
V_p	volume of the cell p	[m³]
V_t	tangential velocity	[m/s]
V_a^m	mean axial velocity at the outlet	[m/s]
V_t^m	mean tangential velocity at the outlet	[m/s]
$\mathbf{v}$	velocity vector	[m/s]
$\mathbf{v}^*$	updated velocity vector	[m/s]
$\mathbf{v}_f$	velocity at the face f	[m/s]
$\mathbf{v}_f'$	velocity correction at the face f	[m/s]
$\mathbf{v}_f^*$	updated velocity at the face f	[m/s]
$\tilde{\mathbf{v}}_f'$	velocity correction at the face f	[m/s]
$\mathbf{v}_{\mathrm{in}}$	velocity at the inlet	[m/s]
$\mathbf{v}_p'$	velocity correction of the cell p	[m/s]
$\mathbf{v}_p^*$	updated velocity of the cell p	[m/s]
x	Cartesian coordinate in the axial direction	[m]
$\mathbf{x}_f$	position vector of the face f	[m]

doi:10.6342/NTU202104312

$\mathbf{x}_p$	position vector of the cell p	[m]
y	Cartesian coordinate in the horizontal direction	[m]
y^+	non-dimensional wall distance	[−]
z	Cartesian coordinate in the vertical direction	[m]

doi:10.6342/NTU202104312

Greek Symbols

α_f	linear interpolation factor for the face f	$[-]$
$\boldsymbol{\alpha}_f$	reciprocal of normalized displacement vector	$[1/\mathrm{m}]$
β	constant of turbulence model	$[-]$
β^*	constant of turbulence model	$[-]$
Γ	diffusion coefficient	$[-]$
Γ_f	diffusion coefficient at the face f	$[-]$
γ	blending function for wall treatment	$[-]$
γ_f	Rhie-and-Chow dissipation	$[\mathrm{kg/s}]$
Δt	time step size	$[\mathrm{s}]$
δx	normalized grid size	$[-]$
$\boldsymbol{\delta}$	Kronecker delta	$[-]$
ε	turbulent dissipation rate	$[\mathrm{m^2/s^3}]$
κ	von Kármán constant	$[-]$
λ	thermal conductivity	$[\mathrm{W/m \cdot K}]$
λ_e	effective thermal conductivity	$[\mathrm{W/m \cdot K}]$
μ_0	magnetic permeability in vacuum	$[\mathrm{H/m}]$
μ_m	viscosity	$[\mathrm{Pa/s}]$
μ_t	turbulent viscosity	$[\mathrm{Pa/s}]$
ν	kinematic viscosity	$[\mathrm{m^2/s}]$
ρ	density	$[\mathrm{kg/m^3}]$
ρ_f	density at the face f	$[\mathrm{kg/m^3}]$
ρ_p	density of the cell p	$[\mathrm{kg/m^3}]$
$\sum \widehat{\dot{m}}^*$	normalized mass imbalance	$[-]$

doi:10.6342/NTU202104312

σ	electrical conductivity	$[\mathrm{S/m}]$
σ_k	constant of turbulence model	$[-]$
σ_ω	constant of turbulence model	$[-]$
$\boldsymbol{\tau}$	viscous stress tensor	$[\mathrm{Pa}]$
ϕ	electric potential	$[\mathrm{V}]$
ϕ_{ref}	target voltage drop	$[\mathrm{V}]$
ψ	scalar quantity	$[-]$
ψ_f	scalar quantity at the face f	$[-]$
ψ_p	scalar quantity of the cell p	$[-]$
ψ^m	mean of scalar quantity	$[-]$
ψ^∞	grid-independent solution of scalar quantity	$[-]$
φ	generic function	$[-]$
ω	specific dissipation rate	$[1/\mathrm{s}]$
ω_0	specific dissipation rate specified at the nearest wall cell	$[1/\mathrm{s}]$
$\omega_{\mathbf{A}}$	under-relaxation factor for the magnetic vector potential equations	$[-]$
ω_E	under-relaxation factor for the energy equation	$[-]$
ω_p	under-relaxation factor for the pressure correction equation	$[-]$
ω_t	under-relaxation factor for the turbulence model	$[-]$
$\omega_{\mathbf{v}}$	under-relaxation factor for the momentum equation	$[-]$
ω_ϕ	under-relaxation factor for the electric potential equation	$[-]$
ω_{in}	specific dissipation rate at the inlet	$[1/\mathrm{s}]$

doi:10.6342/NTU202104312

List of Figures

Figure 1.1: (a) RTC transferred plasma torch (b) RTC non-transferred plasma torch (c) WTC non-transferred plasma torch 6

Figure 1.2: Typical voltage traces in the restrike, takeover, steady modes 6

Figure 2.1: Flowchart of the numerical scheme 27

Figure 2.2: Convergence history of the normalized mass imbalance for $I = 140$ A and $Q = 140$ SLM 28

Figure 2.3: Convergence history of voltage drop for $I = 140$ A and $Q = 140$ SLM 28

Figure 3.1: The schematic illustration of the experiment system 29

Figure 3.2: A schematic illustration of the computational domain (3D view) 31

Figure 3.3: A schematic illustration of the computational domain (2D view) 32

Figure 3.4: Dependence of ϕ on I and Q 36

Figure 3.5: Dependence of density on temperature for air plasma 39

Figure 3.6: Dependence of electrical conductivity on temperature for air plasma 39

Figure 3.7: Dependence of thermal conductivity on temperature for air plasma 39

Figure 3.8: Dependence of specific heat capacity on temperature for air plasma 40

Figure 3.9: Dependence of viscosity on temperature for air plasma 40

Figure 3.10: Dependence of radiation loss on temperature for air plasma 40

Figure 3.11: Mesh used to discretize the computational domain (*x* axis is scaled by 0.2) 42

Figure 3.12: Mesh cut at $x = 0$ 42

Figure 3.13: Mesh cut at $y = 0$ 43

Figure 3.14: Dependence of V_a^m on *N* 46

Figure 3.15: Dependence of T^m on *N* 46

doi:10.6342/NTU202104312

Figure 3.16: Dependence of ϕ on N 46
Figure 3.17: Discretization error of V_a^m 47
Figure 3.18: Discretization error of T^m 47
Figure 3.19: Discretization error of ϕ 47
Figure 4.1: The computational domain given in the reference 49
Figure 4.2: The employed 3D computational domain 49
Figure 4.3: Mesh cut at $x = 0$ 50
Figure 4.4: Mesh cut at $y = 0$ 50
Figure 4.5: Comparison of the temperature distributions between electrodes 51
Figure 4.6: Time-averaged axial velocity distributions at $Q = 140$ SLM 55
Figure 4.7: Time-averaged temperature distributions at $Q = 140$ SLM 56
Figure 4.8: Time-averaged electric current density distributions at $Q = 140$ SLM 57
Figure 4.9: Time-averaged tangential magnetic field distributions at $Q = 140$ SLM 58
Figure 4.10: Centerline profile of time-averaged axial velocity at $Q = 140$ SLM 59
Figure 4.11: Centerline profile of time-averaged temperature at $Q = 140$ SLM 59
Figure 4.12: Centerline profile of time-averaged electric current density at $Q = 140$ SLM 60
Figure 4.13: Outlet profile of time-averaged axial velocity at $Q = 140$ SLM 60
Figure 4.14: Outlet profile of time-averaged tangential velocity at $Q = 140$ SLM 61
Figure 4.15: Outlet profile of time-averaged temperature at $Q = 140$ SLM 61
Figure 4.16: Time history of the mean axial velocity at the outlet at $Q = 140$ SLM 64
Figure 4.17: Time history of the mean tangential velocity at the outlet at $Q = 140$ SLM 65
Figure 4.18: Time history of the mean temperature at the outlet at $Q = 140$ SLM 66

doi:10.6342/NTU202104312

Figure 4.19: Time history of voltage drop at $Q = 140$ SLM 67
Figure 4.20: Fast Fourier transform of voltage drop at $Q = 140$ SLM.....68
Figure 4.21: Temperature distributions inside the torch of different cross sections 69
Figure 4.22: Electric current density distributions inside the torch of different cross sections 70
Figure 4.23: Time-averaged axial velocity distributions at $I = 140$ A.....73
Figure 4.24: Time-averaged temperature distributions at $I = 140$ A 74
Figure 4.25: Time-averaged electric current density distributions at $I = 140$ A.....75
Figure 4.26: Time-averaged tangential magnetic field distributions at $I = 140$ A....76
Figure 4.27: Centerline profile of time-averaged axial velocity at $I = 140$ A 77
Figure 4.28: Centerline profile of time-averaged temperature at $I = 140$ A.....77
Figure 4.29: Centerline profile of time-averaged electric current density at $I = 140$ A 78
Figure 4.30: Outlet profile of time-averaged axial velocity at $I = 140$ A.....78
Figure 4.31: Outlet profile of time-averaged tangential velocity at $I = 140$ A.....79
Figure 4.32: Outlet profile of time-averaged temperature at $I = 140$ A 79
Figure 4.33: Time history of the mean axial velocity at the outlet at $I = 140$ A 81
Figure 4.34: Time history of the mean tangential velocity at the outlet at $I = 140$ A 82
Figure 4.35: Time history of the mean temperature at the outlet at $I = 140$ A.....83
Figure 4.36: Time history of voltage drop at $I = 140$ A 84
Figure 4.37: Fast Fourier transform of voltage drop at $I = 140$ A.....85
Figure 4.38: Axial velocity comparison of centerline profile predicted by two models 89
Figure 4.39: Temperature comparison of centerline profile predicted by two models 90

doi:10.6342/NTU202104312

Figure 4.40: Comparison of arc length predicted by two models under different conditions.....91
Figure 4.41: Regression correlation of arc length.....91
Figure 4.42: Comparison of the mean axial velocity at the outlet predicted by two models under different conditions 92
Figure 4.43: Regression correlation of the mean axial velocity at the outlet 92
Figure 4.44: Comparison of the mean tangential velocity at the outlet predicted by two models under different conditions 93
Figure 4.45: Regression correlation of the mean tangential velocity at the outlet 93
Figure 4.46: Comparison of the mean temperature at the outlet predicted by two models under different conditions 94
Figure 4.47: Regression correlation of the mean temperature at the outlet.....94

doi:10.6342/NTU202104312

List of Tables

Table 2.1: Boundary conditions 15

Table 2.2: The terms arising in the integral form of governing equations 17

Table 2.3: Coefficients of the linearized algebraic equation 20

Table 3.1: The modelled conditions 30

Table 3.2: Dimension of computational domain 32

Table 3.3: Boundary conditions of each boundary 32

Table 3.4: Boundary conditions for different inlet flow rates 33

Table 3.5: Boundary conditions for different working currents 33

Table 3.6: Characteristics of cathode material 35

Table 3.7: Target voltage drop for $I = 140$ A 36

Table 3.8: Target voltage drop for $Q = 140$ SLM 36

Table 3.9: Arc length of $I = 140$ A 37

Table 3.10: Arc length of $Q = 140$ SLM 37

Table 4.1: Boundary conditions 49

doi:10.6342/NTU202104312

Chapter 1 Introduction

Direct current (DC) plasma torch is one of thermal plasma devices, and there are several parameters, such as working gas, flow rate, torch design and electrode materials affecting the torch performance. According to the anode position, the DC plasma torches are categorized into the transferred and non-transferred ones. As shown in Figure 1.1, the electrode positions of the non-transferred plasma torch are inside the torch, whereas one electrode position of the transferred one is outside the torch. The cathode design is divided into rod-type cathode (RTC) and well-type cathode (WTC) which are also shown in Figure 1.1. In general, DC plasma torch uses electric arc as the main energy source to accelerate the flow and elevate the temperature. Via the interaction between arc columns and the working gas, high-temperature plasma jets are created for some industrial applications, such as plasma spraying and plasma cutting, which mostly take place in atmospheric condition. However, a closed environment is required to prevent gaseous products in waste destruction from leaking, and the working pressure may extremely alter in the application process. Therefore, the related flow characteristics that influence the efficiency of the torch are difficult to be observed and measured because of a closed environment featured with high temperature [1]. The numerical simulation becomes a feasible method to investigate different designs of DC plasma torches for enhancing the performance.

doi:10.6342/NTU202104312

During the past few decades, computational fluid dynamics (CFD) has been applied to the modeling of thermal plasma. Numerical simulation serves as a powerful approach in analyzing complicated thermal fluid phenomena in the arc discharge zone. In studying DC plasma torch, numerous works have been conducted with two-dimensional (2D) axisymmetric modeling in order to simplify the three-dimensional (3D) problems [2-9], and the axisymmetric assumption usually results in circumferentially uniform arc attachment at the electrodes. However, the experimental observations indicated that the arc root is only attached on a small region of the electrode surface [10]. To simulate this behavior, a method using fictitious anode to modify 2D modeling was developed [6], but it was unable to predict the 3D flow within the torch. Recently, owing to the rapid development of computing power, 3D modeling has been used for capturing the dynamics of the arc inside DC plasma torch where the interaction of the electromagnetic force and the flow drag was studied [1, 4, 11-15]. Based on the observations of the anode attachment movement and the voltage drop signal over time, there are three distinctive operating modes of the arc in the plasma torch equipped with RTC: the steady mode, the takeover mode and the restrike mode [16, 17] which are shown in Figure 1.2. The arc in the steady mode has a fixed length, and the jet has a laminar-like appearance rather than a turbulent one [16]. In the restrike mode, the major restrikes labelled 1 in Figure 1.2 indicate the diffused arc root near a

doi:10.6342/NTU202104312

boundary layer with higher temperature that contributes to the lower voltage. Besides, the major restrikes labelled 2 in Figure 1.2 indicate the sharp attachment of the arc throughout a thicker boundary layer [16]. Compared to the instability of the restrike mode, the takeover mode delivers a more stable behavior via the well-defined arc fluctuations and the heat is adequately distributed in anode [17].

In the numerical simulation, there were several magnetohydrodynamic (MHD) models proposed to study the thermal and flow characteristics of the DC plasma torch [15, 18]. A steady 3D model was developed to simulate the temperature and velocity fields in the DC plasma torch equipped with RTC, and the arc length and arc core radius are adjusted to match the torch power corresponding to the given working current and gas flow [11]. This method has a disadvantage that the arc fluctuation is fully ignored, so the time-dependent 3D model is a better choice to describe the dynamic arc motion in the plasma torch. The local thermal equilibrium (LTE), or thermodynamic equilibrium was commonly assumed in thermal plasma modeling where the heavy-particle temperature is almost equal to the electron temperature because of a high collision frequency [19]. The non-LTE model shows that there are nontrivial non-equilibrium regions near the anode surface, and the simulation results show good agreement with experimental observations [14, 20]. In addition to the non-LTE model, there was a simple modified LTE model without solving the electron energy equation

doi:10.6342/NTU202104312

to obtain the nominal electron temperature and to achieve a comparable accuracy to the non-LTE model [13]. These models usually mainly focused on the study of non-transferred DC plasma torch equipped with RTC. The comparison of the RTC and WTC design via a 2D axisymmetric LTE model indicated that the turbulent effects are much stronger in WTC [3]. A steady 2D axisymmetric non-LTE simulation considering the chemical reactions in a WTC plasma torch showed that LTE assumption is valid in the hot plasma core and in the vicinity of the electrodes [7]. A 3D transient model for describing the internal plasma flow coupled with a 2D stationary model for describing the external plasma jet was proposed where a favorable agreement with the experiment was found [12]. The study suggests that the 3D transient formulations are required for describing the real behavior of arc discharge inside the torch, while the 2D stationary approaches are able to predict the time-averaged plasma characteristics outside the torch because of its simplicity and rapidness in the computation [4].

Although numerous works have been done to date, there are still relatively little researches conducted based on a 3D modeling of DC plasma torch with a WTC design. The purpose of this study is to develop a 3D unsteady numerical code simulating the DC plasma torch with WTC design under the LTE assumption. The MHD equations, the discretization and the solution procedure of the numerical scheme are discussed in Chapter 2. The study cases including the experimental setup, the calculation domain

doi:10.6342/NTU202104312

and the mesh construction are given in Chapter 3. The results and discussion are continued in Chapter 4, and the conclusion is given in Chapter 5.



doi:10.6342/NTU202104312

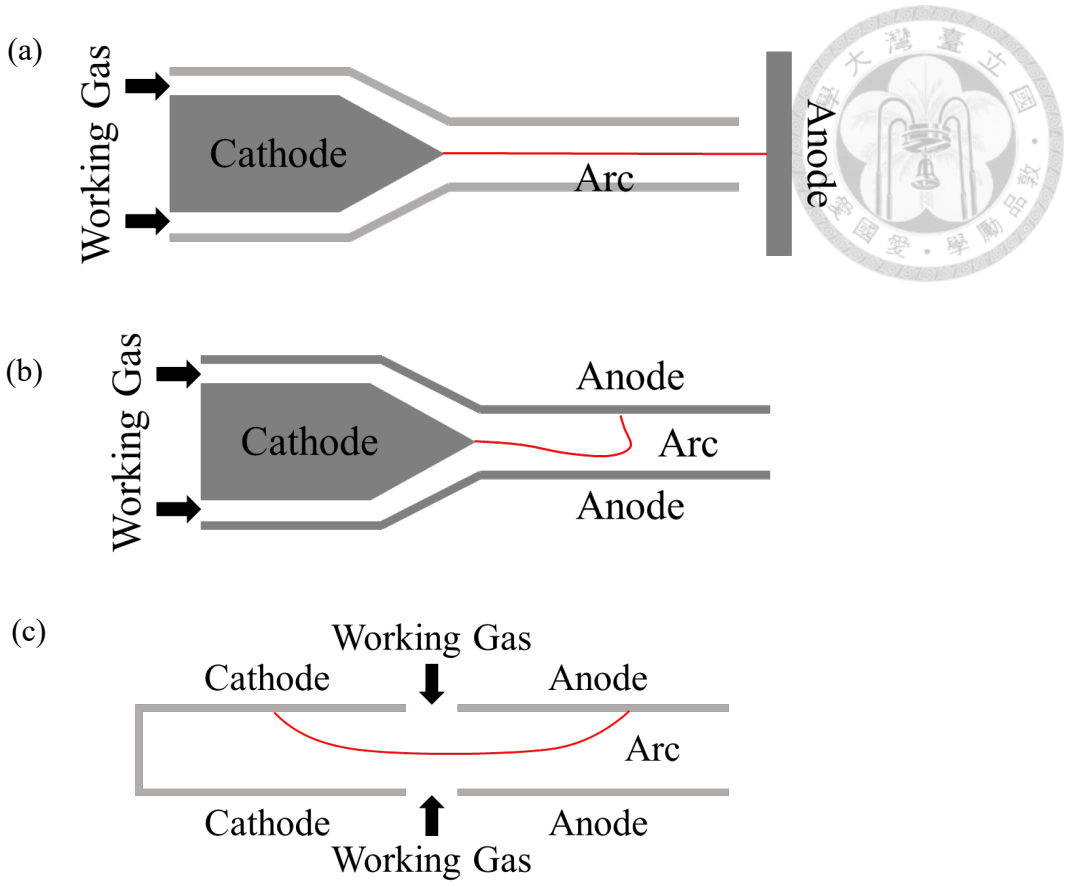


Figure 1.1: (a) RTC transferred plasma torch (b) RTC non-transferred plasma torch

(c) WTC non-transferred plasma torch

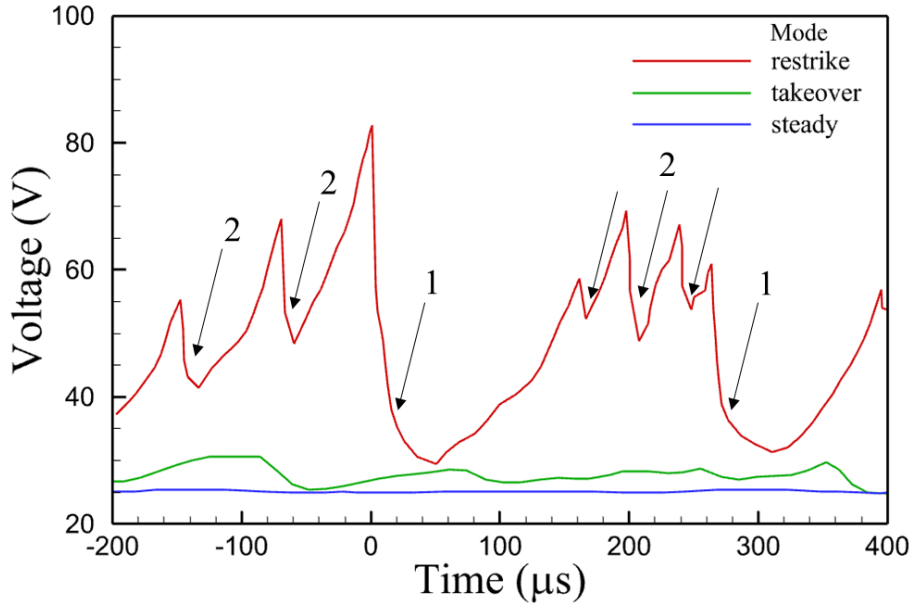


Figure 1.2: Typical voltage traces in the restrike, takeover, steady modes [16]

doi:10.6342/NTU202104312

Chapter 2 Method

2-1 Governing Equations

2-1-1 Magnetohydrodynamic Equations

In this study, thermal plasma modelling is adopted because of high electron density and high collision frequency arising in DC plasma torches. The mathematical model of thermal plasma is based on a set of partial differential equations (PDEs) which correlate the velocity, pressure, temperature, turbulence and electromagnetic fields. The examined plasma is considered an electrically conducting fluid that follows the equations of fluid dynamics and Maxwell's equations [21]. The fluid models are described by the Navier-Stokes equations obeying conservation laws, namely:

$$\frac{\partial \rho}{\partial \mathrm{t}} + \nabla \cdot (\rho \mathbf{v}) = 0, \tag{1}$$

$$\frac{\partial (\rho \mathbf{v})}{\partial t} + \nabla \cdot (\rho \mathbf{v}\mathbf{v} + p\boldsymbol{\delta} - \boldsymbol{\tau}) = \mathbf{f}_L, \tag{2}$$

where ρ denotes the density, $\mathbf{v}$ the temporally-averaged velocity, t the time, p the pressure, $\boldsymbol{\delta}$ the Kronecker delta, $\boldsymbol{\tau}$ the viscous stress tensor and $\mathbf{f}_L$ the Lorenz force.

In a DC plasma torch, the Joule heat and electromagnetic force result in an obvious acceleration of the fluid. The flow velocity in the torch can grow from 10 m/s to 1000 m/s. Consequently, turbulent flow is more appropriate than laminar flow for describing the examined plasma flow [5, 8, 22, 23]. A shear stress transport (SST) two-equation $k-\omega$ turbulence model is then adopted in this study, and it is combing a $k-\omega$

doi:10.6342/NTU202104312

turbulence model near the wall and a $k-\varepsilon$ turbulence model in the far field [5]. The governing equations for the kinetic energy k and the specific dissipation rate ω are [24-27]

$$\frac{\partial(\rho k)}{\partial t}+\nabla\cdot(\rho\mathbf{v}k)=\nabla\cdot[(\mu_m+\sigma_k\mu_t)\nabla k]+P_k-\rho\beta^* f_{\beta^*}k\omega, \tag{3}$$

$$\frac{\partial(\rho\omega)}{\partial t}+\nabla\cdot(\rho\mathbf{v}\omega)=\nabla\cdot[(\mu_m+\sigma_\omega\mu_t)\nabla\omega]+P_\omega-\rho\beta f_\beta\omega^2, \tag{4}$$

where μ_m is the material viscosity, μ_t the turbulent viscosity, σ_k and σ_ω the model constants, P_k and P_ω the production terms, β^* and β the model constants, f_{β^*} the free-shear modification factor and f_β the vortex-stretching modification factor. The turbulent viscosity μ_t is then calculated by

$$\mu_t=\rho k T_t, \tag{5}$$

where T_t denotes the turbulent time scale [28]. The essential blended function F_1 of the SST $k-\omega$ turbulence model which controls the contribution of $k-\omega$ model and $k-\varepsilon$ model is defined as

$$F_1=\tanh\left(\left[\min\left(\max\left(\frac{\sqrt{k}}{\beta^* d\omega},\frac{500\nu}{d^2\omega}\right),\frac{2k}{d^2\mathrm{CD}_{k\omega}}\right)\right]^4\right), \tag{6}$$

where d represents the wall distance, ν the kinematic viscosity and $\mathrm{CD}_{k\omega}$ the cross-diffusion constant. The abovementioned model constants are given in Appendix I.

The LTE approximation is acceptable under high collision frequency, and it assumes that the kinetic energy of the species in space is able to be described by a single temperature T. Therefore, the energy equation is showed below:

doi:10.6342/NTU202104312

$$\frac{\partial(\rho E)}{\partial t} + \nabla \cdot (\rho \mathbf{v} E) = \nabla \cdot (\lambda_e \nabla T) - \nabla \cdot [\mathbf{v}(p\boldsymbol{\delta} - \boldsymbol{\tau})] + S_E, \quad (7)$$

$$E = C_p T + \frac{|\mathbf{v}|^2}{2}, \quad (8)$$

$$\lambda_e = \lambda + \frac{\mu_t C_p}{Pr_t}, \quad (9)$$

$$S_E = E_J - E_R, \quad (10)$$

where E represents the total energy, λ the thermal conductivity, C_p the specific heat capacity, λ_e the effective thermal conductivity and Pr_t the turbulent Prandtl number [29]. The source term S_E in the energy equation is the summation of Joule heat E_J and radiation loss E_R.

The main thrust to accelerate flow in a DC plasma torch is the electromagnetic force contributed by the current and self-induced magnetic field. Thus, the Maxwell's equations are introduced as

$$\nabla \cdot \mathbf{J} = 0, \quad (11)$$

$$\nabla \cdot \mathbf{B} = 0, \quad (12)$$

$$\nabla \times \mathbf{E} = -\frac{\partial \mathbf{B}}{\partial \mathrm{t}}, \quad (13)$$

$$\nabla \times \mathbf{B} = \mu_0 \mathbf{J}, \quad (14)$$

$$\mathbf{J} = \sigma(\mathbf{E} + \mathbf{v} \times \mathbf{B}), \quad (15)$$

where $\mathbf{J}$ denotes the current density, σ the electrical conductivity, $\mathbf{E}$ the electric field, $\mathbf{B}$ the magnetic flux density and μ_0 the vacuum magnetic permeability given in Appendix II. The Lorenz force and the Joule heat used in Eqs. (2) and (7) are expressed

doi:10.6342/NTU202104312

as

$$\mathbf{f}_{\mathrm{L}} = \mathbf{J} \times \mathbf{B}, \tag{16}$$

$$E_J = \mathbf{J} \cdot (\mathbf{E} + \mathbf{v} \times \mathbf{B}). \tag{17}$$

By introducing the electric potential ϕ and the magnetic vector potential $\mathbf{A}$, the electric field $\mathbf{E}$ and magnetic flux density $\mathbf{B}$ is then expressed in terms of these two potentials as

$$\mathbf{E} = -\nabla\phi - \frac{\partial \mathbf{A}}{\partial t}, \tag{18}$$

$$\mathbf{B} = \nabla \times \mathbf{A}. \tag{19}$$

Then, the governing equation for electric potential derived from Eqs. (11), (15), (18) and (19) is expressed as

$$\nabla \cdot (\sigma \nabla \phi) = \nabla \cdot \sigma \left(-\frac{\partial \mathbf{A}}{\partial t} + \mathbf{v} \times \nabla \times \mathbf{A} \right), \tag{20}$$

and, similarly, the governing equation for magnetic vector potential derived from Eqs. (14), (15), (18) and (19) is expressed as

$$\frac{\partial (\sigma \mathbf{A})}{\partial t} + \frac{\nabla^2 \mathbf{A}}{\mu_0} = -\sigma (\nabla \phi - \mathbf{v} \times \nabla \times \mathbf{A}). \tag{21}$$

doi:10.6342/NTU202104312

2-1-2 Boundary Conditions

Boundary conditions are mathematically necessary to solve PDEs that describe the physical phenomena. Dirichlet and Neumann conditions are two boundary conditions frequently used to solve PDEs. Generally, the Dirichlet condition states the value of variable on the boundary, and the Neumann condition describes the gradient of variable on the boundary. In the following sections, these two types of boundary conditions are both used.

(a) Inlet

The dependent variable fields $\mathbf{v}$, k, ω, T are explicitly assigned on the inlet boundary as

$$\mathbf{v}_{\text{in}} = \mathbf{v}_{given}, \tag{22}$$

$$k_{\text{in}} = \frac{3}{2}(I_t|\mathbf{v}_{\text{in}}|)^2, \tag{23}$$

$$\omega_{\text{in}} = \frac{\rho k_{\text{in}}}{(\mu_t/\mu_m)_{\text{in}}\,\mu_m}, \tag{24}$$

$$T_{\text{in}} = T_{given}, \tag{25}$$

where I_t denotes the specified turbulence intensity and $(\mu_t/\mu_m)_{\text{in}}$ the turbulent viscosity ratio at the inlet. In addition, the inlet boundary for the pressure p is using a Neumann condition of zero gradient.

(b) Outlet

The outlet boundary is a Neumann condition. The derivatives of dependent

doi:10.6342/NTU202104312

variable fields, e.g., $\mathbf{v}$, p, k, ω, T normal to the outlet boundary are set to zero.

(c) Wall

A no-slip condition is adopted on the wall, and the flow velocity is set to zero. The wall boundary is a main source to create the vorticity, so an accurate prediction of flow and turbulence near the wall is important. The inner flow region near the wall is subdivided into three sublayers: viscous sublayer, buffer layer and logarithmic layer. To describe the wall function, a non-dimensional wall distance y^+ and a non-dimensional velocity u^+ are described in the following equations:

$$y^+ = \frac{d\rho u_\tau}{\mu_m}, \tag{26}$$

$$u^+ = \frac{u}{u_\tau}, \tag{27}$$

where d is the wall distance, u the velocity parallel to wall and u_τ the friction velocity. The sublayer closest to the wall, or viscous sublayer, is practically laminar and dominated by viscous effects. In this sublayer, experimental evidences show that the velocity profile follows the relation below when $0 \le y^+ \le 5$:

$$u^+ = y^+. \tag{28}$$

The turbulent logarithmic layer, or overlapping layer, is simultaneously dominated by viscous and turbulent effects, and the logarithmic law is valid when $30 \le y^+ \le 500$. The logarithmic law relation is expressed as below:

$$u^+ = \frac{1}{\kappa}\ln(E'y^+), \tag{29}$$

doi:10.6342/NTU202104312

where κ is the von Kármán constant and E' the offset. The buffer layer is a transitional layer between these two layers. In this study, a blending function γ is used to approximate the friction velocity u_τ:

$$\gamma = e^{\frac{-Re_d}{11}}, \tag{30}$$

$$Re_d = \frac{\sqrt{k}d}{\nu}, \tag{31}$$

$$u_\tau = \gamma \frac{\mu_m |u|}{\rho d} + (1-\gamma) C_\mu^{\frac{1}{4}} k^{\frac{1}{2}}, \tag{32}$$

where Re_d is the wall-distance Reynolds number and C_μ the turbulence model constant. The blending function is also adopted to determine the near-wall turbulence properties [25, 30, 31]:

$$P_k = \mu_t S^2 + (1-\gamma) \frac{1}{\mu_m} \left(\rho u_* \frac{u}{u^+}\right)^2 \frac{\partial u^+}{\partial y^+}, \tag{33}$$

$$\omega_0 = \gamma \frac{6\nu}{\beta d^2} + (1-\gamma) \frac{u_\tau}{\sqrt{\beta^*}\kappa d}, \tag{34}$$

where S is the mean strain rate and ω_0 the specific dissipation rate specified at the nearest wall cell. In addition, a zero-gradient condition of k, ω and p is applied on walls, and wall temperature is prescribed at wall.

(d) Symmetry Plane

The velocity component and gradients of other variables normal to the symmetry plane are set to zero.

(e) Cathode

The cathode region is a boundary only applied to the electromagnetic field, and

doi:10.6342/NTU202104312

the cathode region is treated as a wall boundary for other variables. The cathode spot is assumed to be a circle region on the torch surface. The electric current density at the cathode spot is distributed as

$$J(r_c) = J_{max} e^{-br_c}, \tag{35}$$

where J_{max} is the maximum value of the current density, b a given constant, and r_c the distance from the center of cathode spot. The values of J_{max} and b are taken from [2]. In an unsteady simulation, the cathode spot travels with a given frequency on the inner torch wall.

(f) Anode

A Dirichlet boundary condition is used to describe the electric potential of anode that is set to zero, and the anode is treated as a wall boundary for other variables. In an unsteady simulation, the anode position is decided by the working current and inflow rate of gas, and the details are discussed in Chapter 3.

The boundary conditions for all fields are summarized in Table 2.1. A zero-gradient condition is used at the inlet, outlet and wall for the electric potential ϕ. In this study, it is assumed that the external magnetic field has no effect on the self-induced magnetic field arising inside the torch. Therefore, the normal component of the magnetic field $\mathbf{B}$, i.e., $\nabla \times \mathbf{A}$, is set to zero at all boundaries, that is A_t, i.e., the tangential component of $\mathbf{A}$, is set to zero.

doi:10.6342/NTU202104312

Table 2.1: Boundary conditions

Boundary	Inlet	Outlet	Wall	Cathode	Anode
$\mathbf{v}$	$\mathbf{v}_{\text{in}}$	$\nabla\mathbf{v}\cdot\mathbf{n}=\mathbf{0}$	$\mathbf{0}$		
p	$\nabla p\cdot\mathbf{n}=0$				
k	k_{in}	$\nabla k\cdot\mathbf{n}=0$			
ω	ω_{in}	$\nabla\omega\cdot\mathbf{n}=0$			
T	T_{in}	$\nabla T\cdot\mathbf{n}=0$	T_{w}	T_{c}	T_{a}
ϕ	$\nabla\phi\cdot\mathbf{n}=0$			Eq. (35)	0
$\mathbf{A}$	$A_t=0$				

doi:10.6342/NTU202104312

2-2 Numerical Method

2-2-1 Finite Volume Method

Finite volume method (FVM) is a kind of discretization method for solving PDEs. In the FVM, the computational domain is divided into a finite number of volumes called control volumes or cells [32]. The governing equations are able to be written in the generic form of transport equation. By integrating the generic transport equation over a control volume and applying Gauss divergence theorem, the integral form of the transport equation for a scalar quantity ψ is obtained:

$$\frac{d}{dt}\int_V \rho\psi dV + \int_A \rho\mathbf{v}\psi \cdot d\mathbf{a} = \int_A \Gamma\nabla\psi \cdot d\mathbf{a} + \int_V S_\psi dV, \tag{36}$$

where V denotes the control volume, A the surface area of the control volume, $\mathbf{a}$ the surface area vector, Γ and S_ψ the generic diffusion coefficient and source term, respectively. The equation can be also represented as

$$\int_V F_t dV + \int_A \mathbf{C}_f \cdot d\mathbf{a} = \int_A \mathbf{D}_f \cdot d\mathbf{a} + \int_V S_\psi dV, \tag{37}$$

where F_t is the transient term, $\mathbf{C}_f$ the convective flux, $\mathbf{D}_f$ the diffusive flux and S_ψ the source term. The transient term F_t signifies the time rate of change of ψ inside the control volume. The source term S_ψ corresponds to the production or consumption of the scalar quantity ψ in the control volume. The governing equations given in Chapter 2-1-1 can be expressed in the form of Eq. (37), and their corresponding terms are shown in Table 2.2.

doi:10.6342/NTU202104312

Table 2.2: The terms arising in the integral form of governing equations

Conservation	ψ	Transient	Convection	Diffusion	Source
Total mass	1	$\frac{\partial \rho}{\partial t}$	$\nabla \cdot (\rho \mathbf{v})$	0	0
Momentum	$\mathbf{v}$	$\frac{\partial (\rho \mathbf{v})}{\partial t}$	$\nabla \cdot (\rho \mathbf{v}\mathbf{v})$	$\nabla \cdot (\boldsymbol{\tau})$	$\mathbf{f}_{\mathrm{L}} - \nabla \cdot (\mathrm{p}\boldsymbol{\delta})$
Turbulent kinetic energy	k	$\frac{\partial (\rho k)}{\partial t}$	$\nabla \cdot (\rho \mathbf{v} k)$	$\nabla \cdot [(\mu_m + \sigma_k \mu_t) \nabla k]$	$P_k - \rho \beta^* f_{\beta^*} k\omega$
Specific dissipation rate	ω	$\frac{\partial (\rho \omega)}{\partial t}$	$\nabla \cdot (\rho \mathbf{v} \omega)$	$\nabla \cdot [(\mu_m + \sigma_\omega \mu_t) \nabla \omega]$	$P_\omega - \rho \beta f_\beta \omega^2$
Total energy	E	$\frac{\partial (\rho E)}{\partial t}$	$\nabla \cdot (\rho \mathbf{v} E)$	$\nabla \cdot (\lambda_e \nabla T)$	$E_J - E_R - \nabla \cdot [\mathbf{v}(\mathrm{p}\boldsymbol{\delta} - \boldsymbol{\tau})]$
Electrodynamic potential	ϕ	0	0	$\nabla \cdot (\sigma \nabla \phi)$	$\nabla \cdot \sigma \left(\frac{\partial \mathbf{A}}{\partial t} - \mathbf{v} \times \nabla \times \mathbf{A} \right)$
Magnetic vector potential	$\mathbf{A}$	$\frac{\partial (\sigma \mathbf{A})}{\partial t}$	0	$-\nabla \cdot \left(\frac{1}{\mu_0} \nabla \mathbf{A} \right)$	$-\sigma(\nabla \phi - \mathbf{v} \times \nabla \times \mathbf{A})$

Gaussian quadrature is used to calculate the surface integral in the transport equation that is approximated by the product of the value at the face center and the face area:

$$\int_A \mathbf{F}^{\psi} \cdot d\mathbf{a} \approx \sum_f \mathbf{F}_f^{\psi} \cdot \mathbf{a}_f, \tag{38}$$

where $\mathbf{F}^{\psi}$ denotes the convective or the diffusive flux of ψ and $\mathbf{a}_f$ the surface area vector of the face f.

The volume integral in the transport equation is approximated by the product of the value at the cell center and the volume of the cell:

$$\int_V S_{\psi} dV \approx S_{\psi_p} V_p, \tag{39}$$

doi:10.6342/NTU202104312

where S_{ψ_p} denotes the value of S_ψ at the cell center, and V_p is the volume of the cell. Using the above approximations of Eqs. (38) and (39), the transport equation in Eq. (36) can be discretized as

$$\frac{d}{dt}(\rho_p \psi_p V_p) + \sum_f (\rho_f \mathbf{v}_f \psi_f \cdot \mathbf{a}_f) = \sum_f (\Gamma_f \nabla \psi_f \cdot \mathbf{a}_f) + S_{\psi_p} V_p, \tag{40}$$

where ρ_p denotes the density of the cell center, and ρ_f is the interpolated density at the face f.

(a) Transient Term

For unsteady simulations, the total time interval is subdivided into a number of time steps, and the solutions of governing equation at the current time-level require the results from the previous time-level. The first-order temporal discretization is employed to calculate the transient term F_t by using the solution at the current time level $n+1$ and the solution at the previous time level n:

$$F_t = \frac{d}{dt}(\rho_p \psi_p) \approx \frac{(\rho_p \psi_p)^{n+1} - (\rho_p \psi_p)^n}{\Delta t}. \tag{41}$$

Furthermore, a second-order temporal discretization is also adopted to approximate the transient term by using the solutions at the current time level $n+1$, at the previous time levels n and $n-1$:

$$F_t = \frac{d}{dt}(\rho_p \psi_p) \approx \frac{\left[3(\rho_p \psi_p)^{n+1} - 4(\rho_p \psi_p)^n + (\rho_p \psi_p)^{n-1}\right]}{2\Delta t}. \tag{42}$$

(b) Convection Term

The convective flux C_f is approximated as below:

doi:10.6342/NTU202104312

$$C_f \approx \rho_f \mathbf{v}_f \psi_f \cdot \mathbf{a}_f = \dot{m}_f \psi_f, \tag{43}$$

where $\dot{m}_f$ is the mass flow rate across the face f and ψ_f the value of ψ at the face f. The value at the face f is approximated by the central differencing scheme (CDS) by a linear interpolation between the values of two neighboring cells p and n:

$$\psi_f \approx \alpha_f \psi_p + (1 - \alpha_f)\psi_n, \tag{44}$$

where the linear interpolation factor α_f is defined according to the locations of cell center and face center.

(c) Diffusion Term

The diffusive flux D_f through a cell face is written as

$$D_f \approx \Gamma_f \nabla\psi_f \cdot \mathbf{a}_f, \tag{45}$$

where $\nabla\psi_f$, the gradient of ψ at the face, plays an important role in the numerical discretization. To obtain a second-order accurate approximation for an interior-face gradient, the following equation is used

$$\nabla\psi_f \approx (\psi_n - \psi_p)\boldsymbol{\alpha}_f + \overline{\nabla\psi_f} - (\overline{\nabla\psi_f} \cdot \mathbf{ds})\boldsymbol{\alpha}_f, \tag{46}$$

$$\mathbf{ds} = \mathbf{x}_n - \mathbf{x}_p, \tag{47}$$

$$\boldsymbol{\alpha}_f = \frac{\mathbf{a}_f}{\mathbf{a}_f \cdot \mathbf{ds}}, \tag{48}$$

$$\overline{\nabla\psi_f} = \alpha_f \nabla\psi_p + (1 - \alpha_f)\nabla\psi_{\mathrm{n}}, \tag{49}$$

where $\mathbf{x}_p$ and $\mathbf{x}_n$ are the location of the cell p and its neighboring cell n.

Therefore, the diffusive flux across an interior face is expressed as follows:

doi:10.6342/NTU202104312

$$D_f \approx \Gamma_f\left[(\psi_n - \psi_p)\boldsymbol{\alpha}_f \cdot \mathbf{a}_f + \overline{\nabla\psi_f} \cdot \mathbf{a}_f - \left(\overline{\nabla\psi_f} \cdot \mathbf{ds}\right)\boldsymbol{\alpha}_f \cdot \mathbf{a}_f\right], \quad (50)$$

similarly, the diffusive flux across a boundary face is given as

$$D_f \approx \Gamma_f\left[(\psi_f - \psi_p)\boldsymbol{\alpha}_f \cdot \mathbf{a}_f + \nabla\psi_p \cdot \mathbf{a}_f - \left(\nabla\psi_p \cdot \mathbf{ds}\right)\boldsymbol{\alpha}_f \cdot \mathbf{a}_f\right], \quad (51)$$

$$\mathbf{ds} = \mathbf{x}_f - \mathbf{x}_p, \quad (52)$$

where $\mathbf{x}_f$ is the center location of face f. The second and third terms in Eqs. (50) and (51) are essential for improving the prediction accuracy on non-orthogonal meshes. At the same time, the first terms in Eqs. (50) and (51) contribute to the diagonal dominance of the resultant matrix.

According to the above discussion, the detailed discretization of the transport equations used in the numerical scheme is then rearranged in the form of linearized algebraic equations, i.e., Eq. (53) where the corresponding coefficients are shown in Table 2.3.

$$a_p\psi_p + \sum\nolimits_f a_n\psi_n = b_p \quad (53)$$

Table 2.3: Coefficients of the linearized algebraic equation

a_p	$\frac{3\rho_p}{2\Delta t}V_p + \sum_f \left(\dot{m}_f\alpha_f + \Gamma_f\boldsymbol{\alpha}_f \cdot \mathbf{a}_f\right)$
a_n	$\sum_f \left[\dot{m}_f(1-\alpha_f) - \Gamma_f\boldsymbol{\alpha}_f \cdot \mathbf{a}_f\right]$
b_p	$\frac{\left[4(\rho_p\psi_p)^n - (\rho_p\psi_p)^{n-1}\right]}{2\Delta t}V_p + \sum_f \left\{\Gamma_f\left[\overline{\nabla\psi_f} \cdot \mathbf{a}_f - \left(\overline{\nabla\psi_f} \cdot \mathbf{ds}\right)\boldsymbol{\alpha}_f \cdot \mathbf{a}_f\right]\right\} + S_{\psi_p}V_p$

doi:10.6342/NTU202104312

2-2-2 Pressure-correction Equation

SIMPLE (Semi-Implicit Method for Pressure Linked Equations) algorithm is here used to decouple velocity and pressure in solving the flow field [32]. The discretized momentum and continuity equations for a cell can be represented in the form of linearized algebraic equation

$$a_p \mathbf{v}_p + \sum_f a_n \mathbf{v}_n = \mathbf{b}_p - V_p \nabla p_p, \tag{54}$$

$$\sum_f \dot{m}_f = 0. \tag{55}$$

The momentum equation first uses the pressure field p^* obtained from the previous iteration to solve the updated velocity $\mathbf{v}^*$ that surly satisfies the momentum equation but does not necessarily satisfy the continuity equation. Therefore, the updated solutions are substituted into the equations, and the equations can be rewritten as

$$a_p \mathbf{v}_p^* + \sum_f a_n \mathbf{v}_n^* = \mathbf{b}_p - V_p \nabla p_p^*, \tag{56}$$

$$\sum_f \dot{m}_f = \sum_f \left(\dot{m}_f^* + \dot{m}_f'\right) = \sum_f \left(\rho_f \, \mathbf{a}_f \cdot \mathbf{v}_f^* + \dot{m}_f'\right) = 0, \tag{57}$$

where $\dot{m}_f^*$ denotes the mass flow rate across the face f based on $\mathbf{v}_f^*$, $\dot{m}_f'$ the correction of mass flow rate to satisfy the continuity equation. The corrected pressure p_p and velocity $\mathbf{v}_p$ of the current iteration can be written as

$$p_p = p_p^* + p_p', \tag{58}$$

$$\mathbf{v}_p = \mathbf{v}_p^* + \mathbf{v}_p'. \tag{59}$$

From Eqs. (54) and (56), the velocity vector can be rearranged as

doi:10.6342/NTU202104312

$$\mathbf{v}_p = \frac{\mathbf{b}_p - V_p \nabla p_p - \sum_f a_n \mathbf{v}_n}{a_p}, \tag{60}$$

$$\mathbf{v}_p^* = \frac{\mathbf{b}_p - V_p \nabla p_p^* - \sum_f a_n \mathbf{v}_n^*}{a_p}. \tag{61}$$

Therefore, the correction of the velocity field $\mathbf{v}_p'$ is shown as

$$\mathbf{v}_p' = \frac{V_p(\nabla p_p^* - \nabla p_p) + \sum_f a_n(\mathbf{v}_n^* - \mathbf{v}_n)}{a_p} = -\frac{V_p(\nabla p_p') + \sum_f a_n(\mathbf{v}_n')}{a_p}. \tag{62}$$

And, the velocity correction at the face f is approximated by

$$\mathbf{v}_f' = -\frac{V_f(\nabla p_f')}{a_f} + \tilde{\mathbf{v}}_f' \approx -\frac{V_p + V_n}{a_p + a_n}\nabla p_f' + \tilde{\mathbf{v}}_f' \approx \frac{V_p + V_n}{a_p + a_n}(p_p' - p_n')\boldsymbol{\alpha}_f + \tilde{\mathbf{v}}_f', \tag{63}$$

where $\tilde{\mathbf{v}}_f'$ will be discussed in the later paragraph, and V_n is the volume of the neighboring cell n.

Hence, the continuity equation in Eq. (57) becomes

$$\sum_f \dot{m}_f' \approx \sum_f \left\{ \rho_f \, \mathbf{a}_f \cdot \left[\frac{V_p + V_n}{a_p + a_n}(p_p' - p_n')\boldsymbol{\alpha}_f + \tilde{\mathbf{v}}_f' \right] \right\} = -\sum_f \dot{m}_f^*. \tag{64}$$

Rearranging Eq. (64), the pressure correction equation is then represented as

$$\begin{aligned} &\sum_f \left[\rho_f \left(\frac{V_p + V_n}{a_p + a_n} \right) \boldsymbol{\alpha}_f \cdot \mathbf{a}_f (p_p' - p_n') \right] = -\sum_f \left(\dot{m}_f^* + \rho_f \, \mathbf{a}_f \cdot \tilde{\mathbf{v}}_f' \right) \\ &= -\sum_f \left(\dot{m}_f^* + \dot{\tilde{m}}_f' \right) \approx -\sum_f \dot{m}_f^*. \end{aligned} \tag{65}$$

The term $\dot{\tilde{m}}_f'$ is commonly neglected in SIMPLE algorithm. After the pressure correction equation is solved, the pressure correction p' is obtained, and the pressure field and velocity field can be updated to satisfy the mass conservation as below:

$$p_p = p_p^* + p_p', \tag{66}$$

$$\mathbf{v}_p = \mathbf{v}_p^* + \mathbf{v}_p' = \mathbf{v}_p^* - \frac{V_p(\nabla p_p')}{a_p}. \tag{67}$$

doi:10.6342/NTU202104312

In order to suppress unphysical pressure fluctuations from the checkerboard effect caused by a direct linear interpolation of velocity at cell faces, a remedy is proposed for cases using collocated grids [32]. The mass flux $\dot{m}_f^*$ at the face f in Eq. (65) has to be modified before the solution of pressure correction equation

$$\dot{m}_f^* = \rho_f \, \mathbf{a}_f \cdot \mathbf{v}^*{}_f - \gamma_f, \tag{68}$$

where γ_f is the Rhie-and-Chow correction given as follows:

$$\gamma_f = Q_f\left(p_n^* - p_p^* - \nabla p_f^* \cdot \mathbf{ds}\right), \tag{69}$$

where ∇p_f^* is the interpolated gradient of pressure field at the face f.

In Eq. (69), Q_f is expressed as

$$Q_f = \rho_f \left(\frac{V_p + V_n}{a_p + a_n}\right) \boldsymbol{\alpha}_f \cdot \mathbf{a}_f. \tag{70}$$

doi:10.6342/NTU202104312

2-2-3 Wall Distance Calculation

In turbulence modeling, the wall distance is a key parameter to determine turbulent properties near wall. With search procedures to calculate the distance of single cell to all wall boundaries and find the shortest one, the computational time can be very lengthy especially for large non-orthogonal or unstructured 3D grids. In this study, a diffusion equation is used to compute the nearest distance to wall where a distance-related variable φ is solved. This equation is a generalized 3D extension of an exact one-dimensional intuitive formulation [33-35]:

$$\nabla^2\varphi + 1 = 0, \tag{71}$$

with the following boundary conditions

$$\varphi = 0 \text{ at wall,} \tag{72}$$

$$\nabla\varphi \cdot \mathbf{n} = 0 \text{ at other boundaries.} \tag{73}$$

The wall distance d is then computed from the equation below:

$$d = -|\nabla\varphi| + \sqrt{|\nabla\varphi|^2 + 2\varphi}. \tag{74}$$

This approximation of wall distance is accurate near wall, and it is not applicable to the position far from wall. To obtain a more accurate calculation of wall distance, the equation can be modified as Eikonal equation [36].

doi:10.6342/NTU202104312

2-2-4 Solution Procedure



The numerical code is developed on the platform of ultraMPP (ultra-fast Massive Parallel Platform) which is a general-purpose parallelization platform for physical problems modelled by PDEs [37]. The platform helps to reduce the required works, such as loading different types of mesh file, setting up the stencil matrix, linking the libraries like PETSc (the Portable, Extensible Toolkit for Scientific Computation), for solving linearized equations and preparing parallel processing. The code implemented in this study uses the numerical discretization of governing equations discussed in the above subsections, and the solution procedure is shown in Figure 2.1.

The computational domain and the mesh are built according to the problem, and the related parameters, such as boundary conditions, are set in the input file. The numerical procedure first reads the mesh and control parameters to define the computational domain and boundary conditions. The wall distance is then calculated. The initial condition is also set according to the input file. Then, the numerical procedure uses SIMPLE algorithm to solve the velocity and pressure fields followed by the solution of other governing equations and the update of the fluid properties. The outer iteration stops until the normalized mass imbalance $\widehat{\sum \dot{m}}$ is lower than $\widehat{\sum \dot{m}}^*$, or the iteration number is equal to n_i. In this study, $\widehat{\sum \dot{m}}^*$ is set to 10^{-4}, and a typical convergence history of $\widehat{\sum \dot{m}}$ is shown in Figure 2.2. The normalized mass imbalance

doi:10.6342/NTU202104312

is defined as

$$\widehat{\sum \dot{m}} = \frac{\sum_{cell} \left| \sum_f \dot{m} \right|}{|\dot{m}_{in}|}, \tag{75}$$

where $\dot{m}_{in}$ denotes the inlet mass flow rate. The control parameters and constants are given in Appendix II. A typical convergence history of voltage drop is illustrated in Figure 2.3, where the voltage drop seems to converge after around ten thousand iterations.

In this study, a steady simulation is employed as the initial condition for solving an unsteady simulation, where the steady simulation uses a circumferentially uniform boundary condition. After the steady flow field is predicted, the unsteady calculation starts with the steady solution. The boundary conditions update every time step, such as the cathode spot, in the unsteady modeling.

doi:10.6342/NTU202104312

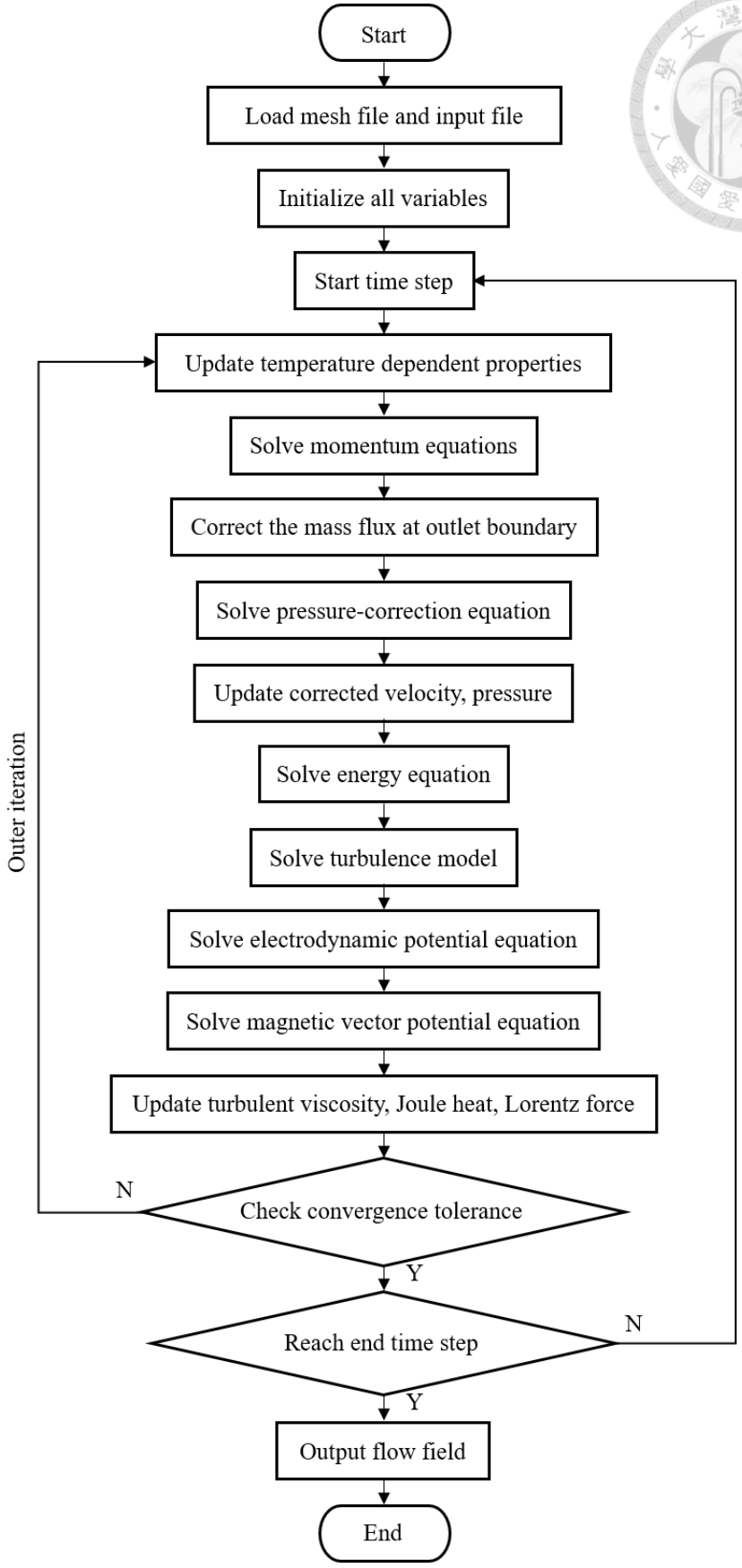


Figure 2.1: Flowchart of the numerical scheme

doi:10.6342/NTU202104312

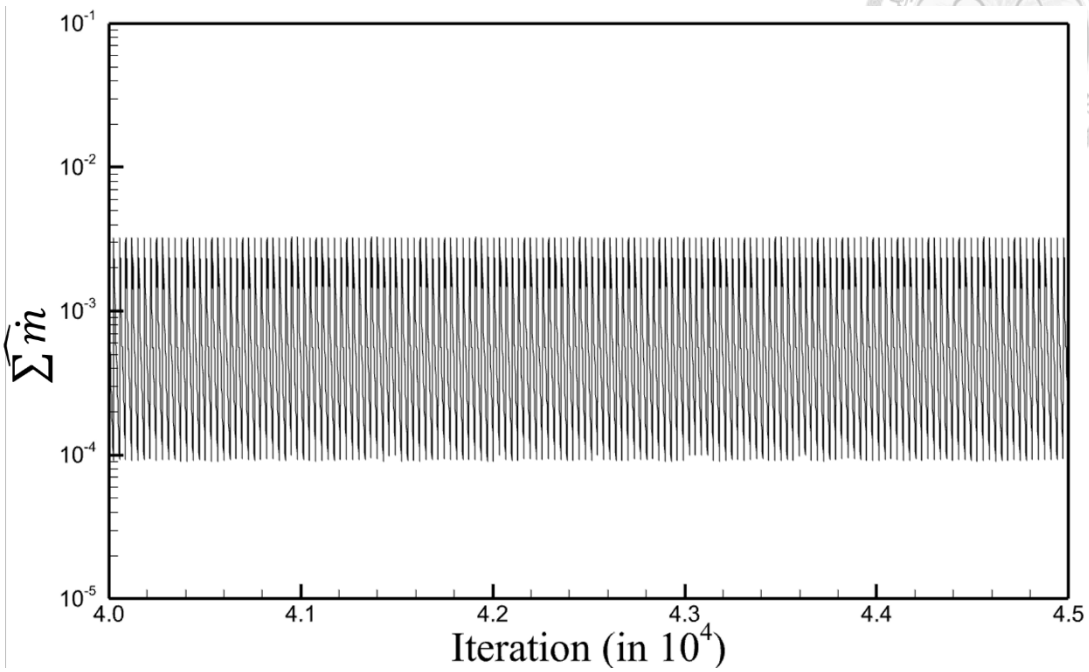


Figure 2.2: Convergence history of the normalized mass imbalance for $I = 140$ A and $Q = 140$ SLM

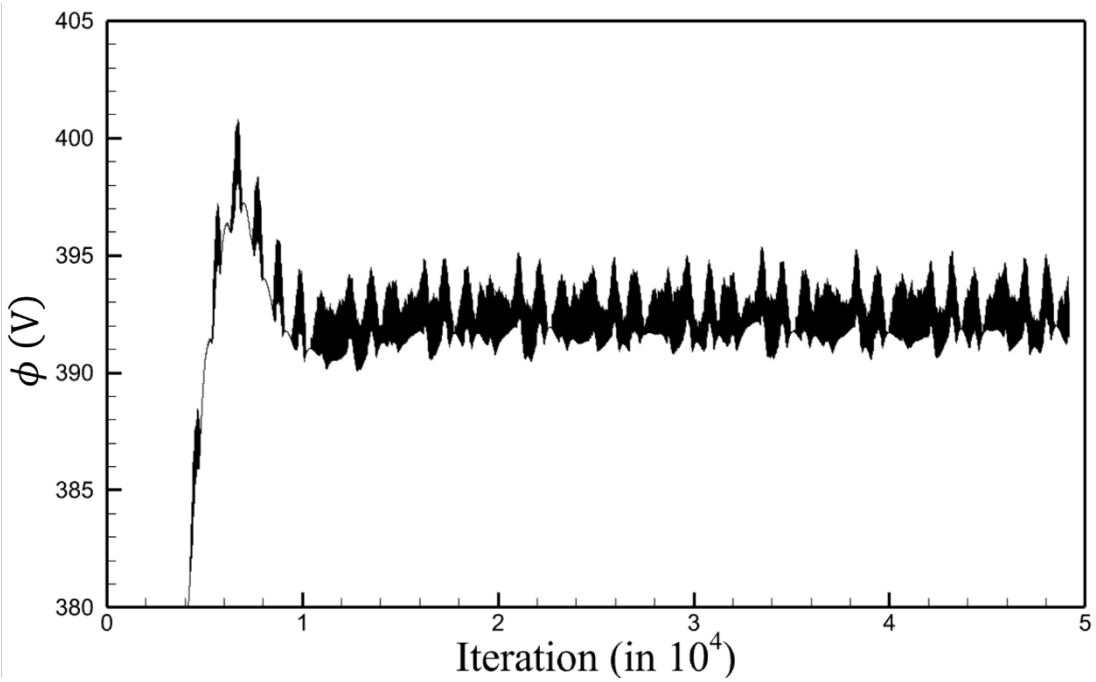


Figure 2.3: Convergence history of voltage drop for $I = 140$ A and $Q = 140$ SLM

doi:10.6342/NTU202104312

Chapter 3 Study Case

3-1 Description of Experiment

The reference experiment consists of a non-transferred plasma torch, an adjustable pressure test chamber, a torch DC power supply, a cooling water circulating unit and a gas supply unit, as well as a control and data acquisition unit, where its schematic illustration is depicted in Figure 3.1 [38]. The pressure test chamber is installed behind the plasma torch and cooled down by a heat exchanger. The non-transferred DC plasma torch equipped with cooling water circulating unit is operated with the DC power supply with the maximum working voltage of 600 V and the maximum working current of 200 A. The gas supply unit provides up to $7\,\mathrm{kg/cm^2}$ of compressed dry air. The pressure control valve is able to dynamically adjust the pressure of the inlet gas. The control and data acquisition unit are used to monitor and record the operating of the whole system.

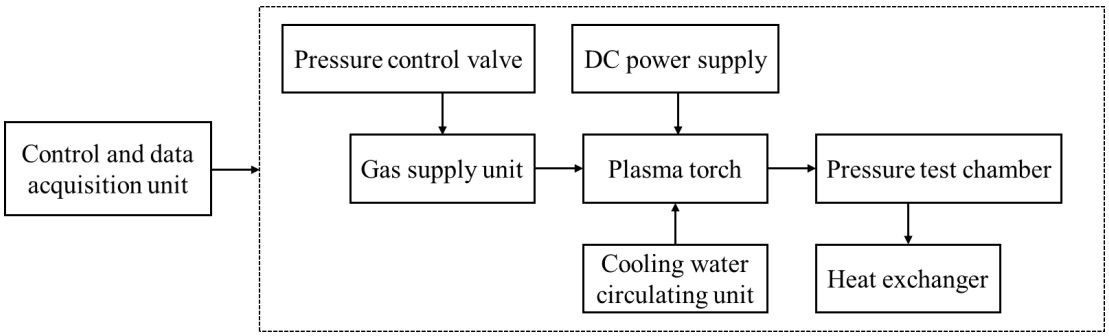


Figure 3.1: The schematic illustration of the experiment system

doi:10.6342/NTU202104312

3-2 Case Description

The cases studied in this study are shown in Table 3.1. The cases were also simulated via 2D axisymmetric modeling [2], and the comparison of 2D and 3D models is discussed in Chapter 4. The experimental working current I is between 100 A and 200 A, and the inlet flow rate Q are between 100 SLM and 200 SLM.

Table 3.1: The modelled conditions

I (A) / Q (SLM)	100	120	140	160	180	200
100			✓			
120			✓			
140	✓	✓	✓	✓	✓	✓
160			✓			
180			✓			
200			✓			

doi:10.6342/NTU202104312

3-3 Computational Domain and Boundary Conditions

Schematic illustrations of the computational domain of the non-transferred DC plasma torch used in this study are shown in Figure 3.2 and Figure 3.3. The size of the computational domain and the boundaries are given in Table 3.2. The cathode spot in this study is regarded as a circle region moving on the inner surface of the torch. The inlet and anode are both assumed to be a ring area on the torch inner surface. The torch is 690 mm long and has a radius of 11 mm. The detailed boundary conditions are listed in Table 2.1 and Table 3.3. The normal velocity $V_{\mathrm{in},n}$, the tangential velocity $V_{\mathrm{in},t}$, the temperature T_{in}, the kinetic energy k_{in} and the specific dissipation rate ω_{in} of the inlet boundary vary with the conditions of the inlet flow rate. The maximum value of the current density J_{max} and the given constant b of the cathode region given in Eq. (35) vary with the working current. The corresponding values are shown in Table 3.4 and Table 3.5. The pressure is assumed 1 atm at the inflow boundary. The temperature of wall T_{w}, the temperature of cathode T_{c} and the temperature of anode T_{a} as indicated in [2] are 1000 K, 3000 K and 1000 K, respectively.

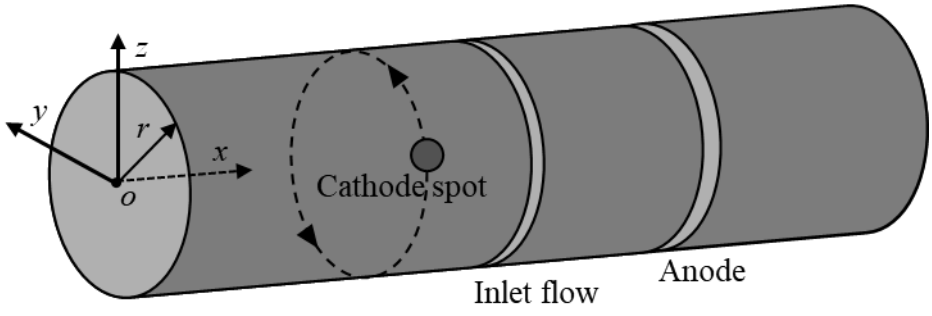


Figure 3.2: A schematic illustration of the computational domain (3D view)

doi:10.6342/NTU202104312

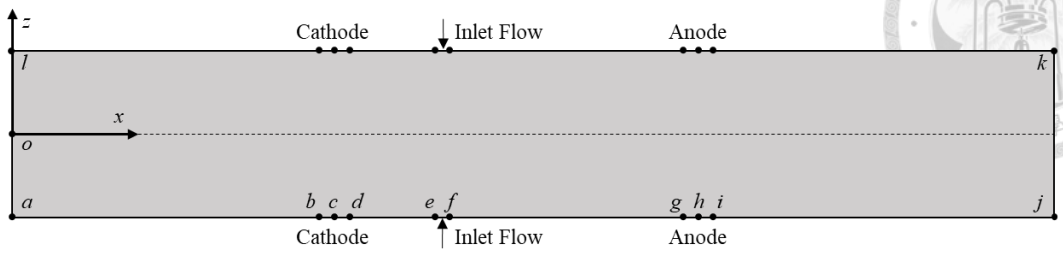


Figure 3.3: A schematic illustration of the computational domain (2D view)

Table 3.2: Dimension of computational domain

Region	Length (mm)	Physical Definition
$\overline{oa}$	11	Radius of the torch
$\overline{al}$	22	Bottom of the torch
$\overline{ac}$	213.5	Length of cathode arc root to bottom of the torch
$\overline{bc}$	3	Radius of cathode arc root
$\overline{ae}$	297	Length of the inlet to the bottom of the torch
$\overline{ef}$	3	Width of the inlet
$\overline{ah}$	–	Length of anode arc root to the bottom of the torch
$\overline{ch}$	–	Arc length L_{arc}
$\overline{gh}$	3	Radius of anode arc root
$\overline{aj}$	690	Length of the torch
$\overline{jk}$	22	Outlet of the torch

Table 3.3: Boundary conditions of each boundary

Region	Boundary condition
$\overline{al}$	Wall
$\overline{ae}$	Wall
$\overline{ef}$	Inlet
$\overline{fj}$	Wall
$\overline{bd}$	Cathode
$\overline{gi}$	Anode
$\overline{jk}$	Outlet

doi:10.6342/NTU202104312

Table 3.4: Boundary conditions for different inlet flow rates [2]

Q (SLM)	$V_{\mathrm{in},n}$ (m/s)	$V_{\mathrm{in},t}$ (m/s)	T_{in} (K)
100	7.6250	40.8713	297.3727
120	9.1042	51.1984	296.9376
140	10.5759	61.6087	296.4074
160	12.0133	72.0190	295.7621
180	13.4265	82.4293	295.0151
200	14.8333	92.8395	294.1654

Table 3.5: Boundary conditions for different working currents [2]

I (A)	$J_{\max}$ (A/mm^2)	b
100	12.0	665
120	14.4	665
140	16.8	665
160	19.2	665
180	21.6	665
200	24.0	665

doi:10.6342/NTU202104312

(a) Cathode

In an unsteady simulation, the cathode spot position is assumed to move in a given frequency on the torch inner surface. The arc moving frequency is assumed 1000 Hz based on the observation in the reference experiment [38]. The time step size for the simulation is 20 μs. In other words, one cycle time of the cathode spot is equal to 50 time steps.

The cathode fall V_C is a relatively rapid drop of electric potential ϕ arising in a very thin layer near the cathode, i.e., the cathode layer. Because high current density near cathode implies high positive space charge, the ratio of electronic current to ionic current near the cathode determines the cathode fall. The gas temperature suddenly decreases near the cathode because of the collision between the gas and the cathode metal. The charge production from thermal ionization then reduces, and the electrical conductivity of gas in the cathode layer becomes lower than its surroundings. The energy flux of ions and electrons from the plasma to the cathode surface is balanced by the heat removed by the electrons leaving the cathode surface [39]. The value of the cathode fall depends on the cathode material and the operation conditions [40]. Table 3.6 lists the characteristics of cathode material. The cathode material is Cu in the experiment, so the cathode falls in this study ranges from 15 V to 21 V.

doi:10.6342/NTU202104312

Table 3.6: Characteristics of cathode material [40, 41]

Metal	Cu	Ag	Fe	W
Ionization potential (V)	7.68	7.54	7.83	7.98
Cathode fall (V)	15~21	12~16	17~18	16~22
Boiling point (K)	3510	2436	3045	5900
Thermal conductivity ($W/cm \cdot K$)	4.1	4.17	0.84	1.67
Average current to a spot (A)	75~200	60~100	60~100	100~300
Current density (A/cm^2)	10^4~10^8	10^6	10^7	10^4~10^6

(b) Anode

The anode fall is generally low in the situation of large anode surface and without additional energy for sustaining the electron current near the anode region [40]. Therefore, the anode fall is neglected in this study. It is observed in the reference experiment that the arc root of anode randomly travels on the torch inner surface. The arc root frequency of anode may differ from the one of cathode. The anode position is therefore difficult to be found in the experiment, because the reference experiment measured the voltage drop under different conditions, so the anode position is fixed by the measured voltage drop. The anode region is regarded as a ring area in this study. In numerical simulations, the anode position is tested until the averaged voltage drop falls in the range of ϕ_{ref}, Table 3.7 and Table 3.8. After the anode position is fixed, the arc length is defined as the distance between the cathode and the anode. The arc length L_{arc} is given in Table 3.9 and Table 3.10.

doi:10.6342/NTU202104312

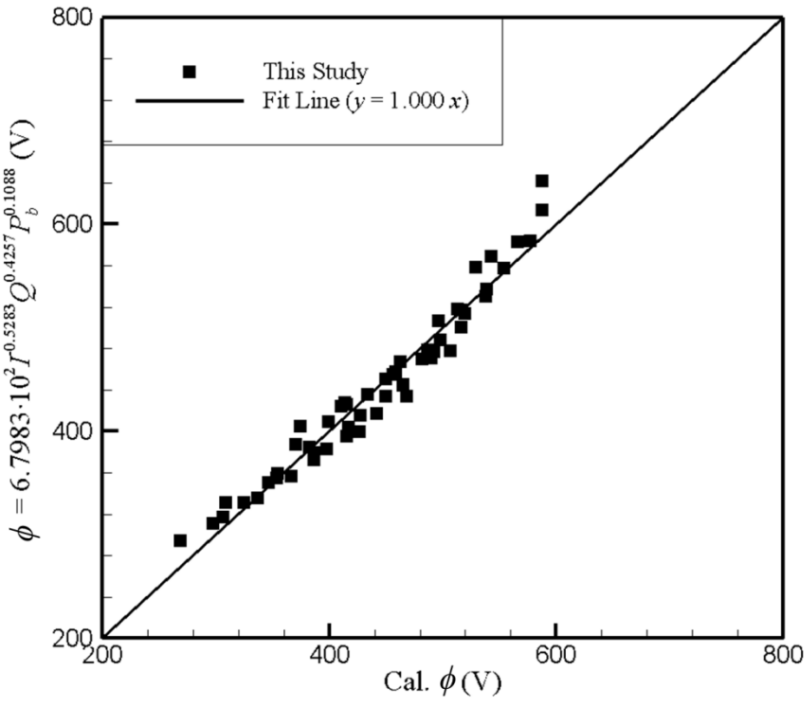


Figure 3.4: Dependence of ϕ on I and Q [2]

Table 3.7: Target voltage drop for $I = 140$ A

Q (SLM)	ϕ_{ref} (V)
100	333.8~339.8
120	362.4~368.4
140	388.5~394.5
160	412.4~418.4
180	434.7~440.7
200	455.6~461.6

Table 3.8: Target voltage drop for $Q = 140$ SLM

I (A)	ϕ_{ref} (V)
100	468.1~474.1
120	423.2~429.2
140	388.5~394.5
160	360.6~366.6
180	337.5~343.5
200	318.1~324.1

doi:10.6342/NTU202104312

Table 3.9: Arc length of $I = 140$ A

Q (SLM)	L_{arc} (mm)
100	216.5
120	226.5
140	236.5
160	246.5
180	254
200	266.5

Table 3.10: Arc length of $Q = 140$ SLM

I (A)	L_{arc} (mm)
100	331.5
120	276.5
140	236.5
160	206.5
180	181.5
200	166.5

doi:10.6342/NTU202104312

3-4 Plasma Properties

In this study, there are six gas properties which are functions of temperature, namely, the density ρ, the electrical conductivity σ, the thermal conductivity λ, the specific heat capacity C_p, the material viscosity μ_m and the radiation loss E_R. These properties of air plasma at 1 atm are shown from Figure 3.5 to Figure 3.10 [42]. An approximation of the electrical conductivity σ is employed when the temperature is below 9000 K [9]:

$$\sigma = 22.22 \times e^{\frac{T}{2000}}. \tag{76}$$

When the temperature is higher than 9000 K, the electrical conductivity σ follows the curve given in Figure 3.6.

doi:10.6342/NTU202104312

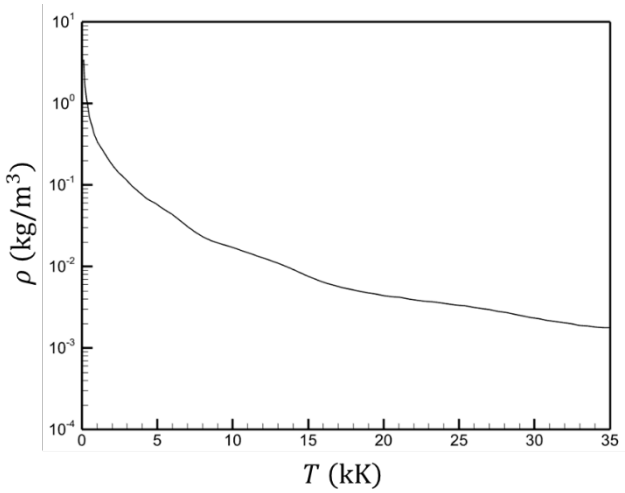


Figure 3.5: Dependence of density on temperature for air plasma

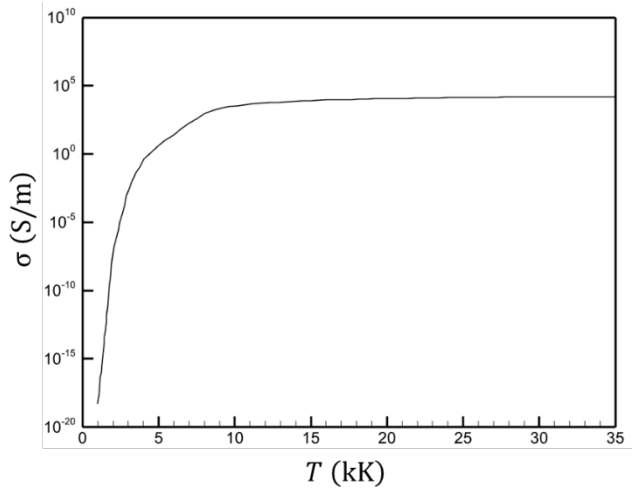


Figure 3.6: Dependence of electrical conductivity on temperature for air plasma

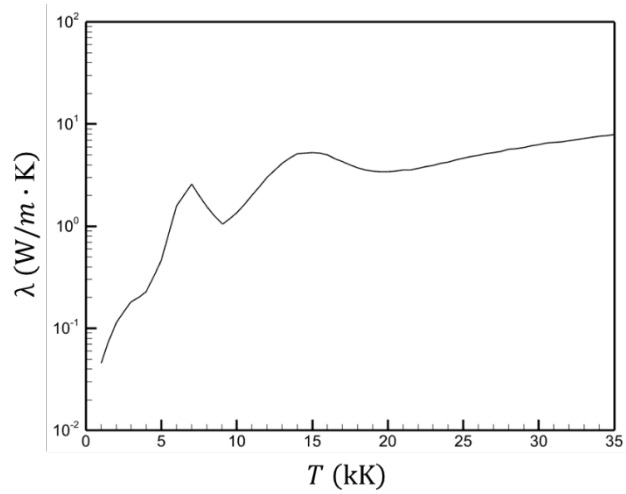


Figure 3.7: Dependence of thermal conductivity on temperature for air plasma

doi:10.6342/NTU202104312

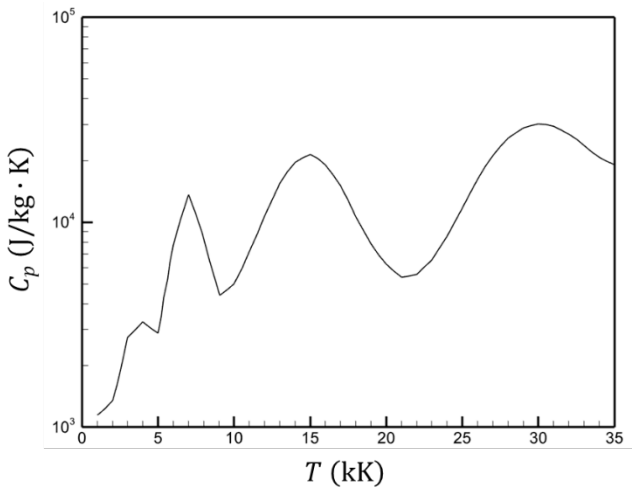


Figure 3.8: Dependence of specific heat capacity on temperature for air plasma

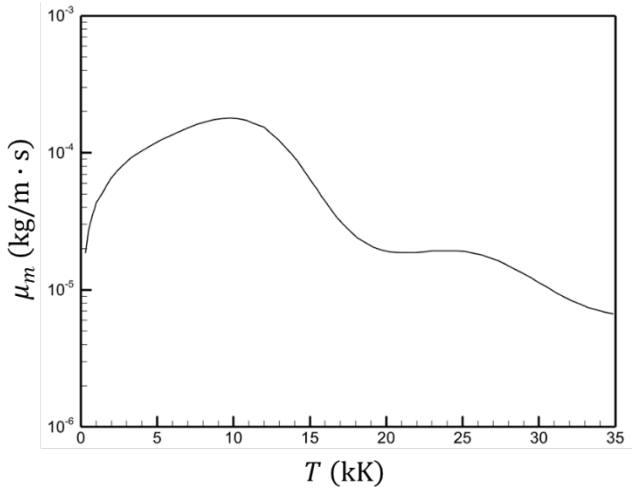
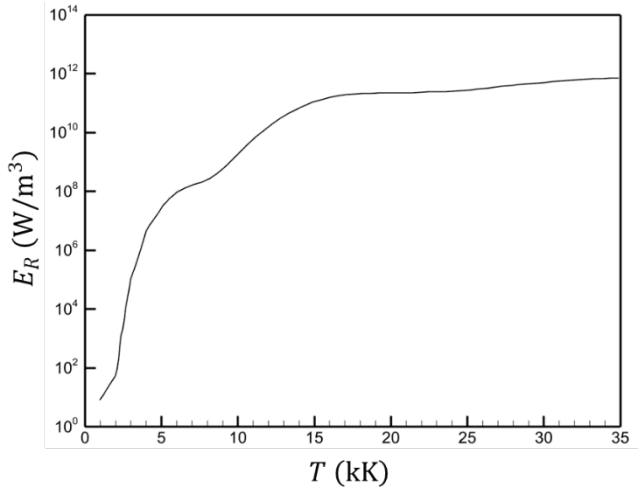


Figure 3.9: Dependence of viscosity on temperature for air plasma



.

Figure 3.10: Dependence of radiation loss on temperature for air plasma

doi:10.6342/NTU202104312

3-5 Mesh

A 3D grid employed in the simulation, Figure 3.11, is extruded from a 2D section, Figure 3.12, along the axial direction. A typical mesh distribution for $I = 140$ A and $\mathrm{Q} = 140$ SLM is shown in Figure 3.12 and Figure 3.13. The total cell number is approximately 2.3 million. The grid is clustered near the wall with a size of 0.15 mm to satisfy the requirement of turbulence modeling. The axial grid clustering is performed in vicinity of wall, cathode, inflow, anode and outlet with a grid size of 0.5 mm. The Reynolds number in this study is in the order of 1000, and y^+ is controlled under 25 via the employed grid arrangement.

doi:10.6342/NTU202104312

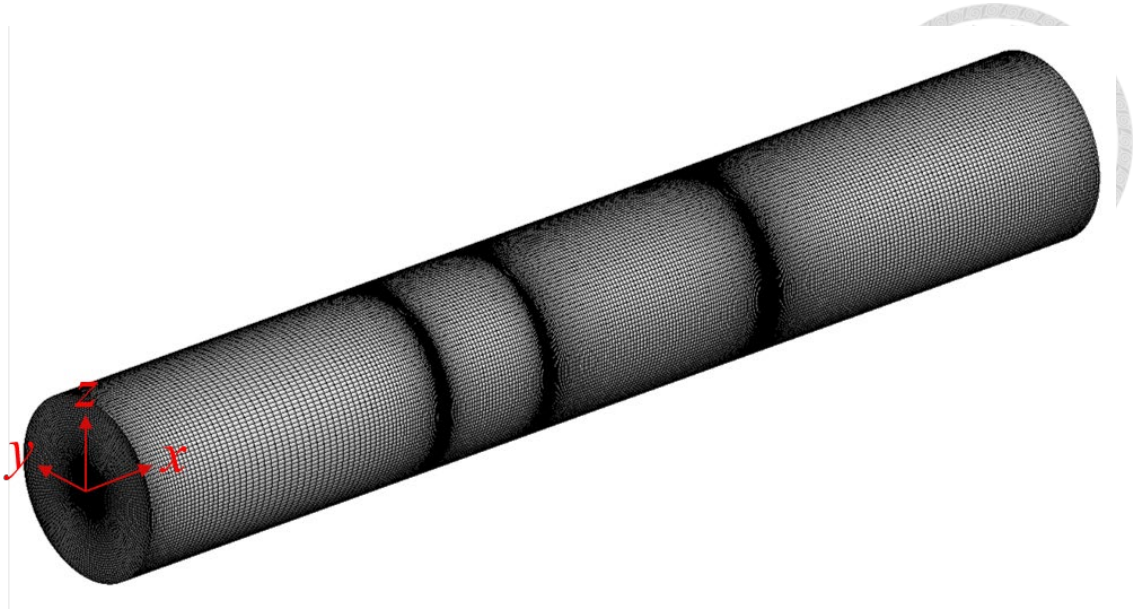


Figure 3.11: Mesh used to discretize the computational domain (x axis is scaled by 0.2)

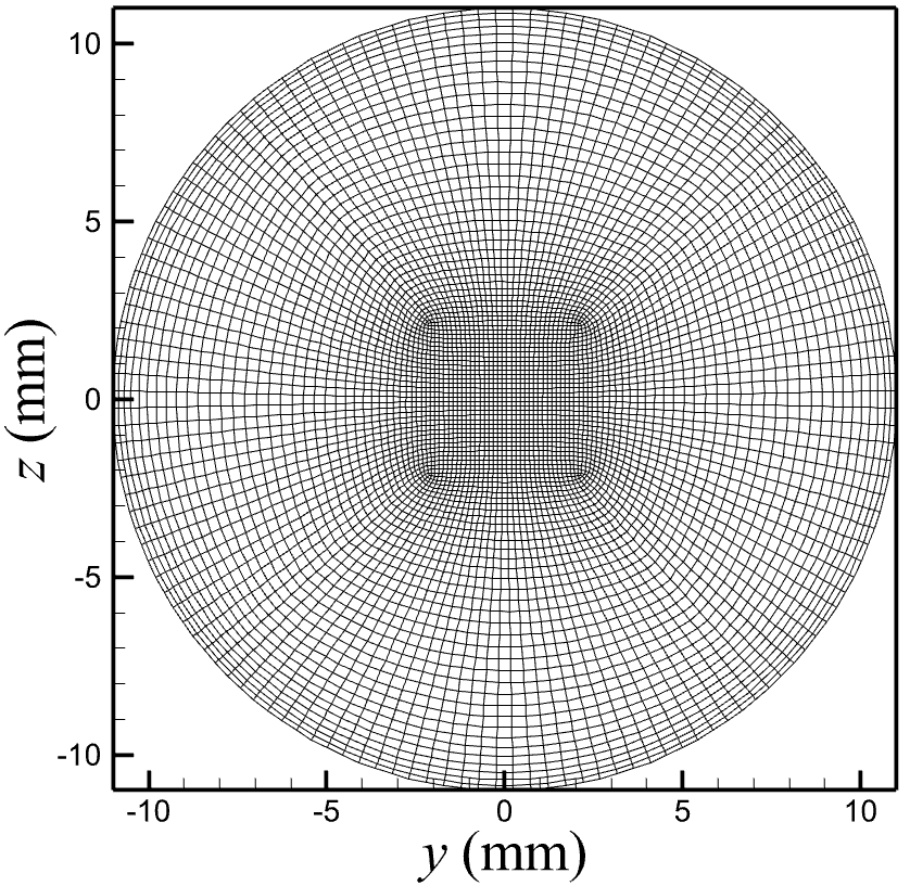


Figure 3.12: Mesh cut at $x = 0$

doi:10.6342/NTU202104312

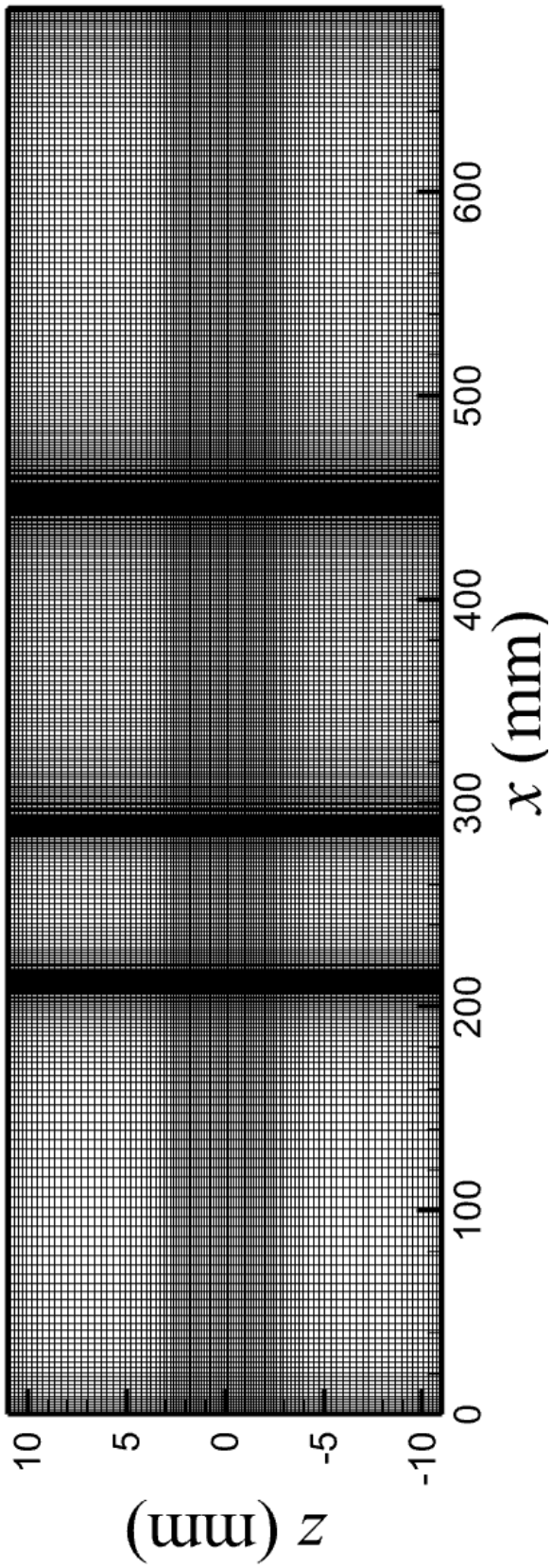


Figure 3.13: Mesh cut at $y = 0$

doi:10.6342/NTU202104312

3-6 Grid Dependency

In a computational study, grid distribution is an important factor to impact accuracy. A dense grid distribution may result in a solution with low spatial discretization error but require more computational time. In order to choose a proper mesh size in this study, a grid dependency analysis is conducted [43], where the grid-independent solution is estimated via Richardson extrapolation. The physical quantities used in the grid dependency study are the mean outlet axial velocity, the mean outlet temperature and the time-averaged voltage drop between the electrodes. The grid-independent solution ψ^{∞} is given in Eq. (77) when a method of second-order accuracy is used.

$$\psi^{\infty} = \psi^{n} + \frac{\psi^{n} - \psi^{n-1}}{\left(\sqrt[3]{\frac{N_n}{N_{n-1}}}\right)^2 - 1}, \tag{77}$$

where ψ^{n} and ψ^{n-1} represent the solution obtained from nth and $(n-1)$th grid level, and N_n and N_{n-1} are the cell numbers of nth and $(n-1)$th grid level. The discretization error E_{ψ}^{n} of the nth grid level is defined as

$$E_{\psi}^{n} = \left|\frac{\psi^{\infty} - \psi^{n}}{\psi^{\infty}}\right|. \tag{78}$$

For a second-order method, the ideal discretization error E^{*} is calculated by the equation given below:

$$E^{*} \approx C\delta x^{2}, \tag{79}$$

doi:10.6342/NTU202104312

$$\log(E^*) \approx \log(C) + 2\log(\delta x), \tag{80}$$

where C is a constant and δx denotes the normalized grid size. Thus, the ideal slope of E^* is 2 in logarithmic scale. The mean value of variable ψ at the outlet, i.e., ψ^m, is defined as

$$\psi^m = \frac{\int \rho\psi\mathbf{v}\cdot d\mathbf{A}}{\int \rho\mathbf{v}\cdot d\mathbf{A}}, \tag{81}$$

In this section, the time averaged values of mean axial velocity and temperature at the outlet and time averaged voltage drop of different cell number in the case of $I = 140$ A and $Q = 140$ SLM are shown in Figure 3.14, Figure 3.15 and Figure 3.16, respectively. The dependence of E_ψ^n on normalized grid size in the case of $I = 140$ A and $Q = 140$ SLM is depicted in Figure 3.17, Figure 3.18 and Figure 3.19, respectively. When the cell number is higher than about 2.3 million, the discretization error E_ψ is less than 4 %. Therefore, the typical cell number of 2.3 million is capable of simulating the fluid with a sufficient accuracy.

doi:10.6342/NTU202104312

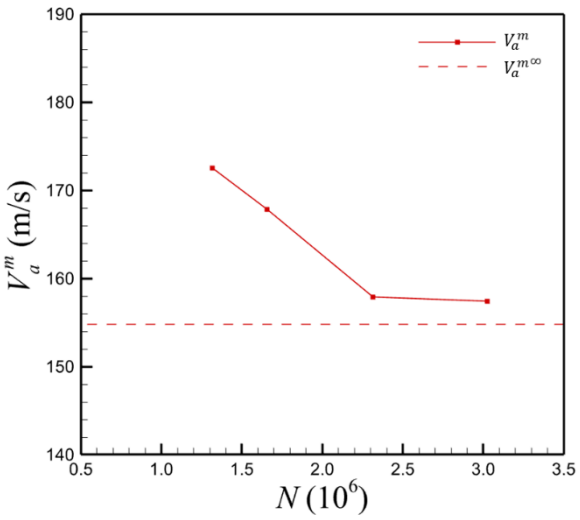


Figure 3.14: Dependence of V_a^m on N

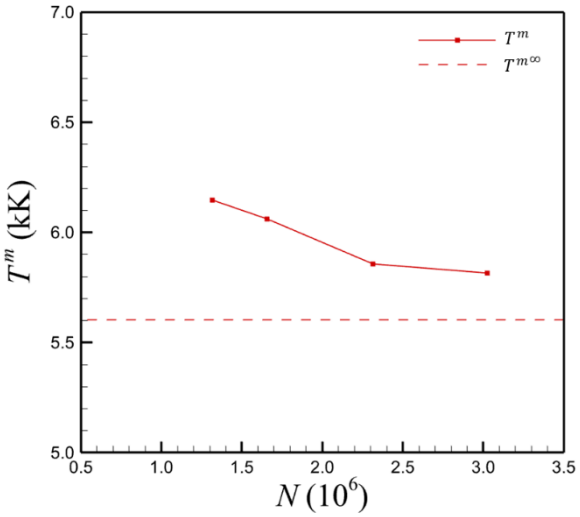


Figure 3.15: Dependence of T^m on N

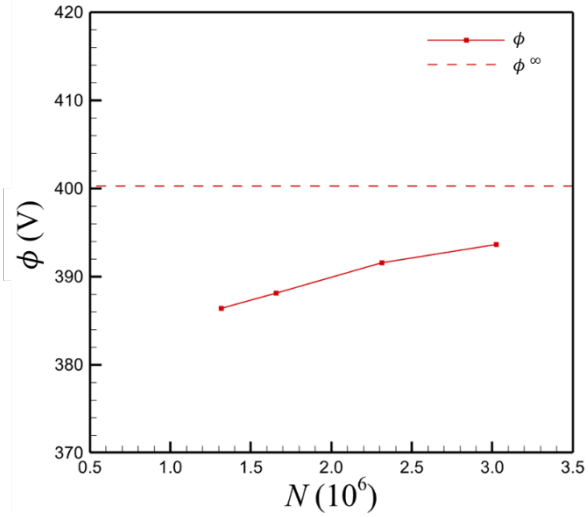


Figure 3.16: Dependence of ϕ on N

doi:10.6342/NTU202104312

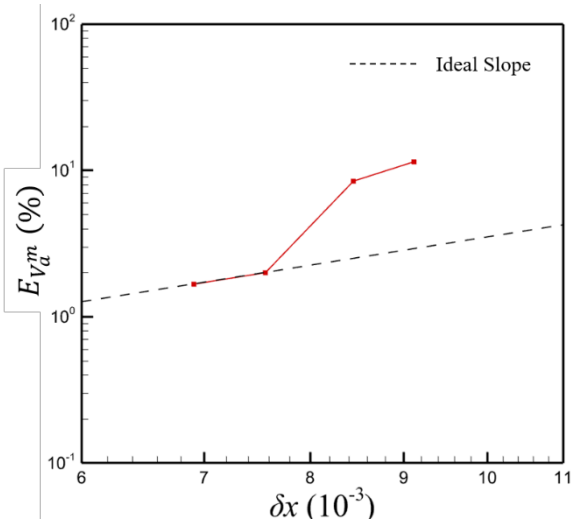


Figure 3.17: Discretization error of V_a^m

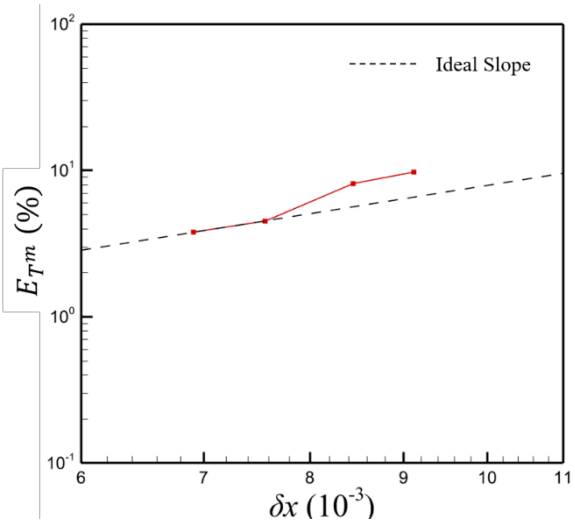


Figure 3.18: Discretization error of T^m

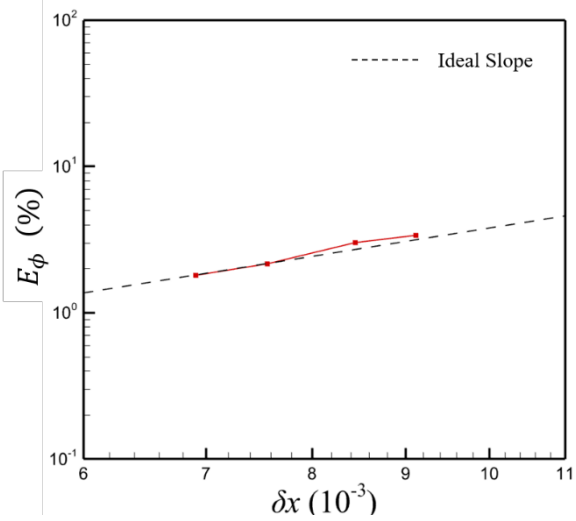


Figure 3.19: Discretization error of ϕ

doi:10.6342/NTU202104312

Chapter 4 Result and Discussion

4-1 Validation

A DC arc measurement at $I = 200$ A and $Q = 68.8$ mg/s [44] is adopted to validate the numerical method proposed in this study. The computational domain of the referenced transferred argon plasma torch is illustrated in Figure 4.1 and Figure 4.2, where the boundary conditions are listed in Table 4.1. A cone-shaped cathode is used in the experiment but a circular surface is used for the convenience of meshing in the simulation, and the current density at the cathode surface is assumed to follow Eq. (35). Figure 4.3 and Figure 4.4 display the mesh cuts of the employed 3D grid at $x = 0$ and $y = 0$, respectively. Figure 4.5 depicts the predicted temperature distribution between the electrodes where the prediction of the proposed numerical model favorably agrees with the experimental measurement. Therefore, the proposed numerical scheme is proven to provide sufficient engineering accuracy in predicting thermal plasma flows.

doi:10.6342/NTU202104312

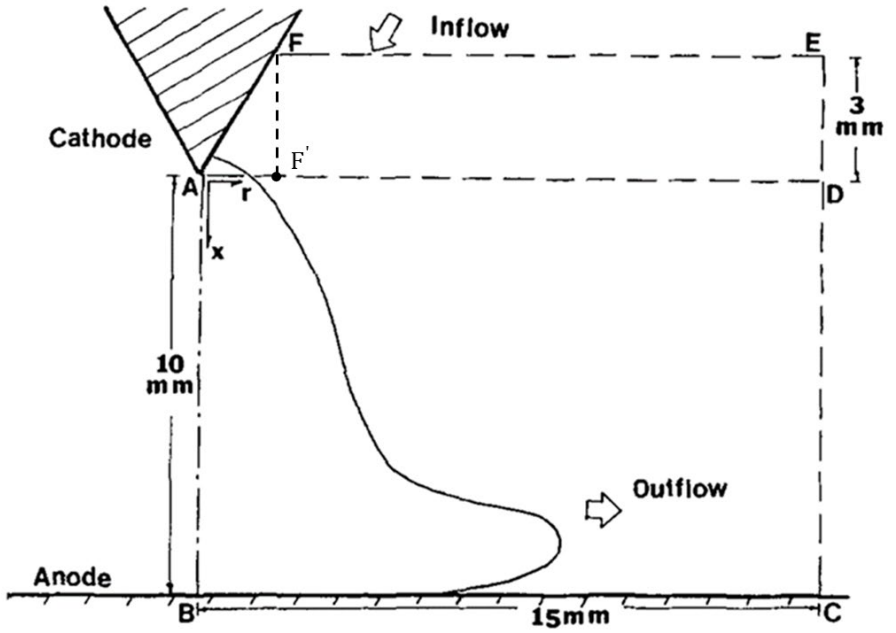


Figure 4.1: The computational domain given in the reference [44]

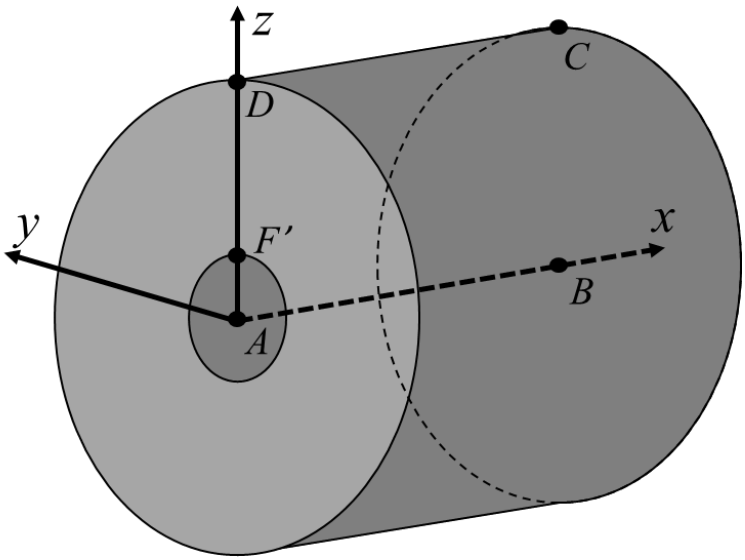


Figure 4.2: The employed 3D computational domain

Table 4.1: Boundary conditions

Region	$\overline{BC}$	$\overline{CD}$	$\overline{DF'}$	$\overline{F'A}$
Type	Anode	Outlet	Inlet	Cathode
$\mathbf{v}$	0	$\nabla\mathbf{v}\cdot\mathbf{n}=\mathbf{0}$	$(0.209\ \mathrm{m/s}, 0, 0)$	0
T	1000 K	$\nabla T\cdot\mathbf{n}=0$	1000 K	3000 K
ϕ	0	$\nabla\phi\cdot\mathbf{n}=0$	$\nabla\phi\cdot\mathbf{n}=0$	Eq. (35)

doi:10.6342/NTU202104312

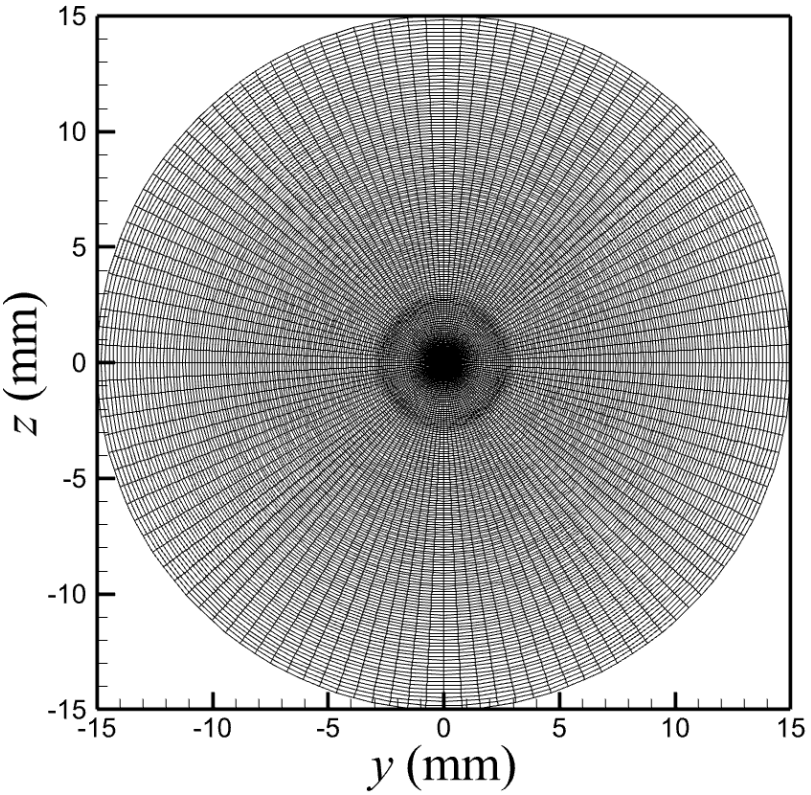


Figure 4.3: Mesh cut at $x = 0$

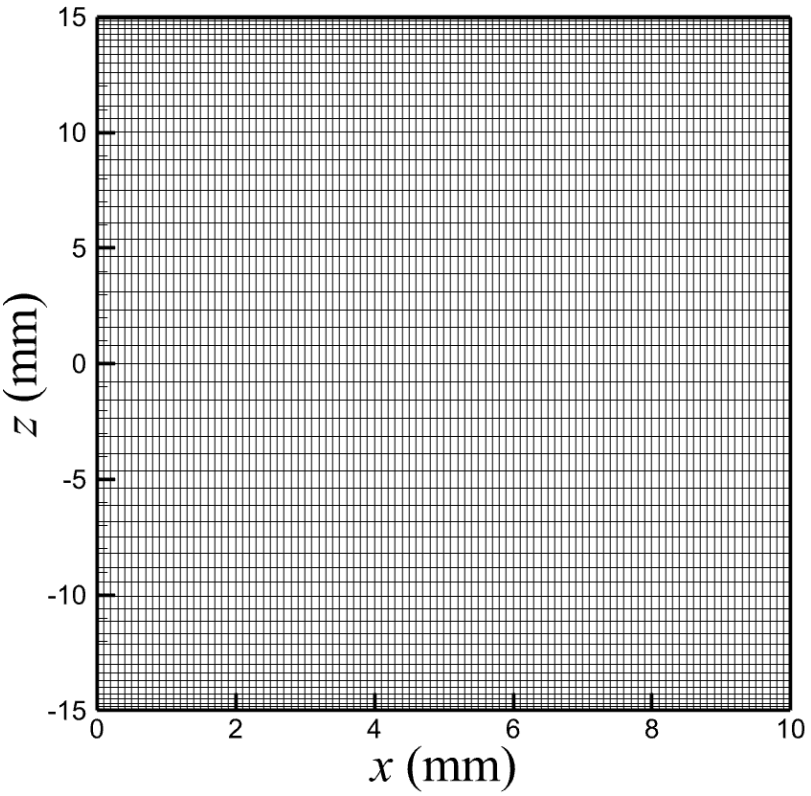


Figure 4.4: Mesh cut at $y = 0$

doi:10.6342/NTU202104312

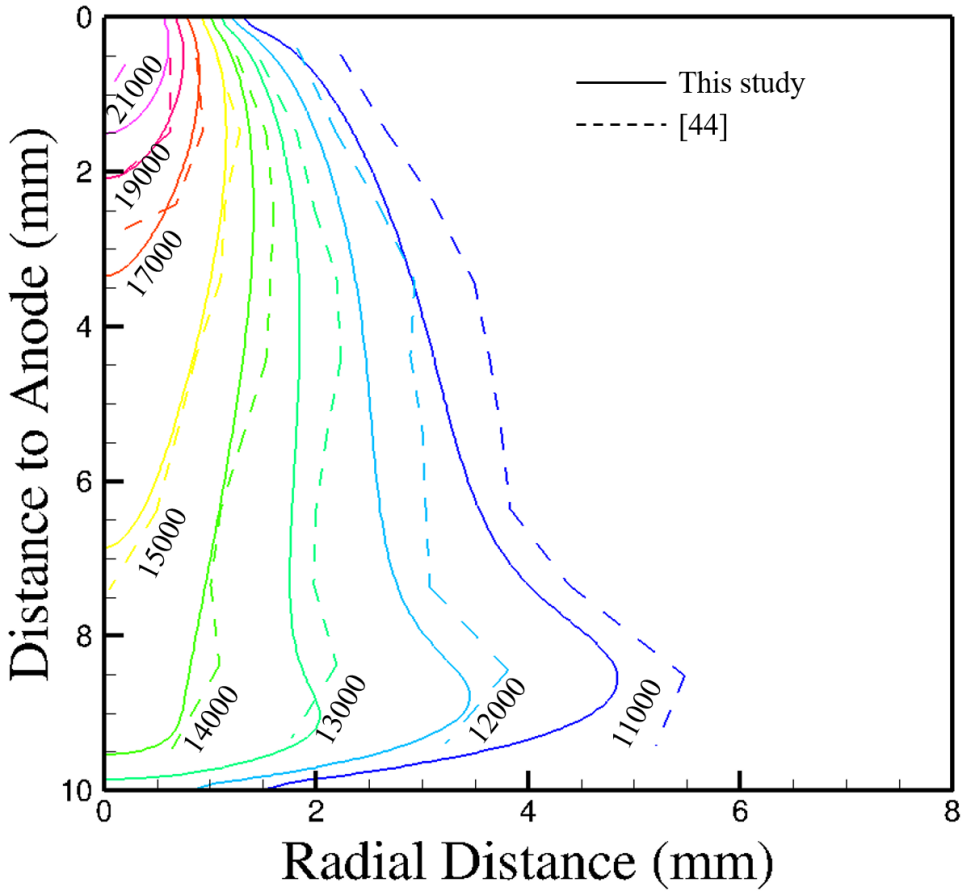


Figure 4.5: Comparison of the temperature distributions between electrodes

doi:10.6342/NTU202104312

4-2 Working Current

This section compares the thermal and flow characteristics of the DC plasma torch under the condition of a working currents ranging from 100 A to 200 A and a fixed inlet flow rate of 140 SLM.

4-2-1 Time-Averaged Analysis

The distributions of time-averaged axial velocity, temperature, current density and tangential magnetic strength are shown from Figure 4.6 to Figure 4.9. The centerline profiles of the time-averaged axial velocity, temperature and electric current density are shown in Figure 4.10, Figure 4.11 and Figure 4.12, respectively. The outlet profiles of the time-averaged axial velocity, tangential velocity and temperature are shown in Figure 4.13, Figure 4.14 and Figure 4.15, respectively. From these distributions, a near-axisymmetric behavior is implied in the time-averaged analysis. The temperature distributions of the smallest working current case, (a), show a necking area is right downstream from the inlet region. It is clearly caused by the flow inertia under a weak electromagnetic force condition. The arc length decreases as the working current increases. The arc length is determined by the force balance between flow and electromagnetic fields. The increasing working current leads to the increases of electromagnetic force, so the arc length tends to decrease. The maximum of the axial

doi:10.6342/NTU202104312

velocity, temperature, current density and tangential magnetic strength increases as the working current increases. Meanwhile, the Lorentz force and Joule heat become larger when the working current increases, but they only significantly impact the flow in the region with high current density. In other words, the time-averaged arc behavior is able to be observed from the time-averaged analysis. The fluid in front of the cathode is relatively aerodynamic, because there is nearly no electric current, i.e., the Lorentz force vanishes. Because of the existence of electric current, the acceleration and heating region is arising between the cathode and anode. The axial velocity increases from the inlet region to the anode region, and the maximum speed occurs beneath the anode. Besides, the temperature and electric current density increase from the cathode region to the inlet region, and their maximums occur beneath the inlet region. The inlet flow carries the gas in low temperature into the torch, and the electrical conductivity near the inlet is much lower than its surroundings. Therefore, the electric current is forced to converge to the torch center which has a higher electrical conductivity than the space near the inlet, and the temperature starts to rise until the Joule heat and radiation loss become balanced. The axial velocity decreases after leaving the anode region, and the temperature and electric current density decrease after leaving the inlet region. The longer distance from the anode to the outlet, i.e., a larger region without acceleration and heating, the lower axial velocity, tangential velocity and temperature at the outlet.

doi:10.6342/NTU202104312

Hence, high working current is unable to deliver high velocity or temperature but the low ones at the outlet. From the outlet profiles, the maximum axial velocity and temperature at the outlet are at the centerline of the torch, and the maximum tangential velocity gradually shift toward the torch center as the working current increases.

doi:10.6342/NTU202104312

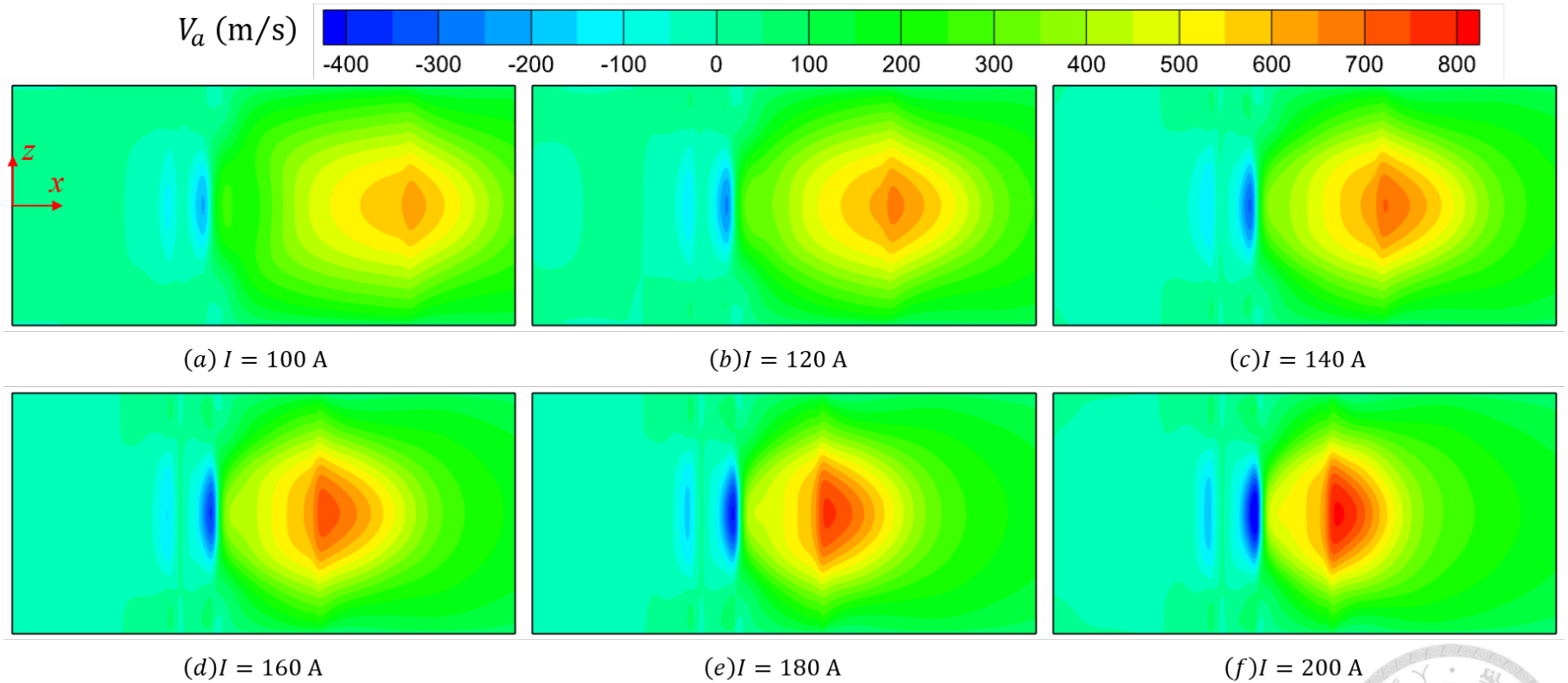


Figure 4.6: Time-averaged axial velocity distributions at $Q = 140$ SLM

doi:10.6342/NTU202104312

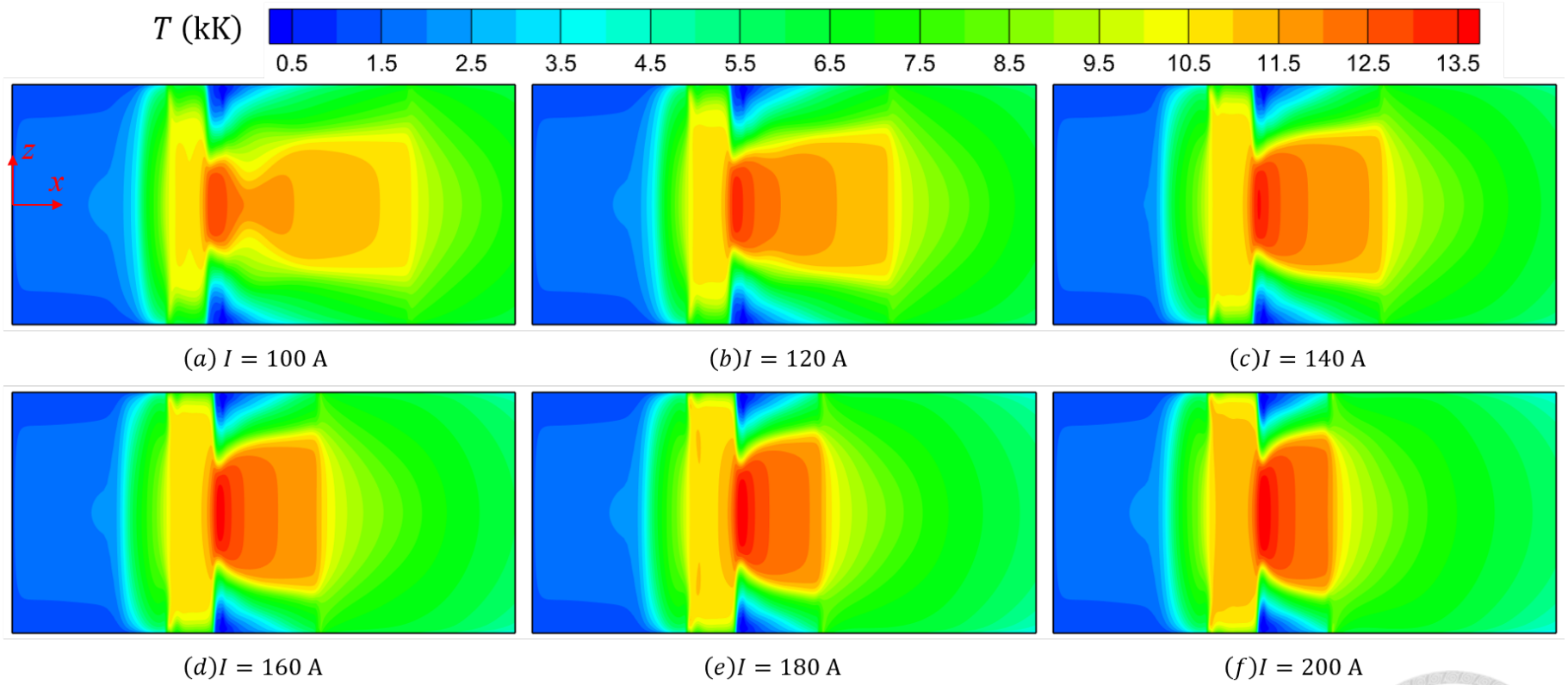


Figure 4.7: Time-averaged temperature distributions at $Q = 140$ SLM

doi:10.6342/NTU202104312

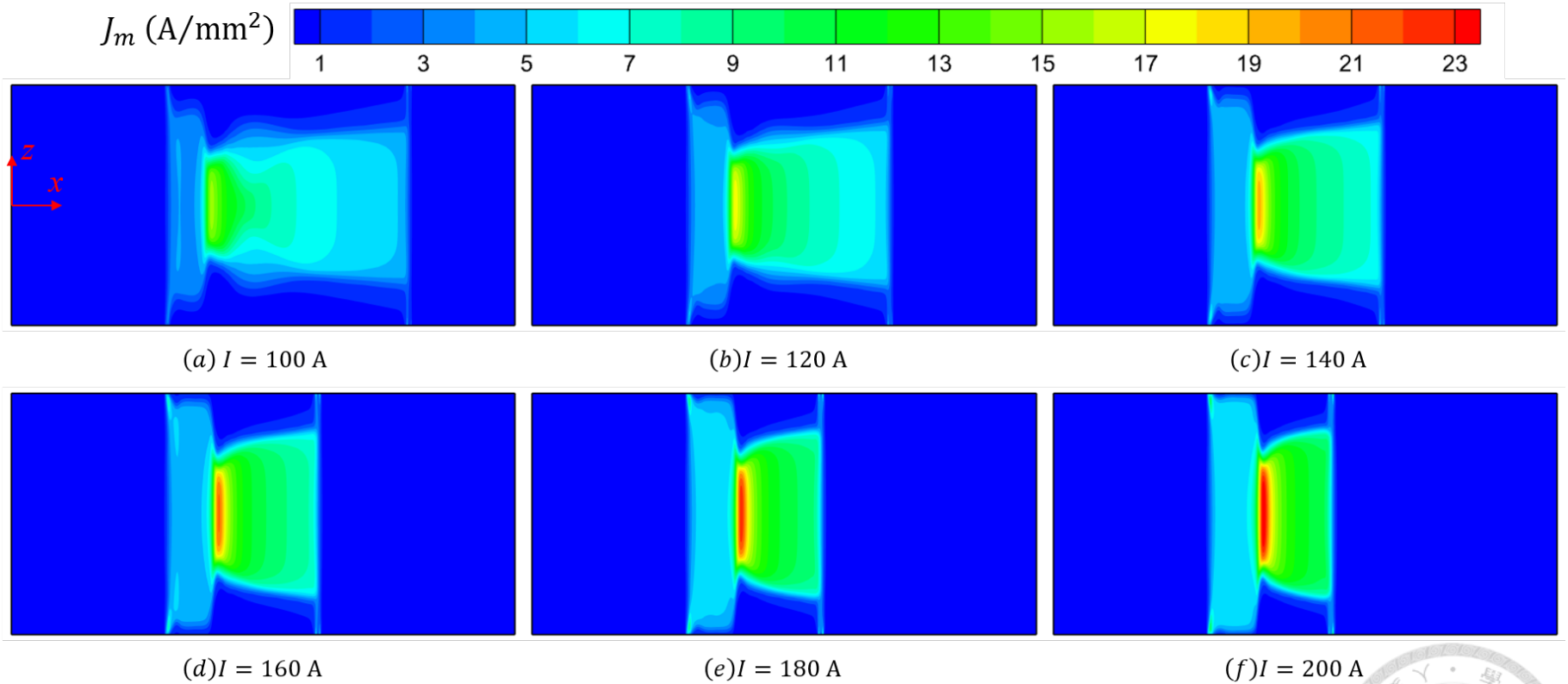


Figure 4.8: Time-averaged electric current density distributions at Q = 140 SLM

doi:10.6342/NTU202104312

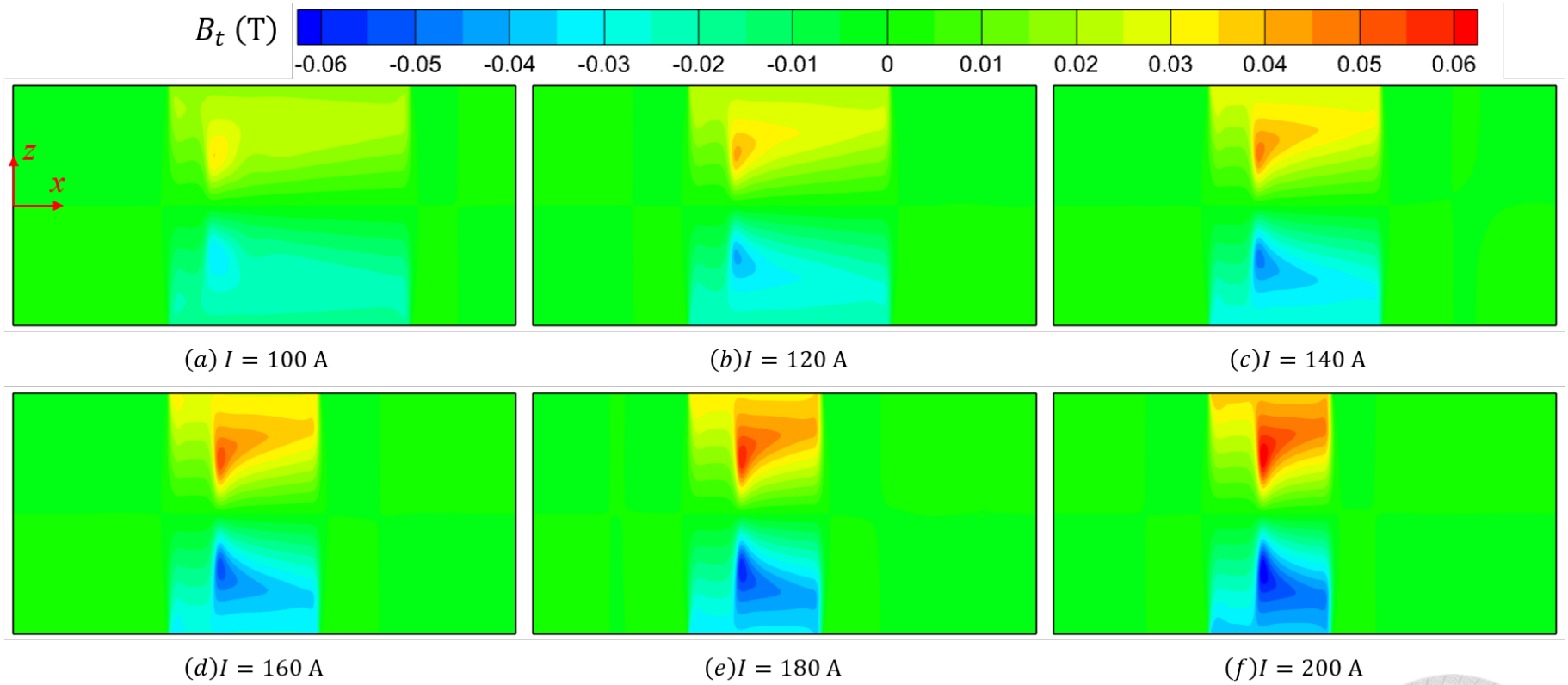


Figure 4.9: Time-averaged tangential magnetic field distributions at $Q = 140$ SLM

doi:10.6342/NTU202104312

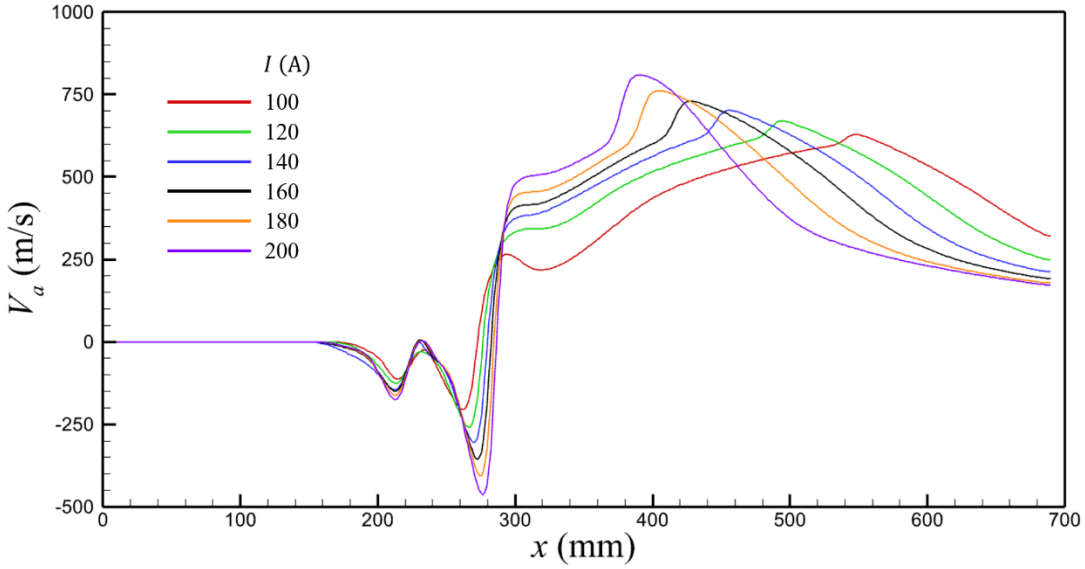


Figure 4.10: Centerline profile of time-averaged axial velocity at $Q = 140$ SLM

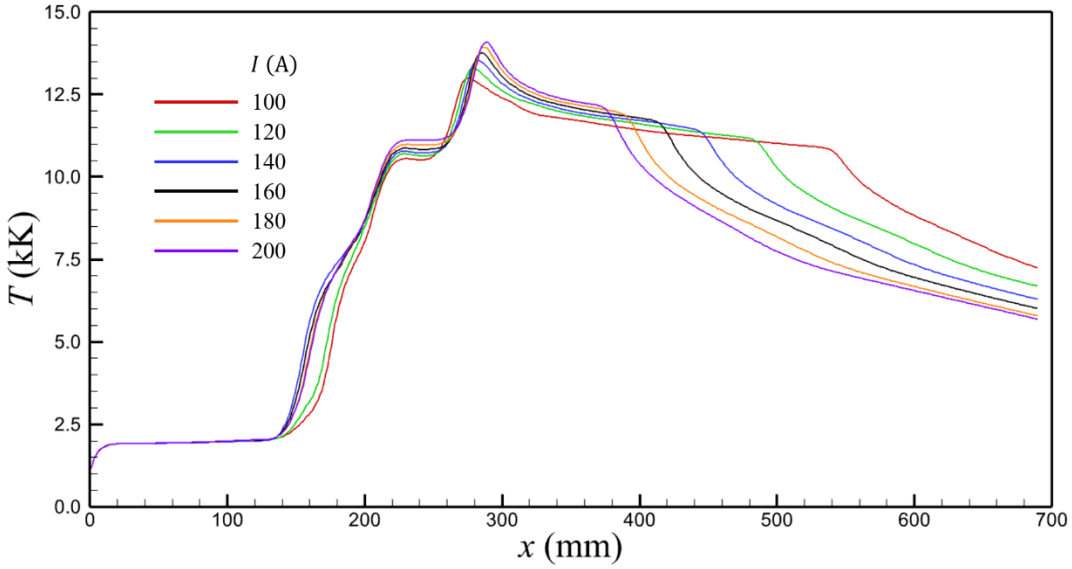


Figure 4.11: Centerline profile of time-averaged temperature at $Q = 140$ SLM

doi:10.6342/NTU202104312

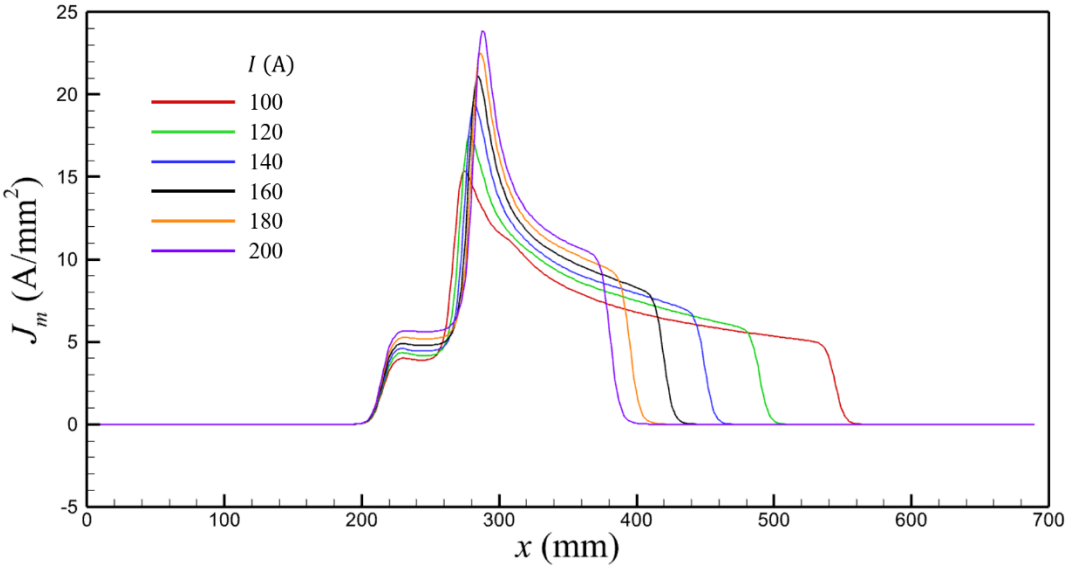


Figure 4.12: Centerline profile of time-averaged electric current density at $Q =$ 140 SLM

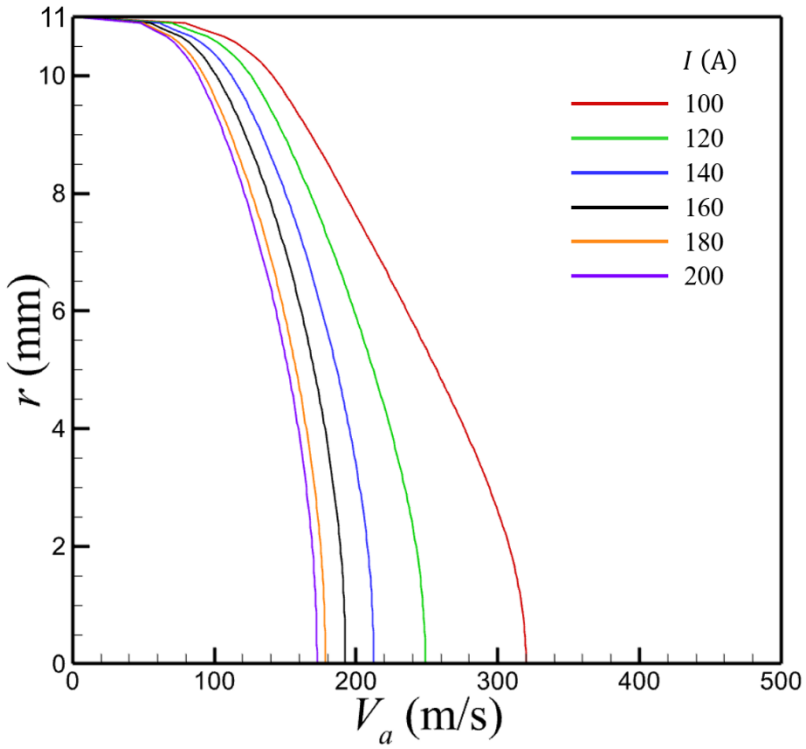


Figure 4.13: Outlet profile of time-averaged axial velocity at $Q = 140$ SLM

doi:10.6342/NTU202104312

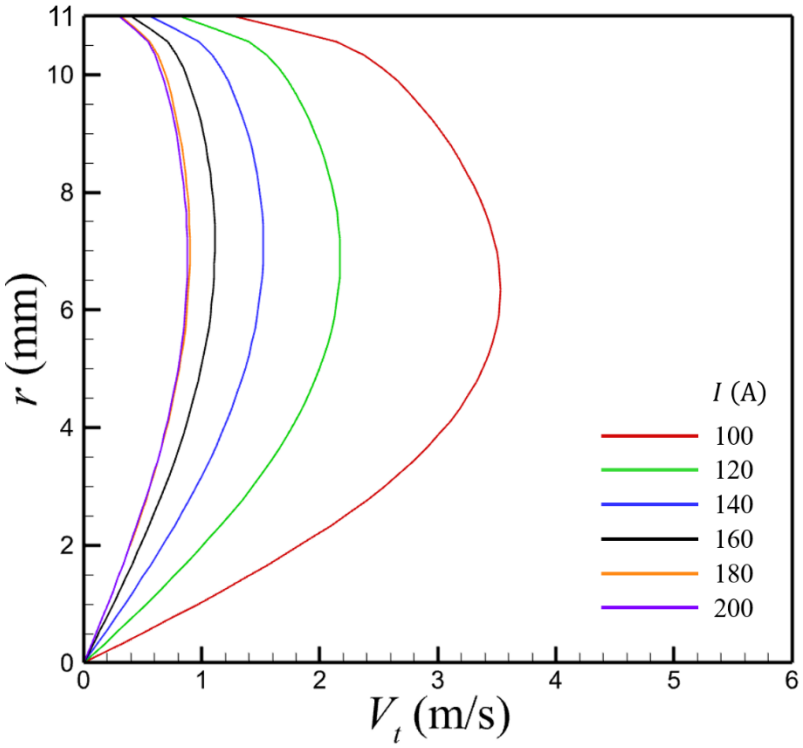


Figure 4.14: Outlet profile of time-averaged tangential velocity at $Q = 140$ SLM

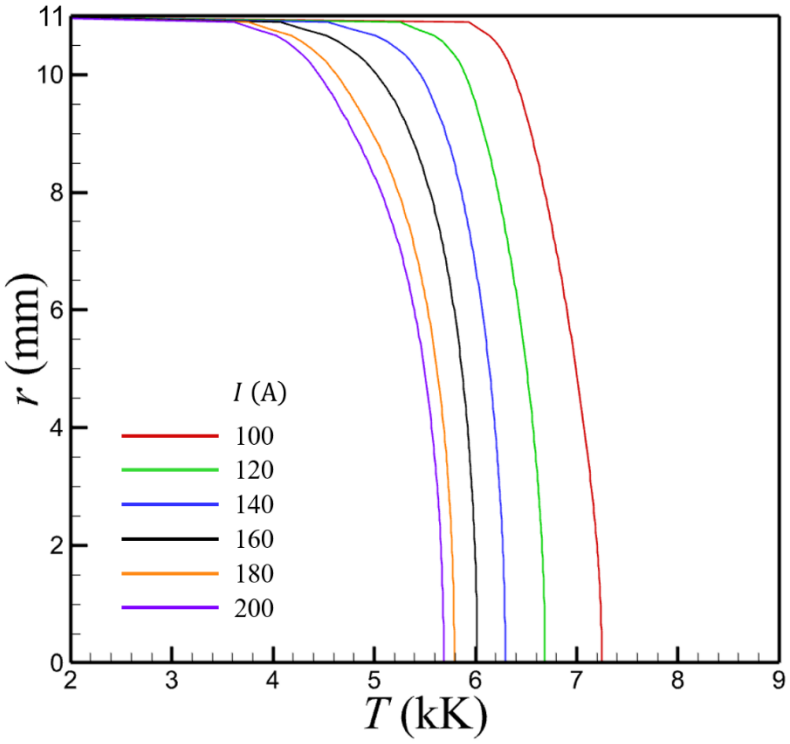


Figure 4.15: Outlet profile of time-averaged temperature at $Q = 140$ SLM

doi:10.6342/NTU202104312

4-2-2 Time History Analysis

In the numerical study, the time step size is 20 μs, and the circulating frequency of cathode spot is 1000 Hz, i.e., 1 ms per cathode spot cycle. The simulation time is 30 ms, i.e., 1500 time steps in total. The mean of a variable, ψ^m, at the outlet is defined in Eq. (81). The means of axial velocity, tangential velocity and temperature at the outlet and the voltage drop between the cathode and anode are shown from Figure 4.16 to Figure 4.19. The mean values gradually stabilize over time. As the working current increases, the time to achieve the stable condition also increases. From Figure 4.19, distinct periodic behavior of the voltage drop is observed for different working currents. The relatively significant voltage drop oscillations of the cases $I = 100\ \mathrm{A}$ and $120\ \mathrm{A}$ indicate low working current prone to enhance voltage drop fluctuations. The mean tangential velocities are also fluctuating with time, especially for small working current. The fast Fourier transform (FFT) of the voltage drop over time excluding the most fluctuating case, i.e., $I = 100\ \mathrm{A}$ and $Q = 140\ \mathrm{SLM}$, is given in Figure 4.20. It is obvious that the growth of the working current tends to reduce the peaks of frequencies. The fundamental frequencies of different working currents seem to vary among the investigated working currents. The temperature and current density distributions over time inside the torch at different cross sections are illustrated in Figure 4.21 and Figure 4.22. The leftmost cross section is at the cathode location, so the cathode spot is

doi:10.6342/NTU202104312

observed the high temperature region in Figure 4.21. The second cross section from the left is at the inlet location, and the temperature contour shows a temperature-contracted area. And, the circulation frequency of the high-temperature region is higher than that of the cathode spot. After the inlet location, there is no obvious change over time in the temperature distributions. From Figure 4.22, the high electric current density also indicates the position of the cathode spot in the leftmost cross section. An area of high current density appears in the second cross section from the left with a higher circulating frequency than that of the cathode spot. The second cross section form the right is located at the anode location. The high temperature region implies the arc root of the anode. The high-temperature region rotates in an opposite direction to the circulating direction of the cathode spot, and its frequency is lower than that of the cathode spot.

doi:10.6342/NTU202104312

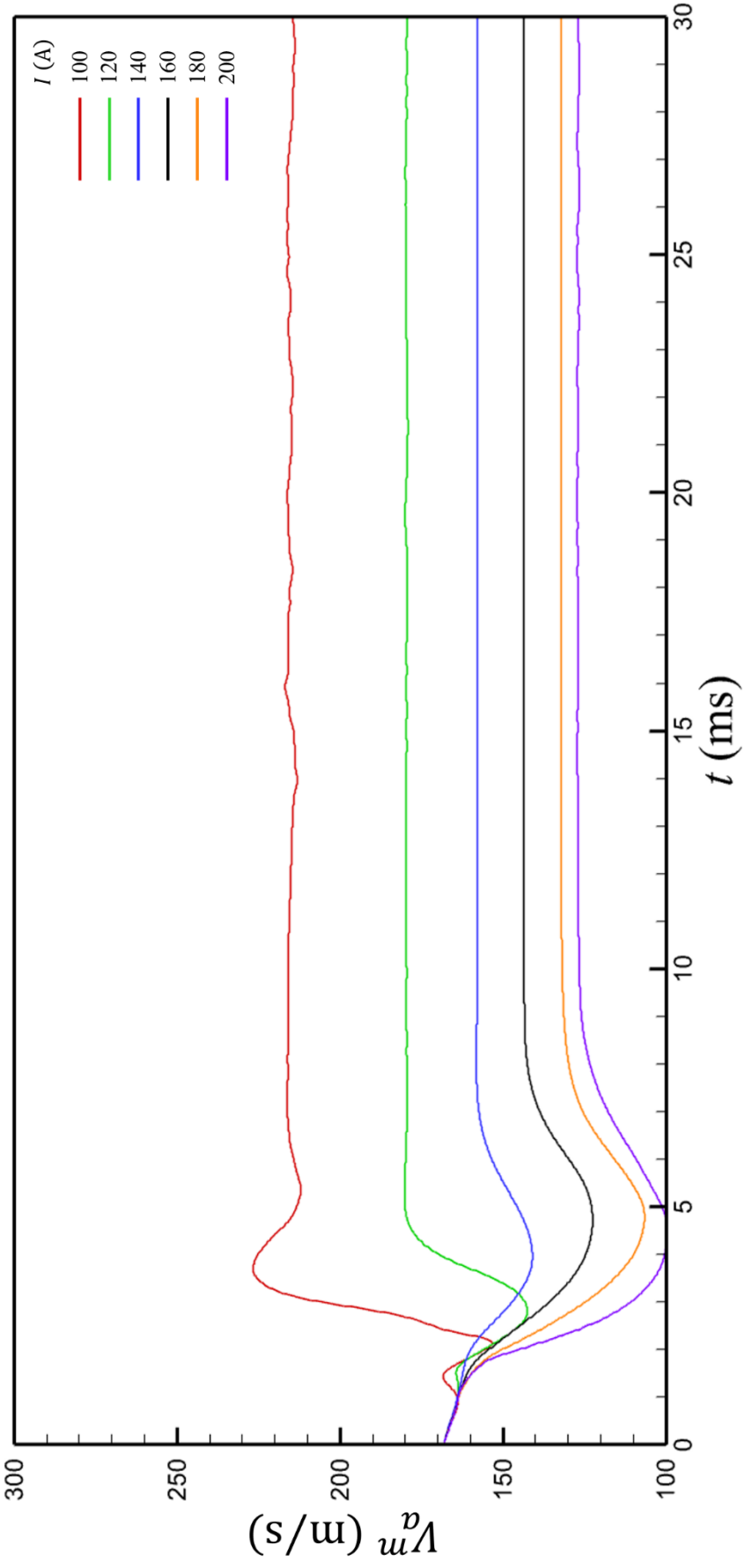


Figure 4.16: Time history of the mean axial velocity at the outlet at $Q = 140$ SLM

doi:10.6342/NTU202104312

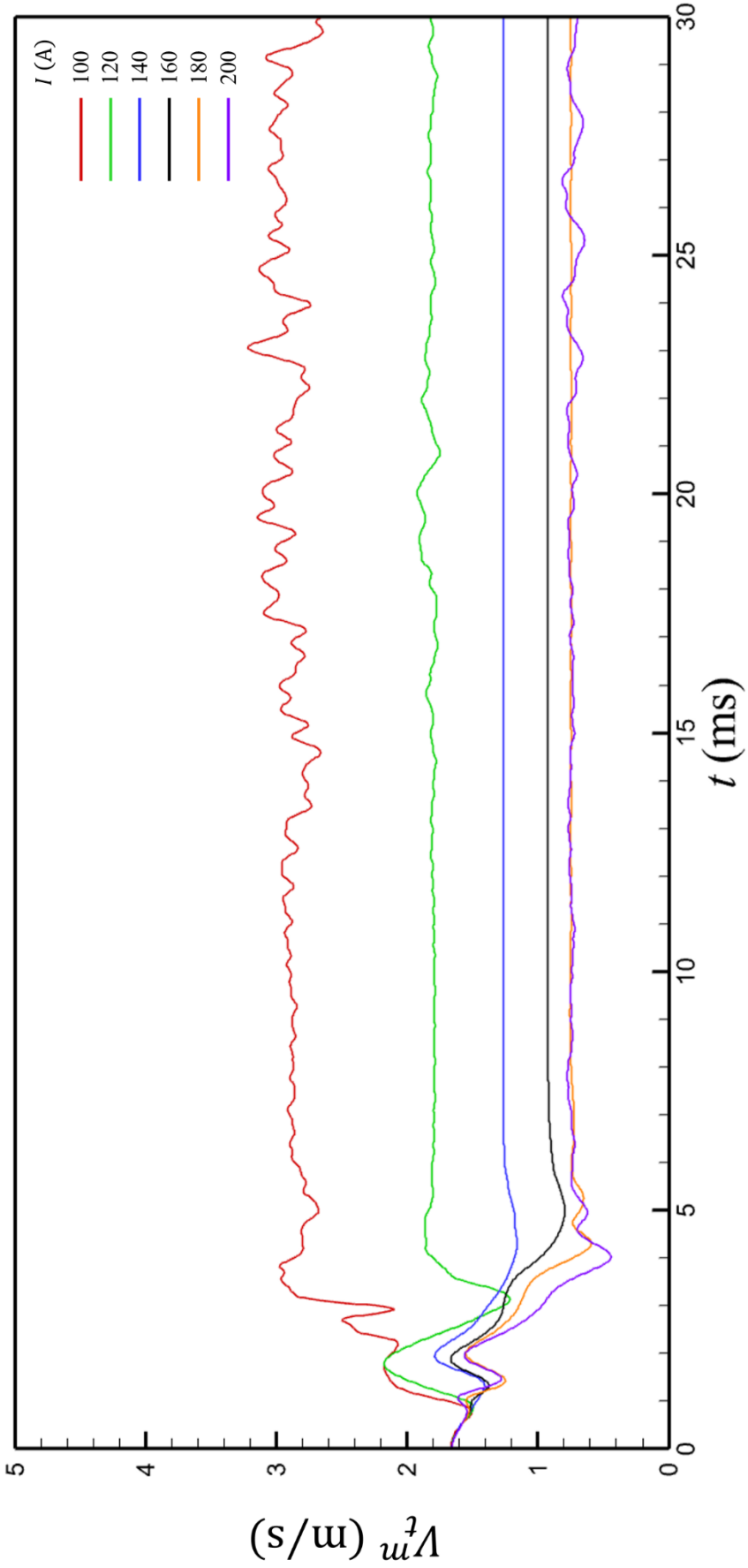


Figure 4.17: Time history of the mean tangential velocity at the outlet at $Q = 140$ SLM

doi:10.6342/NTU202104312

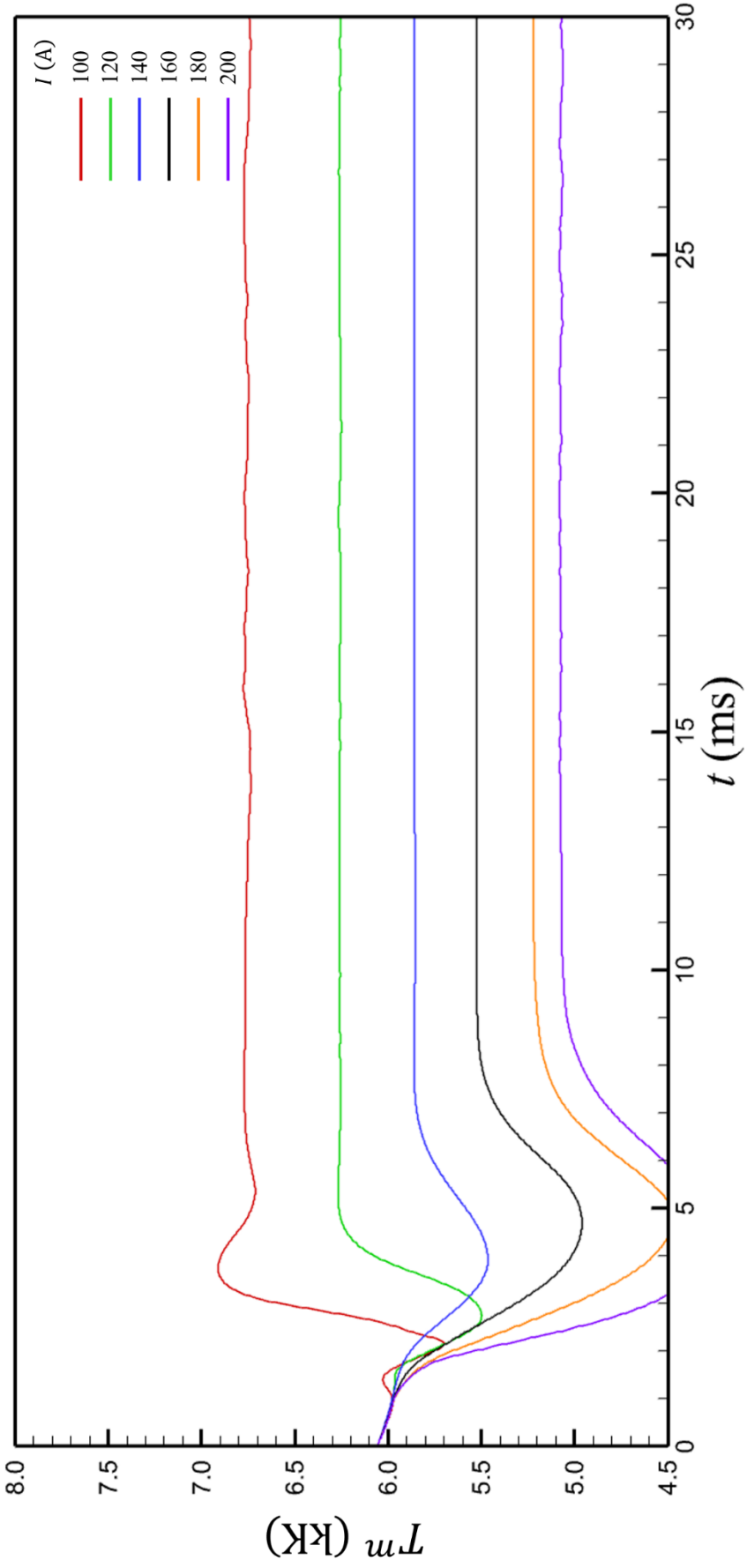


Figure 4.18: Time history of the mean temperature at the outlet at $Q = 140$ SLM

doi:10.6342/NTU202104312

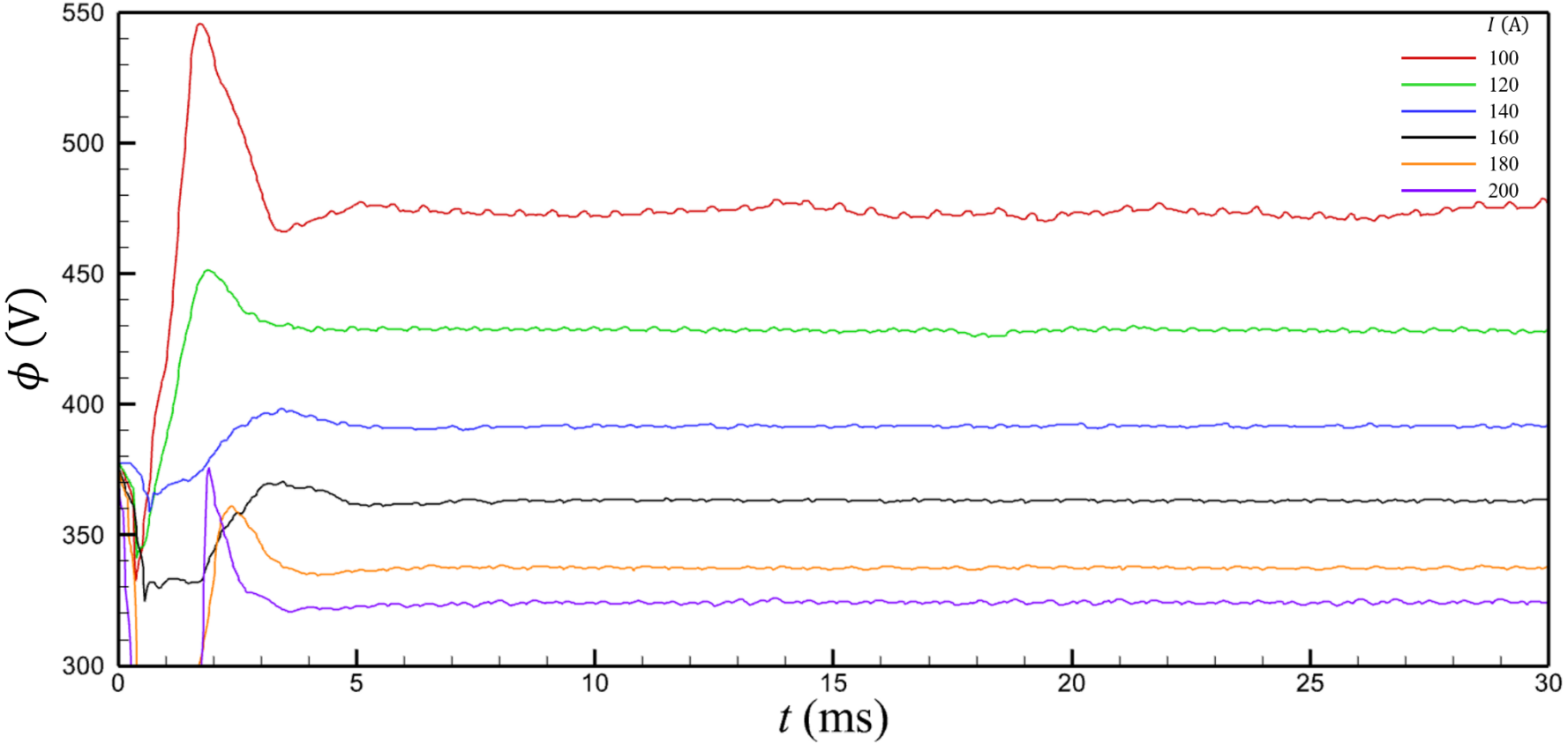


Figure 4.19: Time history of voltage drop at $Q = 140$ SLM

doi:10.6342/NTU202104312

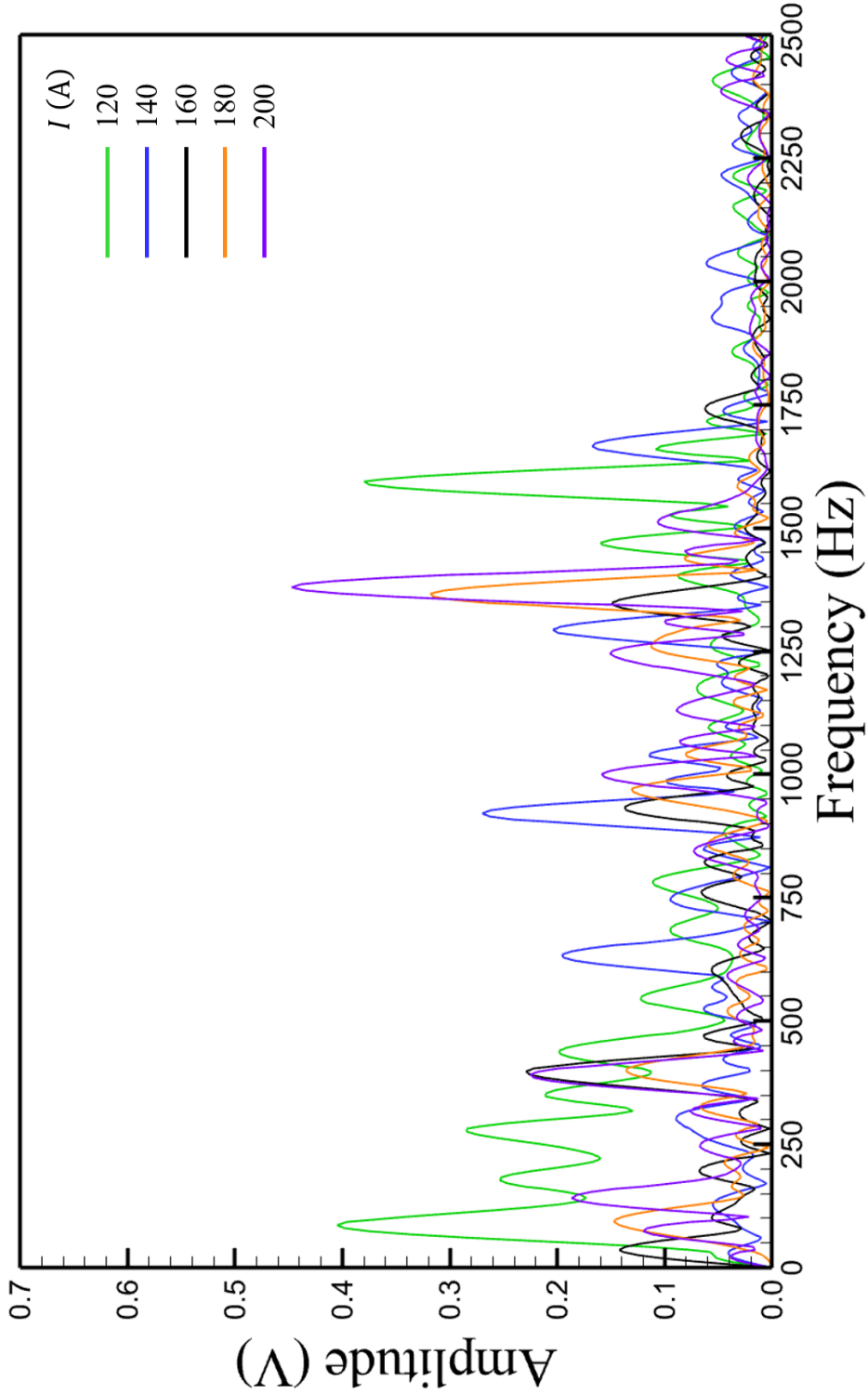


Figure 4.20: Fast Fourier transform of voltage drop at $Q = 140$ SLM

doi:10.6342/NTU202104312

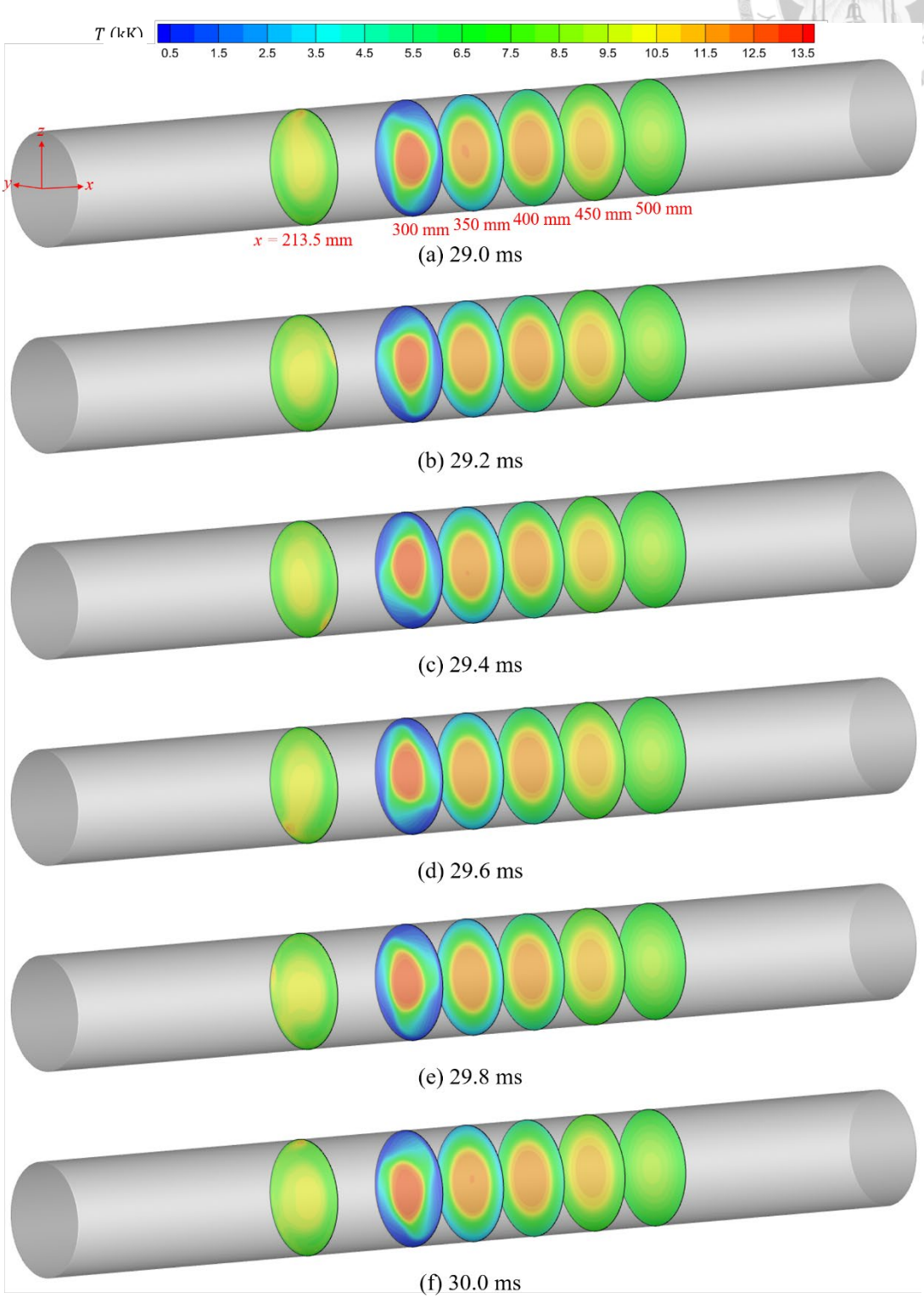


Figure 4.21: Temperature distributions inside the torch of different cross sections

doi:10.6342/NTU202104312

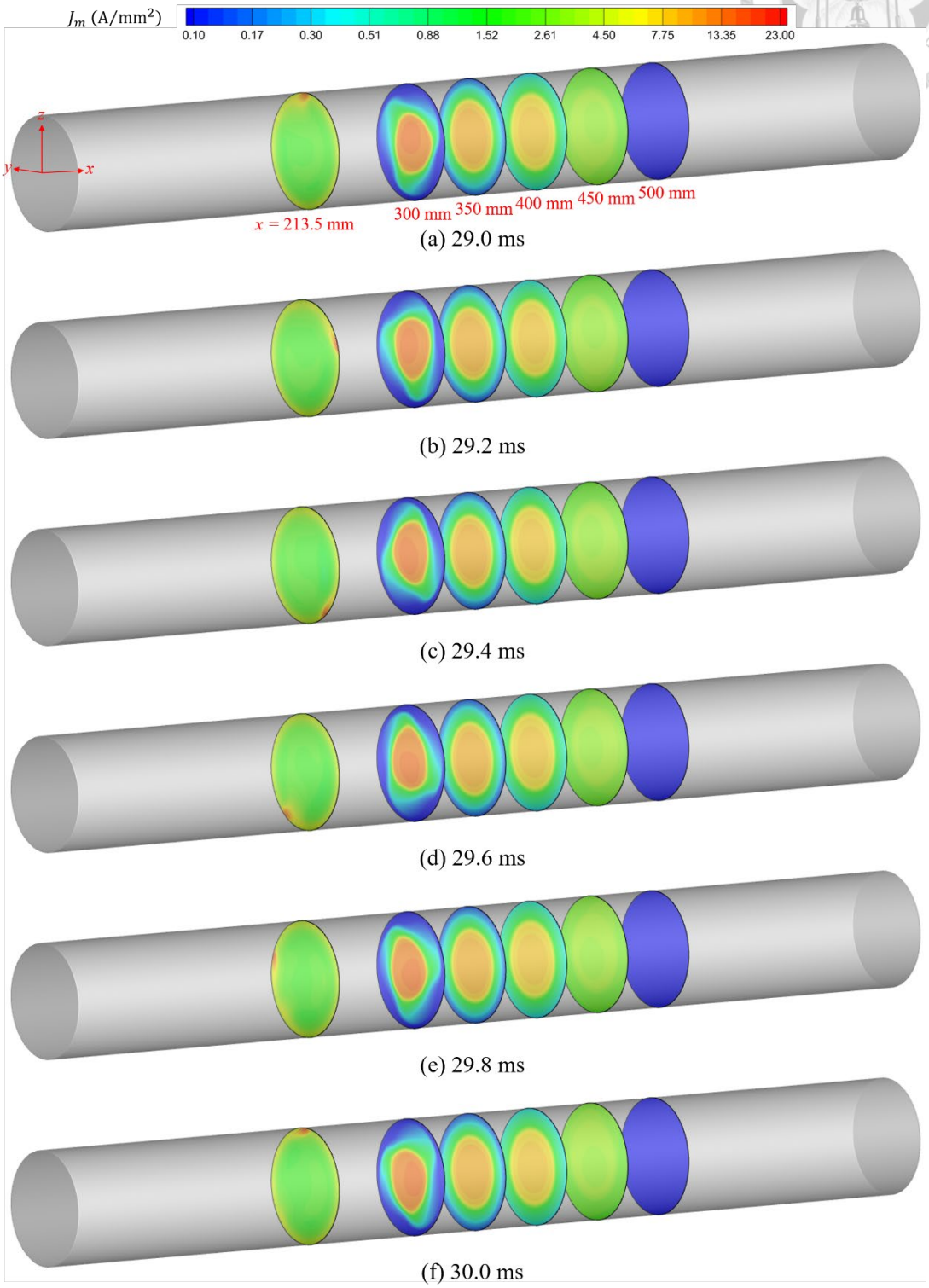


Figure 4.22: Electric current density distributions inside the torch of different cross sections

doi:10.6342/NTU202104312



4-3 Inlet Flow Rate

This section compares the thermal and flow characteristics of the DC plasma torch under the condition of an inlet flow rate ranging from 100 SLM to 200 SLM and a fixed working current of 140 A.

4-3-1 Time-Averaged Analysis

The distributions of time-averaged axial velocity, temperature, current density and tangential magnetic strength are shown from Figure 4.23 to Figure 4.26. The centerline profiles of the time-averaged axial velocity, temperature and current density are shown in Figure 4.27, Figure 4.28 and Figure 4.29, respectively. The outlet profiles of the time-averaged axial velocity, tangential velocity and temperature are shown in Figure 4.30, Figure 4.31 and Figure 4.32, respectively. A near-axisymmetric distribution is observed in the time-averaged analysis. From these distributions, the arc length increases as the inlet flow rate increases. The increase of inlet flow rate implies the increase of flow drag. The maximum axial velocity increases as the inlet flow rate increases, but the maximum temperature, current density and tangential magnetic strength show no significant change due to the fixed working current. The acceleration and heating region is mainly located between the cathode and the anode. The maximum axial velocity occurs at the anode location. The maximum temperature and current density occur at

doi:10.6342/NTU202104312

the inlet location. The case of high inlet flow rate shows a necking region right downstream from the inlet region. The reason is the flow inertia with high inflow speed is unable to be strongly restricted by the electromagnetic force. The axial velocity decreases after leaving the anode region, and the temperature and current density decrease after leaving the inlet region. The gradient of the axial velocity and temperature after leaving the anode region are similar in different inflow cases, because they have a similar electromagnetic field. Figure 4.28 represents that the maximum temperature of different inlet flow rates is almost the same, so the outlet temperature is basically decided by the convective heat transfer which is governed by the axial velocity. The higher inlet flow rate, the higher axial velocity, tangential velocity and temperature at the outlet. The inlet flow rate directly influences the flow characteristics at the outlet. From Figure 4.30, Figure 4.31 and Figure 4.32, the maximum axial velocity and temperature at the outlet are located in the centerline of the torch, and the maximum tangential velocity shows no significantly shifting as displayed in Figure 4.14.

doi:10.6342/NTU202104312

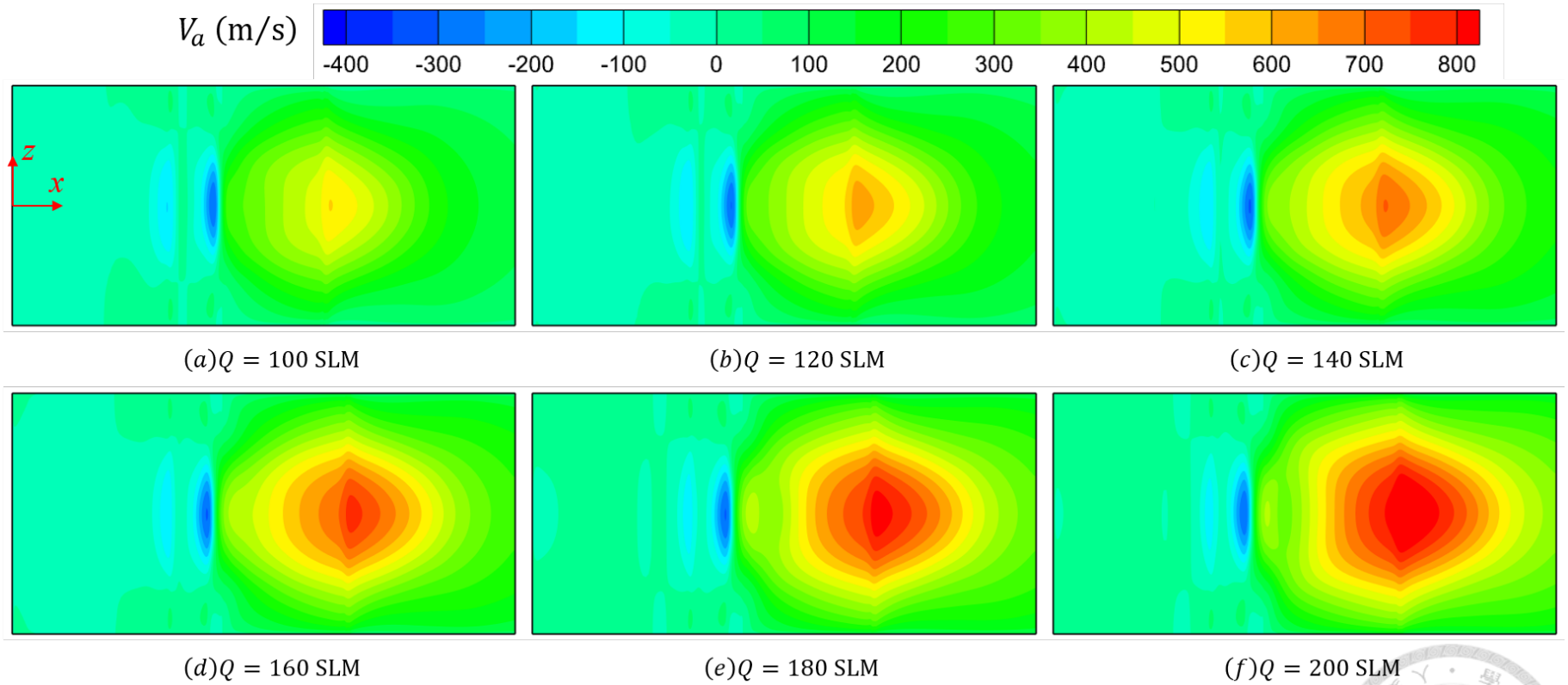


Figure 4.23: Time-averaged axial velocity distributions at $I = 140$ A

doi:10.6342/NTU202104312

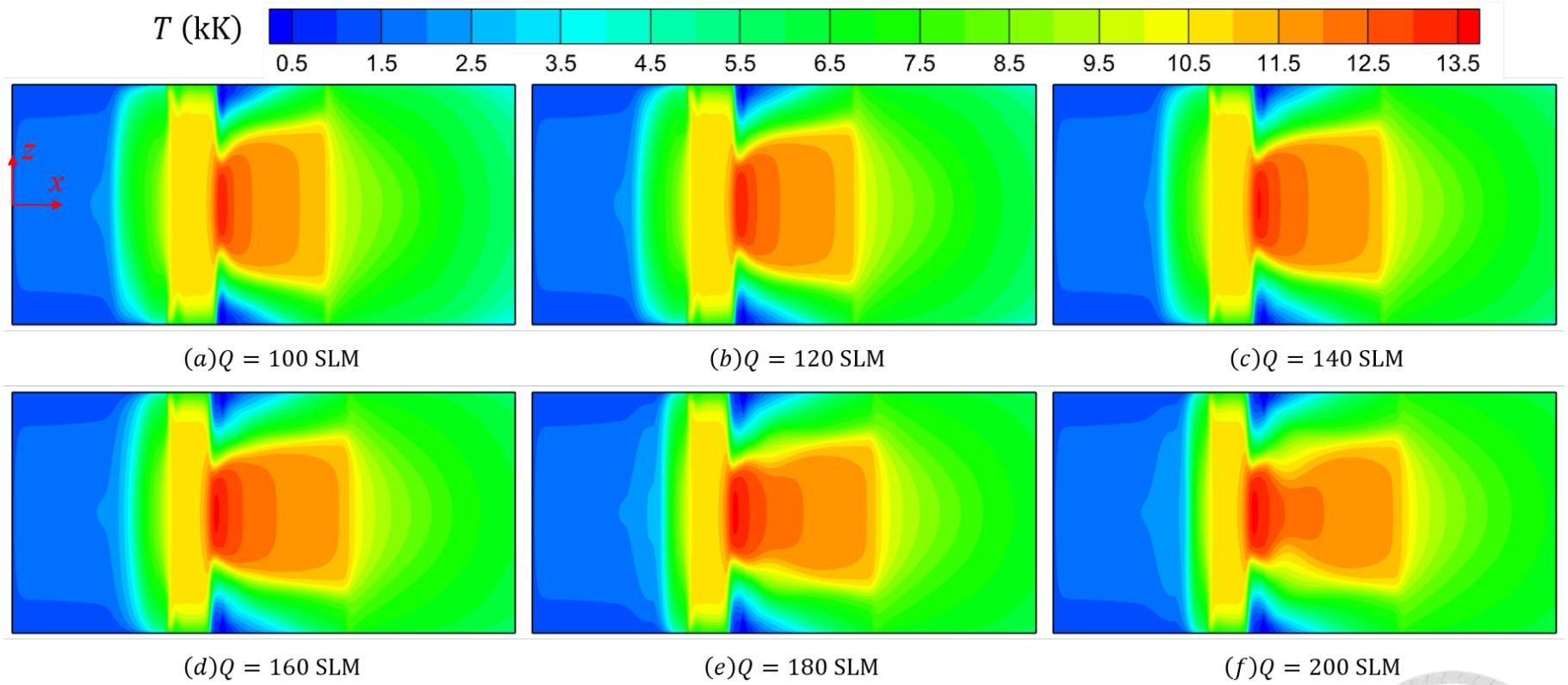


Figure 4.24: Time-averaged temperature distributions at $I = 140$ A

doi:10.6342/NTU202104312

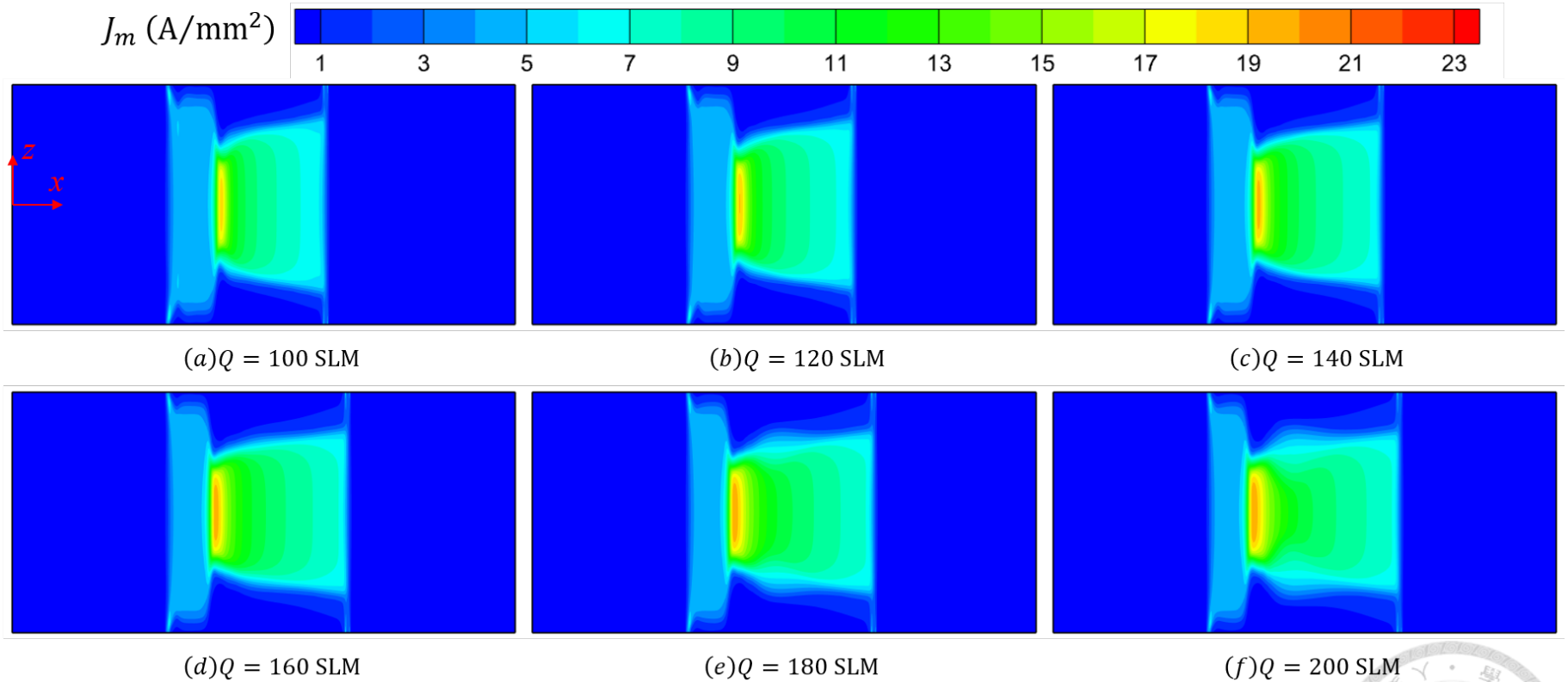


Figure 4.25: Time-averaged electric current density distributions at $I = 140$ A

doi:10.6342/NTU202104312

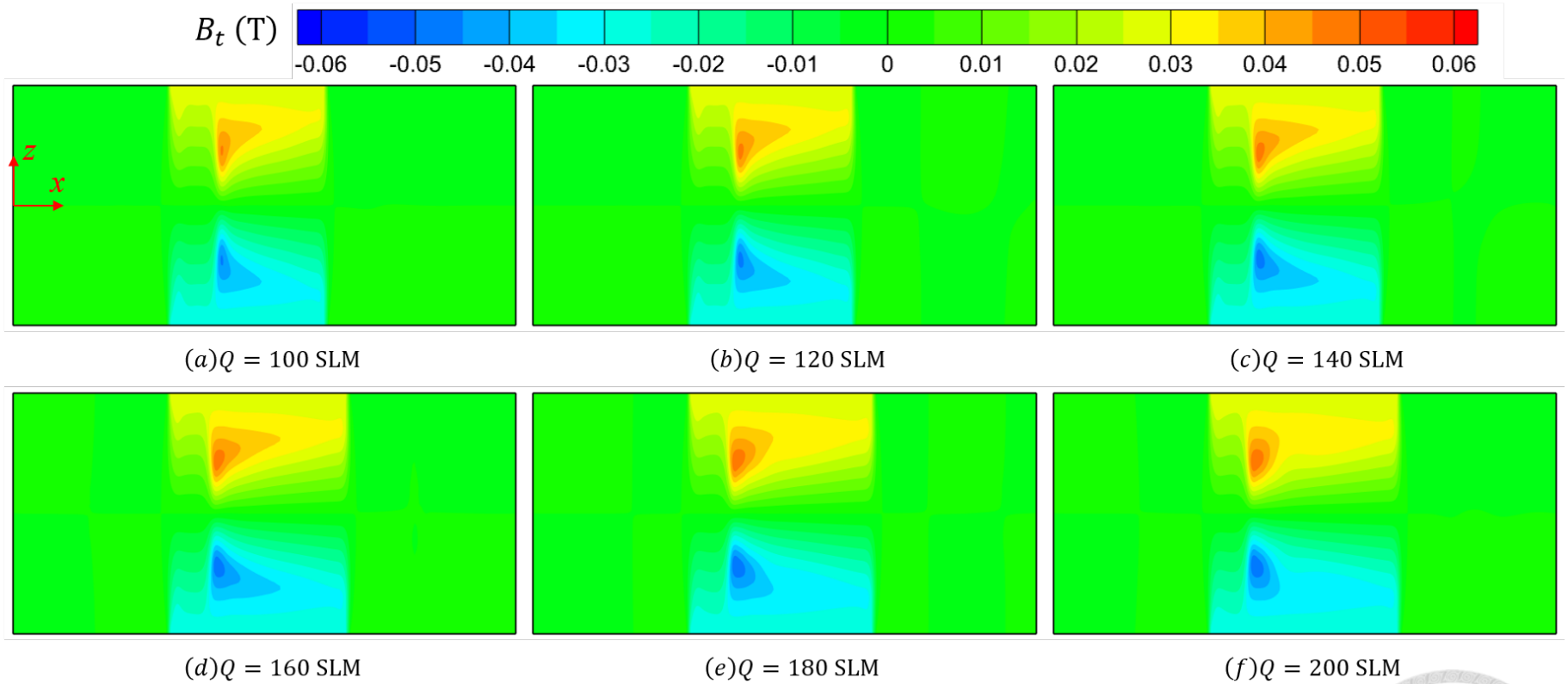


Figure 4.26: Time-averaged tangential magnetic field distributions at $I = 140$ A

doi:10.6342/NTU202104312

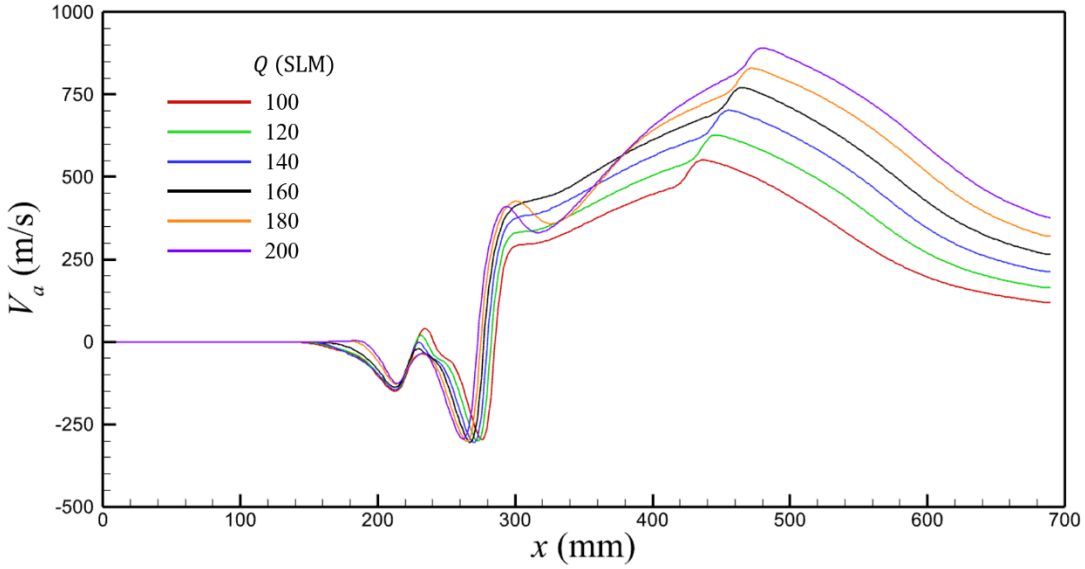


Figure 4.27: Centerline profile of time-averaged axial velocity at $I = 140$ A

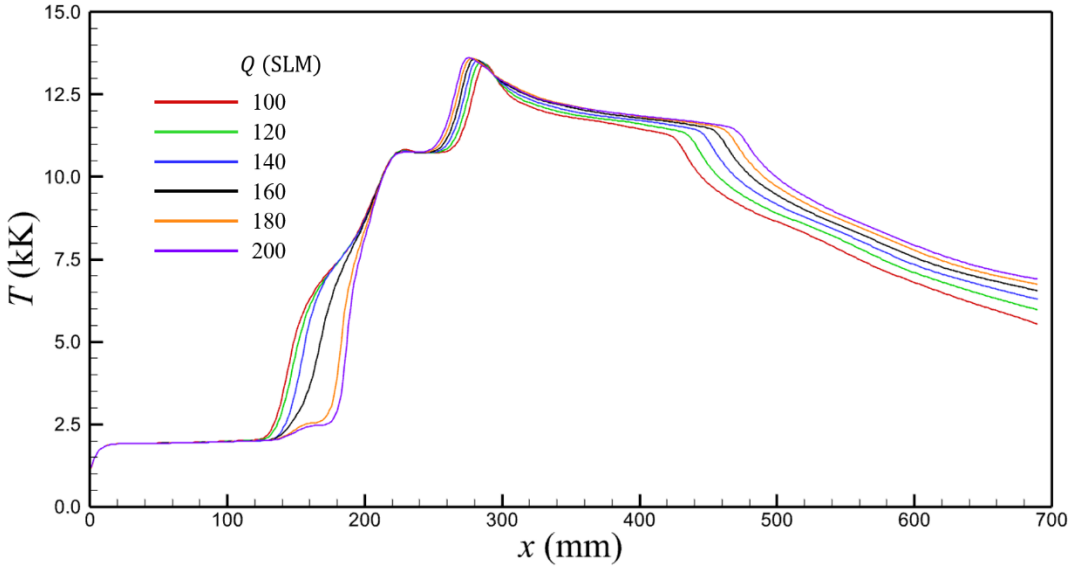


Figure 4.28: Centerline profile of time-averaged temperature at $I = 140$ A

doi:10.6342/NTU202104312

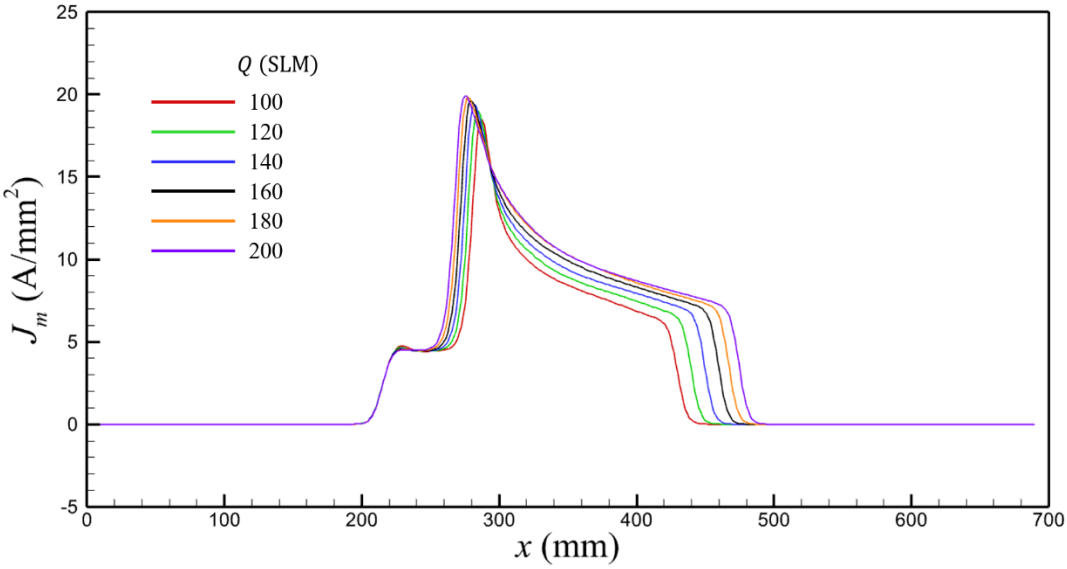


Figure 4.29: Centerline profile of time-averaged electric current density at $I = 140$ A

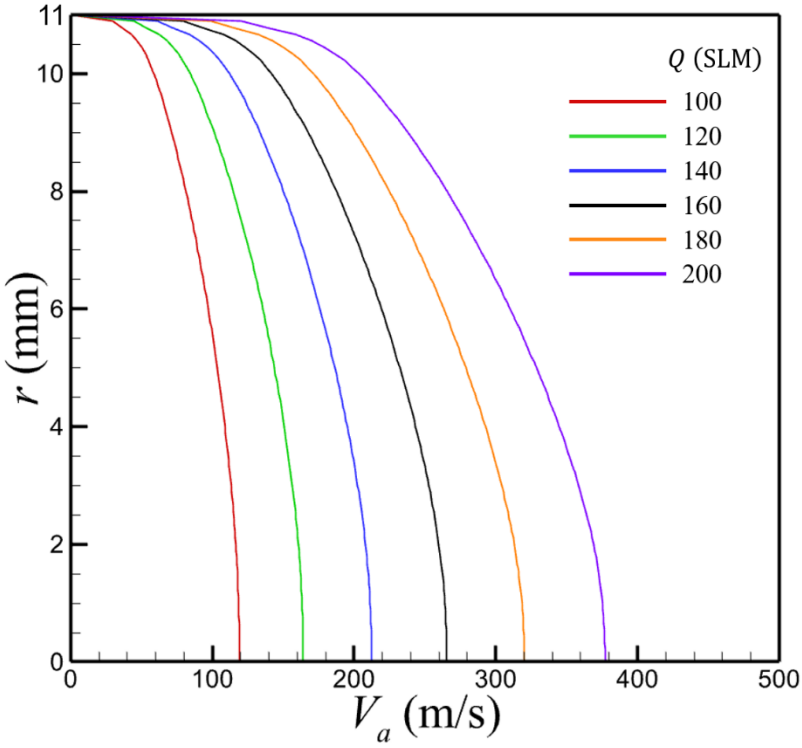


Figure 4.30: Outlet profile of time-averaged axial velocity at $I = 140$ A

doi:10.6342/NTU202104312

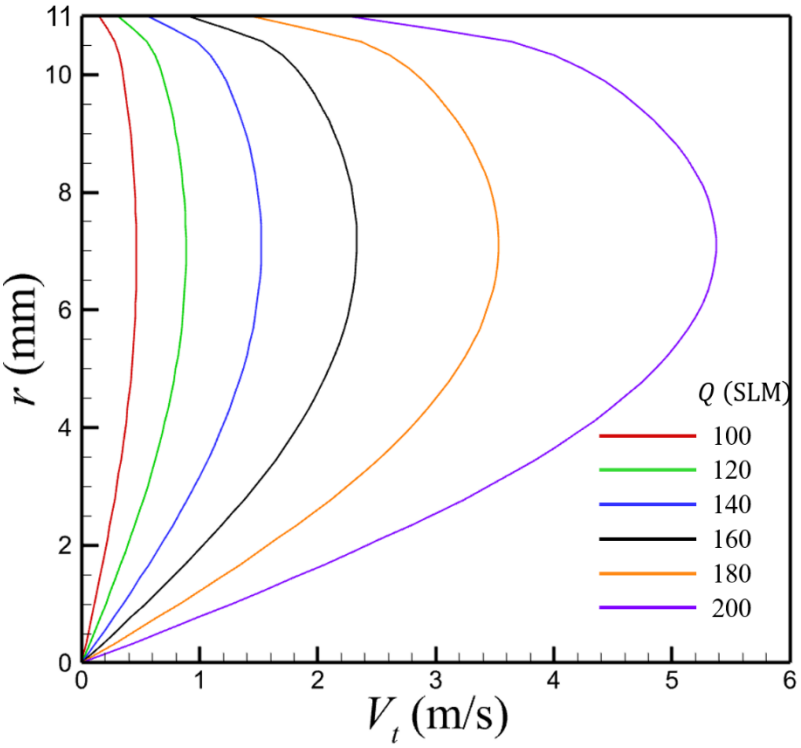


Figure 4.31: Outlet profile of time-averaged tangential velocity at $I = 140$ A

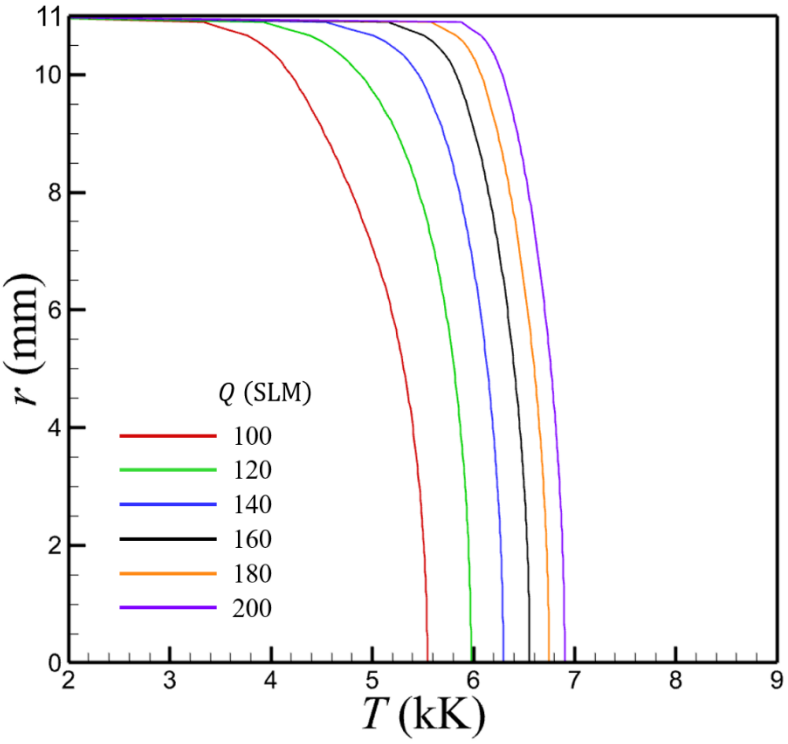


Figure 4.32: Outlet profile of time-averaged temperature at $I = 140$ A

doi:10.6342/NTU202104312

4-3-2 Time History Analysis

In this study, the time step size is 20 μs and the circulating frequency of cathode spot mentioned is 1000 Hz, i.e., 1 ms per cycle. The simulation time is 30 ms, i.e., 1500 time steps in total. The mean of a physical variable, ψ^m, at the outlet is defined in Eq. (81). The mean axial velocity, tangential velocity and temperature at the outlet and the voltage drop between the cathode and anode are shown from Figure 4.33 to Figure 4.36. These mean values gradually stabilize over time. As the inlet flow rate increases, the elapsed time to stable condition decreases. The relatively significant oscillations of the cases $Q = 180$ SLM and 200 SLM indicate their voltage drops with little periodicity when compared to other cases. The mean tangential velocity is also fluctuating at the end time. The FFT of the voltage drop over time excluding the most fluctuating case, $I = 140$ A and $Q = 200$ SLM, is given in Figure 4.37. The increase of flow rate tends to smooth and reduce the peaks of various frequencies.

doi:10.6342/NTU202104312

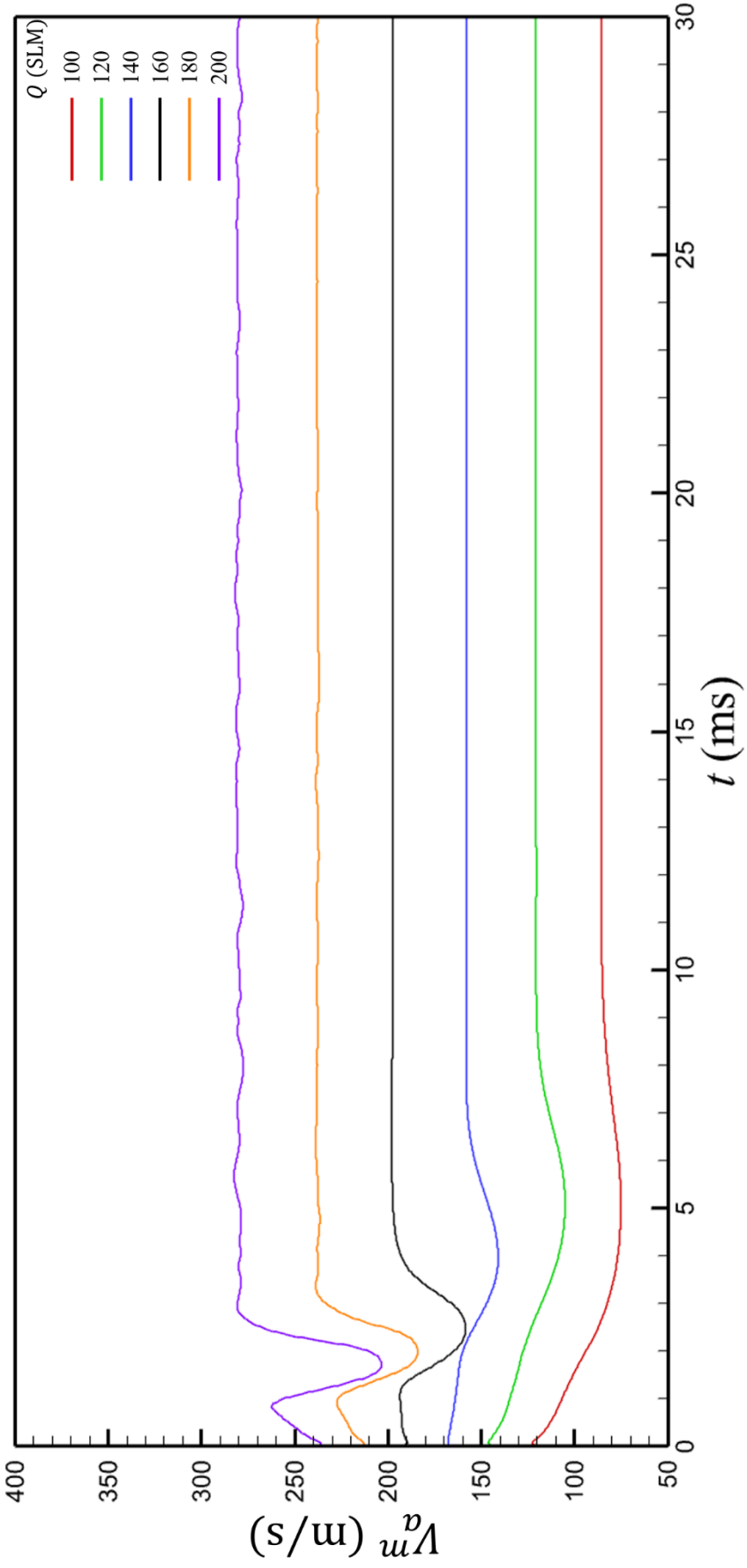


Figure 4.33: Time history of the mean axial velocity at the outlet at I = 140 A

doi:10.6342/NTU202104312

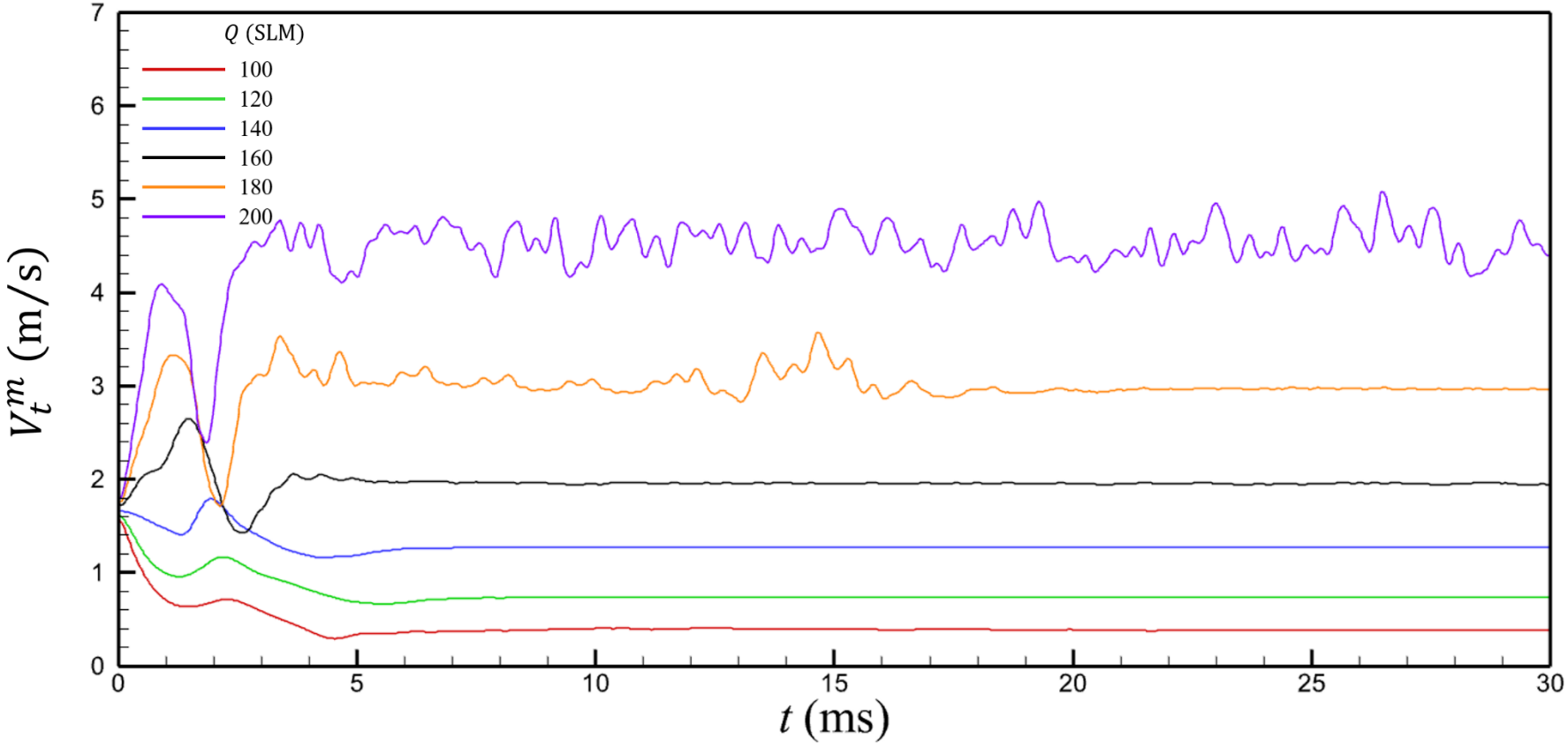


Figure 4.34: Time history of the mean tangential velocity at the outlet at $I = 140$ A

doi:10.6342/NTU202104312

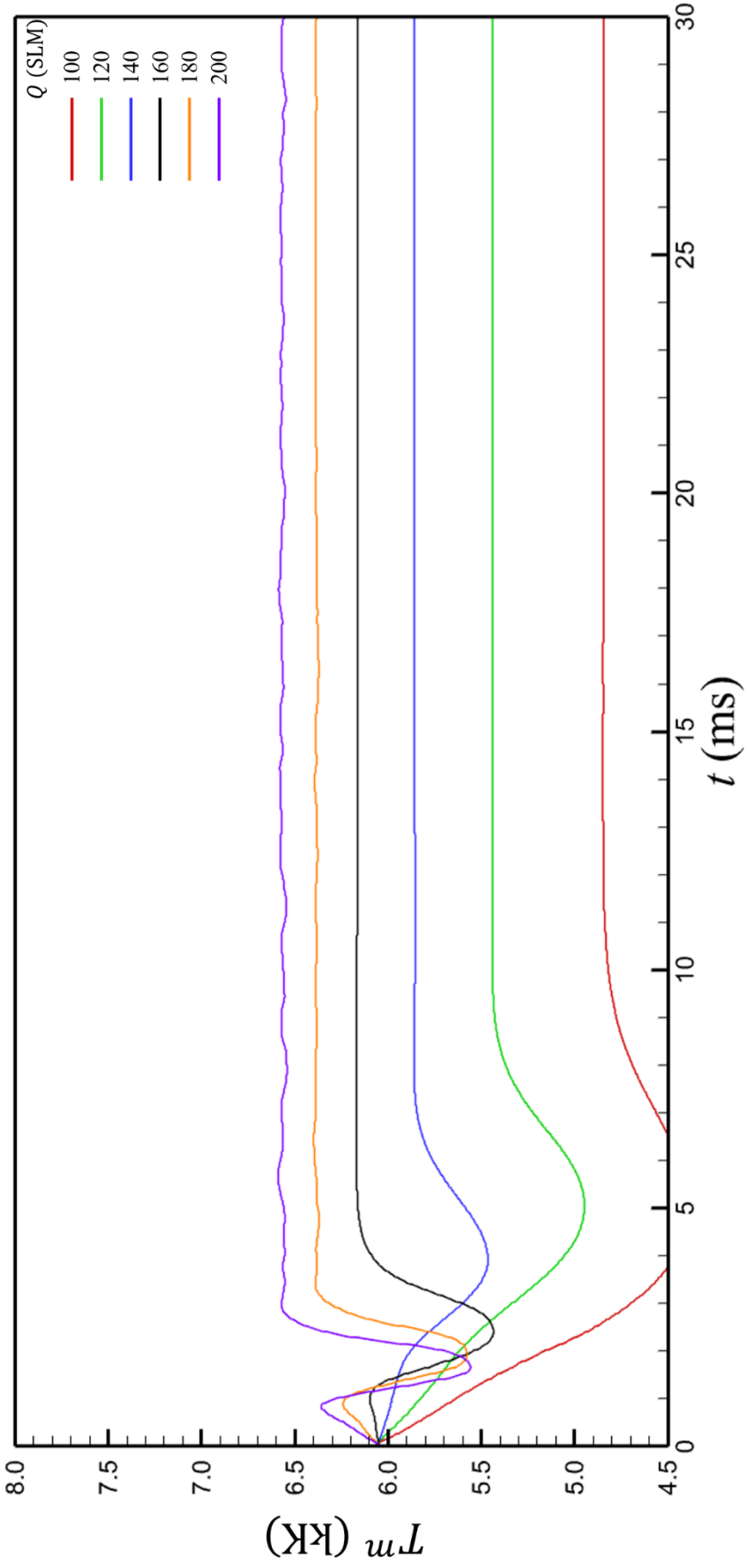


Figure 4.35: Time history of the mean temperature at the outlet at $I = 140$ A

doi:10.6342/NTU202104312

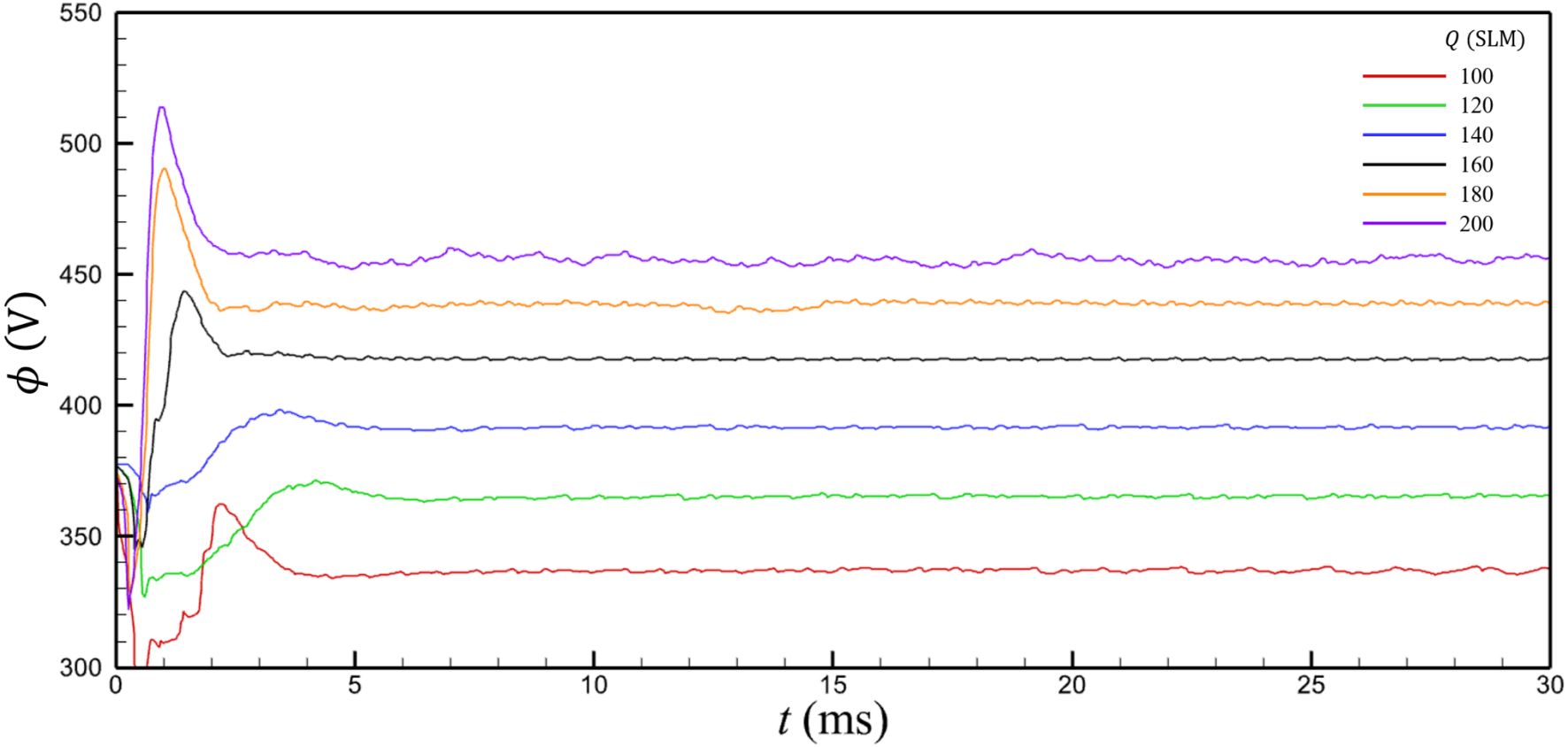


Figure 4.36: Time history of voltage drop at $I = 140$ A

doi:10.6342/NTU202104312

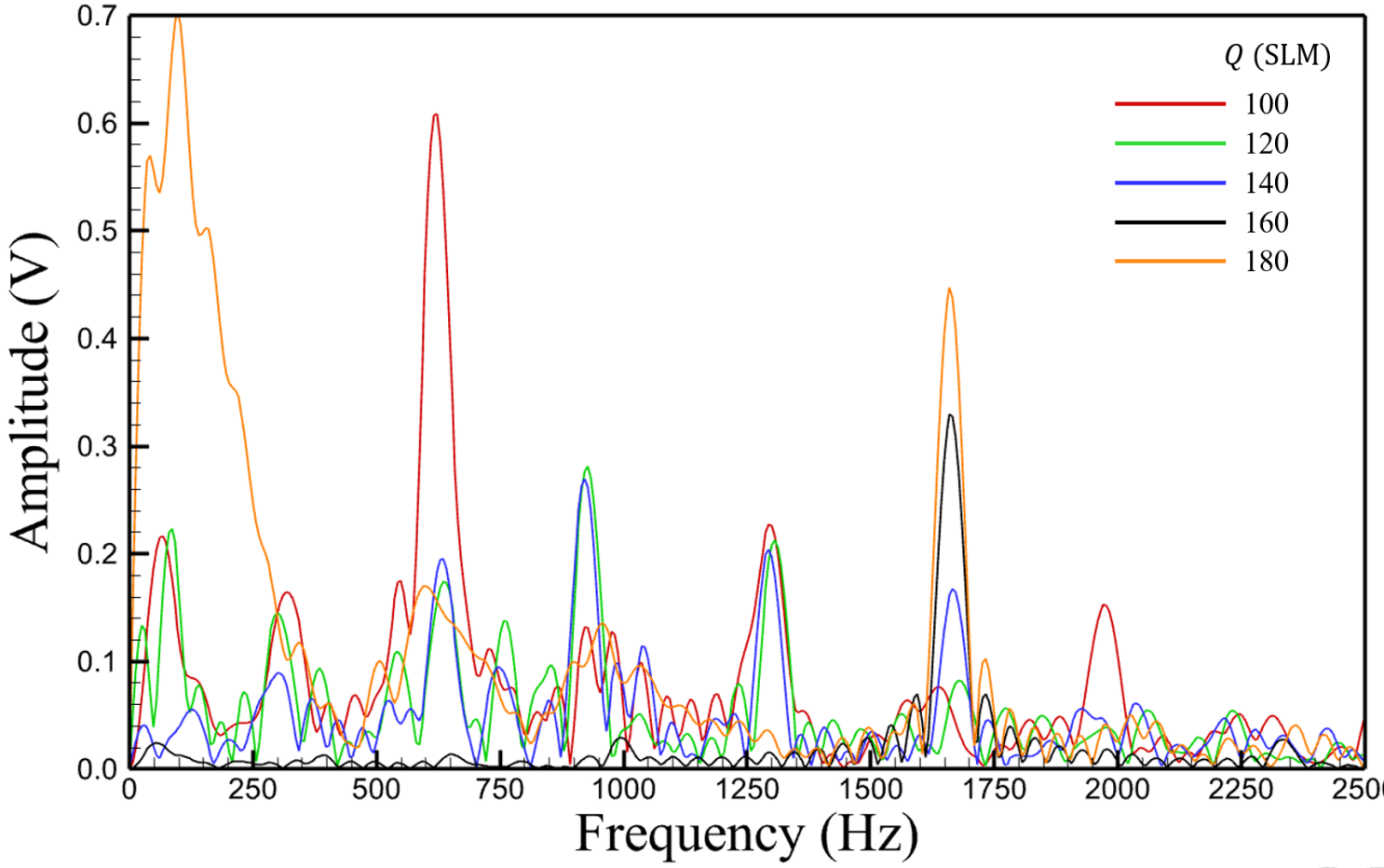


Figure 4.37: Fast Fourier transform of voltage drop at $I = 140$ A

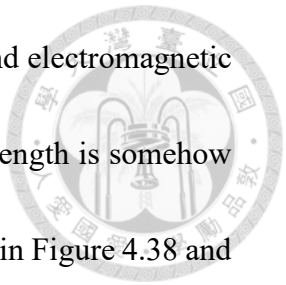
doi:10.6342/NTU202104312

4-4 Discussion

There is an electric arc which connects the circulating cathode spot and the ring anode region, and the flow acceleration is caused by Lorentz force acting on the gas to drive the gas into the centerline of the torch. Simultaneously, the gas temperature increases due to the Joule heat of the electric arc. Therefore, the flow characteristics in some ways are the results of the motion of the electric arc. The comparison of two different modellings, 2D steady axisymmetric modeling [2] and 3D unsteady modeling proposed in this study is presented in this section. The centerline profiles of axial velocity and temperature are compared in Figure 4.38 and Figure 4.39. The dependence of arc length on working current and inlet flow rate is shown in Figure 4.40. Figure 4.41 depicts the regression correlation of arc length. The dependence of the mean axial velocity at the outlet on working current and inlet flow rate is shown in Figure 4.42. Figure 4.43 depicts the regression correlation of the mean axial velocity at the outlet. The dependence of the mean tangential velocity at the outlet, working current and inlet flow rate is shown in Figure 4.44. Figure 4.45 depicts the regression correlation of the mean tangential velocity at the outlet. The dependence of the mean temperature at the outlet, working current and inlet flow rate is shown in Figure 4.46. Figure 4.47 depicts the regression correlation of the mean temperature at the outlet.

Because of the axisymmetric assumption, the cathode in the 2D axisymmetric

doi:10.6342/NTU202104312



modeling a circumferentially uniform region. The electric current and electromagnetic force are overestimated in the axisymmetric modeling, and the arc length is somehow underestimated when compared to this study. The centerline profiles in Figure 4.38 and Figure 4.39 show that the acceleration and heating in the 2D axisymmetric modeling are larger than in this study. Basically, both models have a similar arc and flow behavior as shown in Figure 4.40, Figure 4.42, Figure 4.44 and Figure 4.46. It is observed that the 2D axisymmetric modeling delivers an inconsistent trend at low working current and high inlet flow rate. A possible reason is that the fluctuating flow characteristics are damped in the steady modeling. The study delivers a more reasonable current density distribution than the 2D axisymmetric modeling.

Regression analysis is used to correlate working current and inlet flow rate with thermal and flow characteristics as illustrated in Figure 4.41, Figure 4.43, Figure 4.45 and Figure 4.47. From the fitting equation given in Figure 4.41, the working current is negatively correlated with the arc length, and the inlet flow rate is positively correlated with the arc length, where the working current more significantly impacts the arc length than the inlet flow rate. From the fitting equation given in Figure 4.43, the inlet flow rate more effectively influences on V_a^m than the working current. From the fitting equation given in Figure 4.45, V_t^m is more sensitive to the inlet flow rate. The arc length is mainly governed by the working current whereas the flow characteristics at

doi:10.6342/NTU202104312

the outlet is mainly governed by the inlet flow rate. From the fitting equation given in Figure 4.47, the influence of working current and inlet flow rate on the mean temperature at the outlet are nearly equally important. The mean temperature at the outlet is contributed by the arc heating and convective heat transfer. With the same inlet flow rate, a higher working current means a shorter arc length, and the mean temperature at the outlet reduce because of a long cooling distance from the anode to the outlet.

In this study, the cathode spot periodically circulates at a fixed axial location, and the anode is assumed to be a ring region in the torch as shown in Figure 3.2. From the FFT analysis shown in Figure 4.20 and Figure 4.37, the peak frequencies of voltage drop are found different from the circulating frequency of the cathode spot. This behavior is explained by the fact that the velocity and temperature fields are unable to keep up with the changing electromagnetic field.

doi:10.6342/NTU202104312

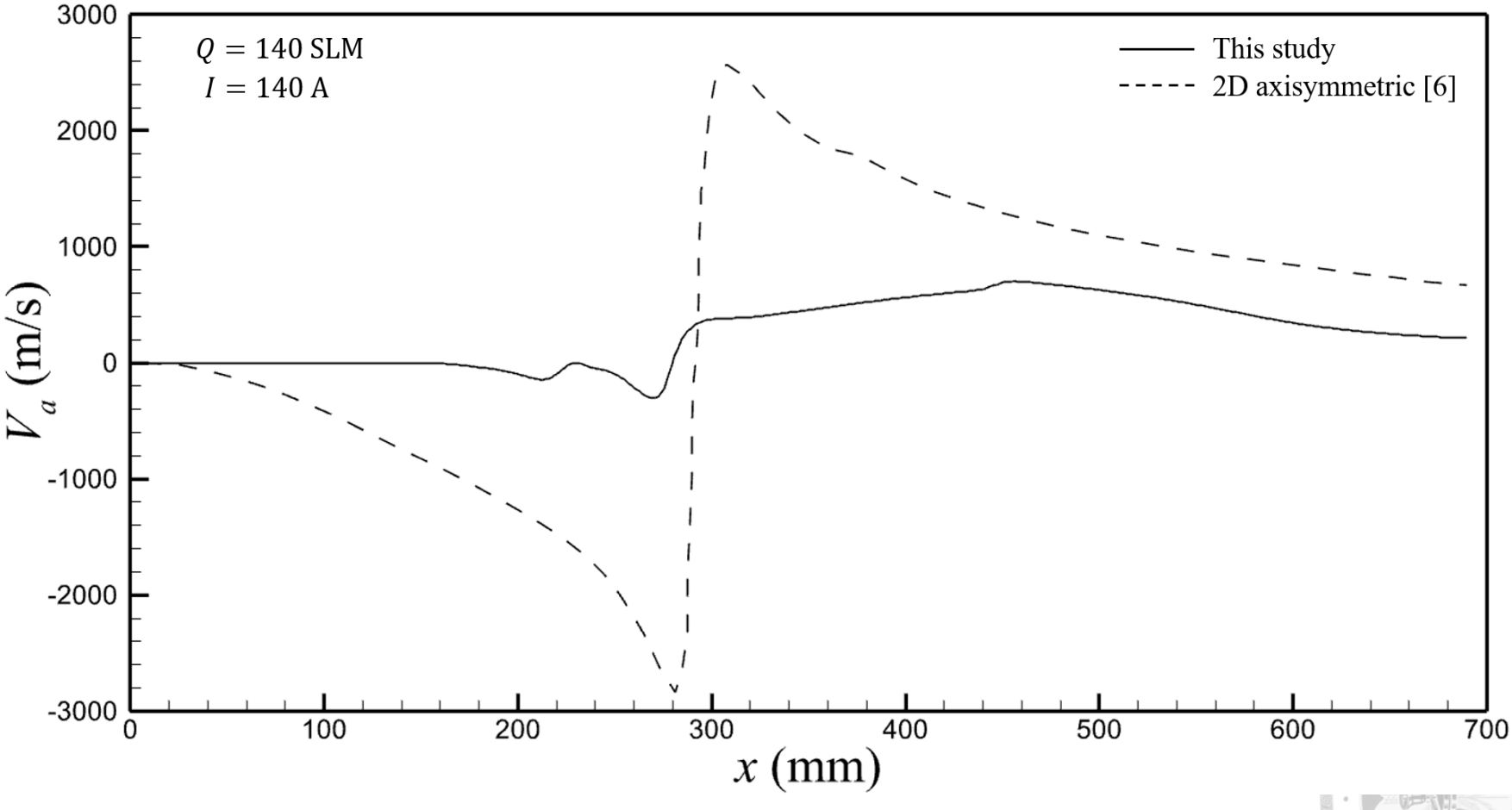


Figure 4.38: Axial velocity comparison of centerline profile predicted by two models

doi:10.6342/NTU202104312

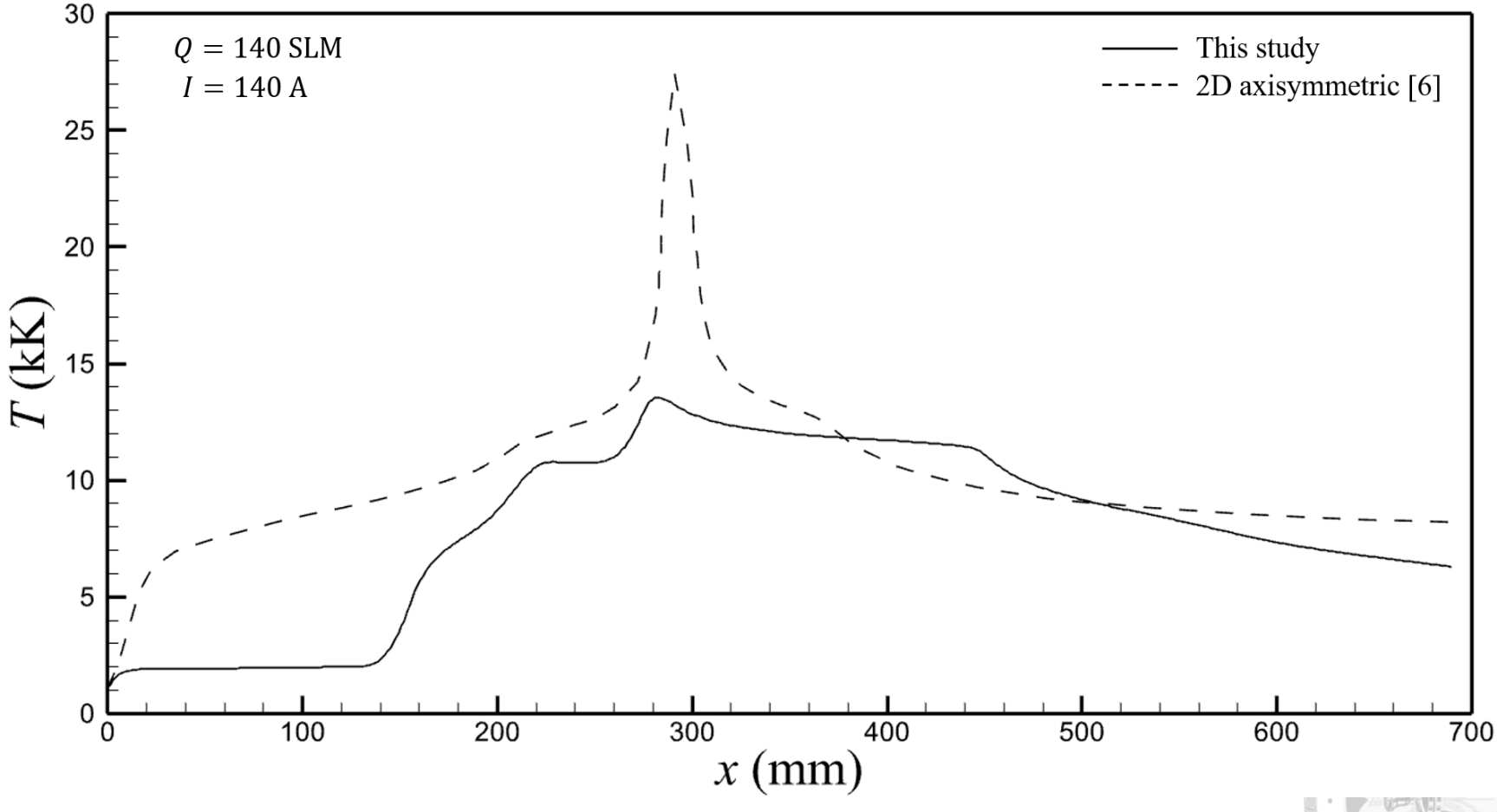


Figure 4.39: Temperature comparison of centerline profile predicted by two models

doi:10.6342/NTU202104312

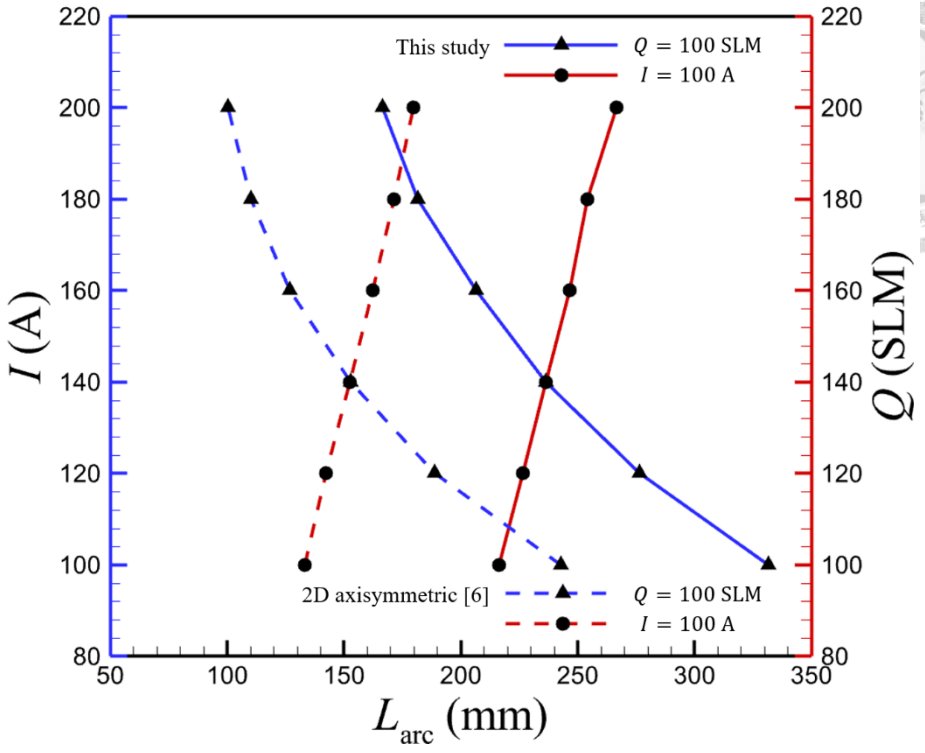


Figure 4.40: Comparison of arc length predicted by two models under different conditions

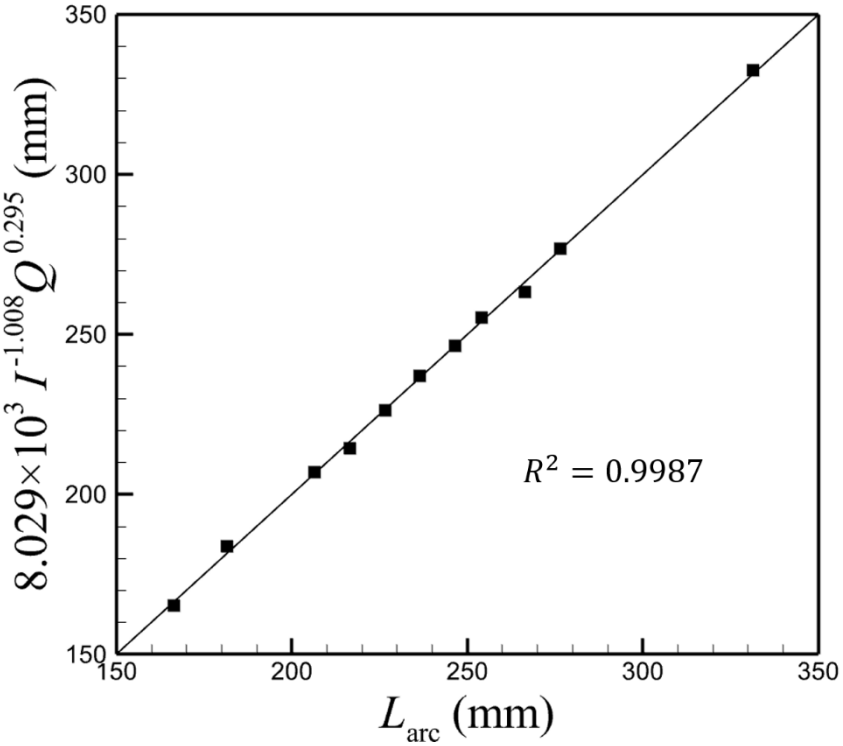


Figure 4.41: Regression correlation of arc length

doi:10.6342/NTU202104312

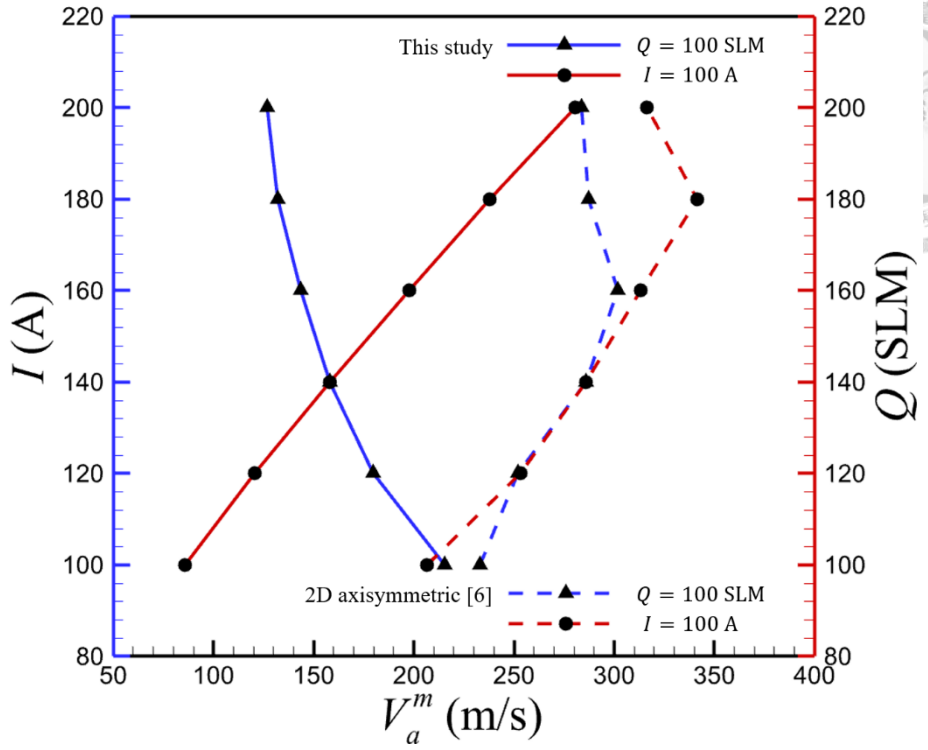


Figure 4.42: Comparison of the mean axial velocity at the outlet predicted by two models under different conditions

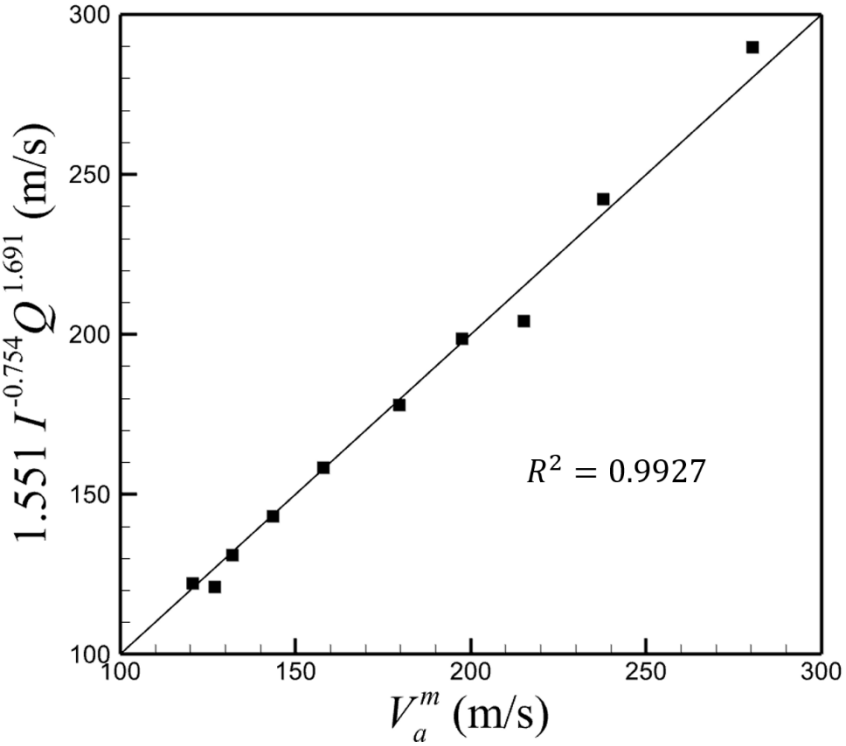


Figure 4.43: Regression correlation of the mean axial velocity at the outlet

doi:10.6342/NTU202104312

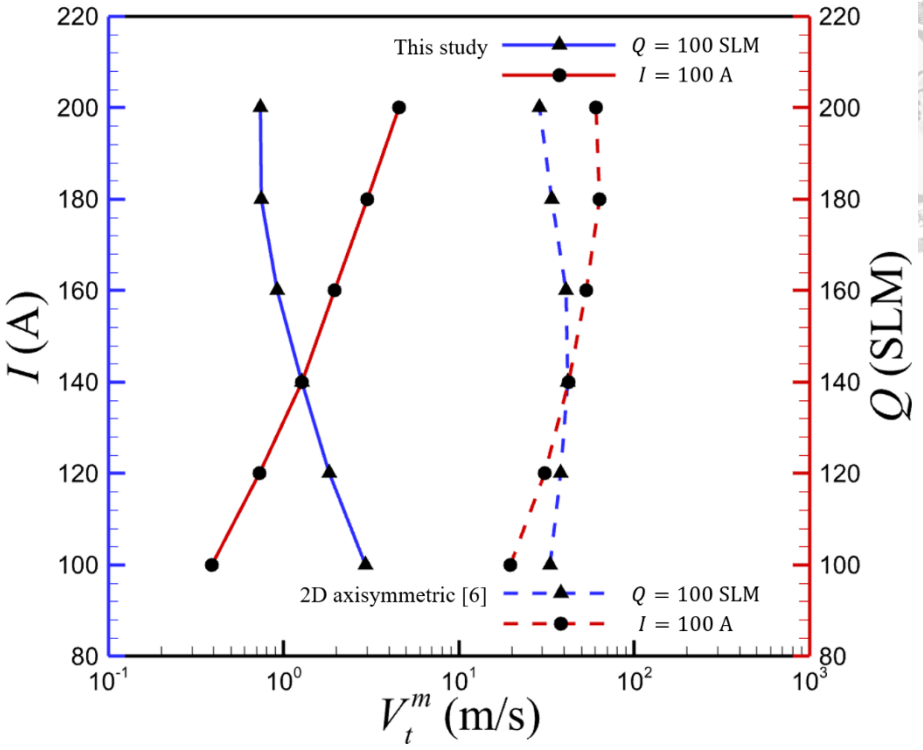


Figure 4.44: Comparison of the mean tangential velocity at the outlet predicted by two models under different conditions

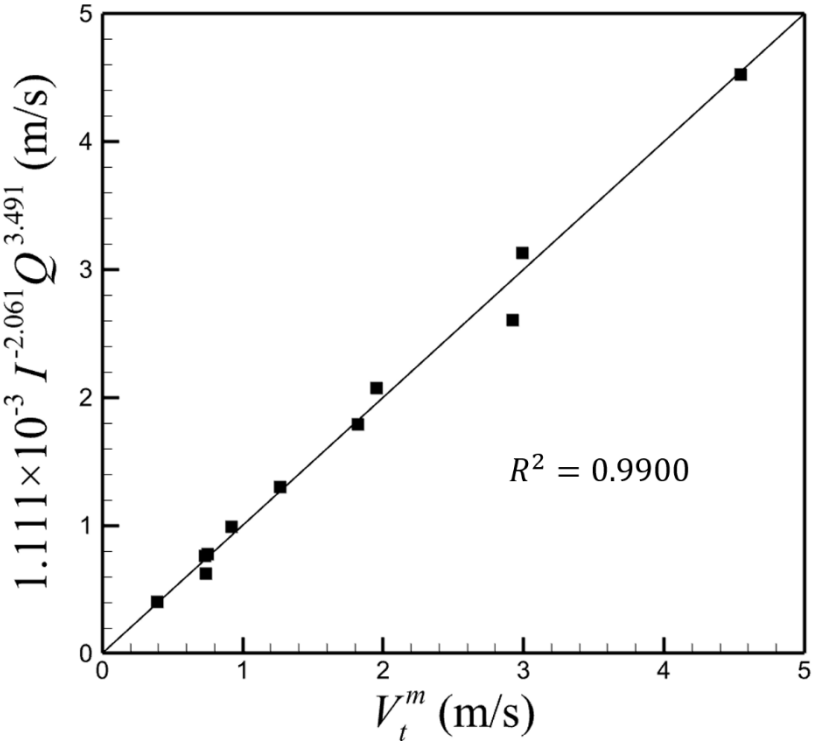


Figure 4.45: Regression correlation of the mean tangential velocity at the outlet

doi:10.6342/NTU202104312

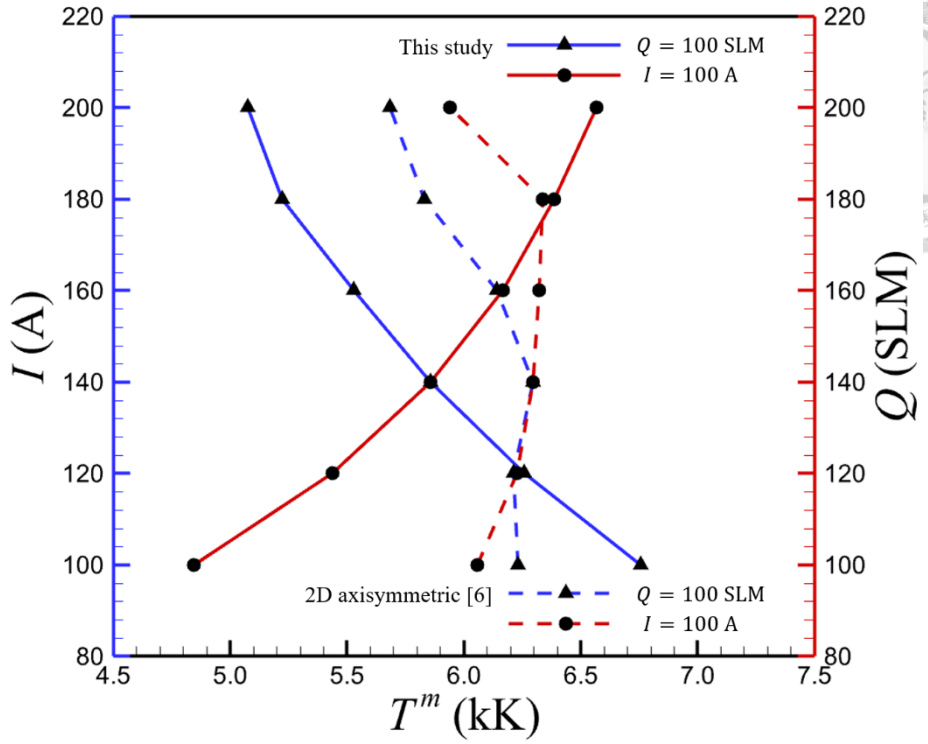


Figure 4.46: Comparison of the mean temperature at the outlet predicted by two models under different conditions

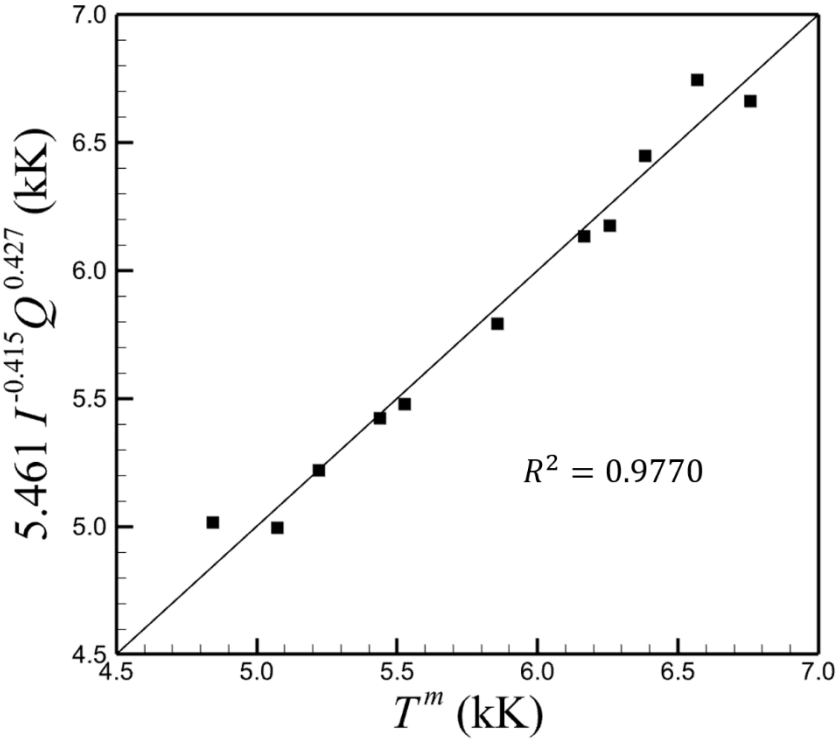


Figure 4.47: Regression correlation of the mean temperature at the outlet

doi:10.6342/NTU202104312

Chapter 5 Conclusions and Future Works

This study develops a numerical framework of unsteady 3D MHD modeling to simulate the fluid flow of the DC plasma torch equipped with WTC. A finite volume method is employed to discretize the MHD equations in the computational domain which is defined by the geometry of the DC plasma torch. The cathode spot circulates with a given frequency, 1000 Hz, on the inner surface of the torch, where the ring region of the anode is determined by satisfying the measured voltage drop. The thermal plasma flow with a fixed working current $I = 140$ A as well as a fixed inlet flow rate $Q = 140$ SLM are analyzed. The time-averaged results apparently reveal that the maximum temperature and current density occur beneath of the inlet, and the axial velocity has a maximum value beneath the anode. Regression analysis is adopted to correlate the working conditions with the thermal and flow behavior at the outlet. The arc length is predicted to grow with the working current to the power of -1.008 and the inlet flow rate to the power of 0.295; the mean axial velocity at the outlet is predicted to grow with the working current to the power of -0.754 and the inlet flow rate to the power of 1.691; the mean tangential velocity at the outlet is predicted to grow with the working current to the power of -2.061 and the inlet flow rate to the power of 3.491; the mean temperature at the outlet is predicted to grow with the working current to the power of

doi:10.6342/NTU202104312

-0.415 and the inlet flow rate to the power of 0.427. In conclusion, the inlet flow rate has larger influence on the thermal and flow behavior at the outlet than the working current. The time history analysis and the FFT analysis demonstrate that the frequencies of voltage drop are different from that of the cathode spot and mainly influenced by the working current. Besides, the voltage drop oscillation is observed in cases of low working current and high inlet flow rate.

Future studies are suggested to examine the impact of the frequency of the cathode spot, the time step size, the shape of the torch and the working gas, etc. Although the code developed in this study delivers good performance in solving unsteady DC plasma torch problem, there is still room for further improvements such as the further reduction of computational time and memory demand. Other topics, such as non-LTE and reactive flows are also possible extensions of this study.

doi:10.6342/NTU202104312

Appendix

Appendix I

Constants of the adopted SST $k-\omega$ turbulence model

σ_k	$F_1\sigma_{k_1}+(1-F_1)\sigma_{k_2}$	σ_ω	$F_1\sigma_{\omega_1}+(1-F_1)\sigma_{\omega_2}$
σ_{k_1}	0.85	σ_{ω_1}	0.5
σ_{k_2}	1	σ_{ω_2}	0.856
P_k	$\mu_t S^2$	P_ω	$\rho\gamma_\omega S^2+2\rho(1-F_1)\sigma_{\omega_2}\frac{\nabla k\cdot\nabla\omega}{\omega}$
β^*	$F_1\beta_1^*+(1-F_1)\beta_2^*$	β	$F_1\beta_1+(1-F_1)\beta_2$
β_1^*	0.09	β_1	0.075
β_2^*	0.09	β_2	0.828
f_{β^*}	1	f_β	1
T_t	$\min\left(\frac{\alpha^*}{\omega},\frac{\mathrm{a}_1}{S\,F_2}\right)$	F_2	$\tanh\left(\left[\max\left(\frac{2\sqrt{k}}{\beta^* d\omega},\frac{500\nu}{d^2\omega}\right)\right]^2\right)$
α^*	$F_1\alpha_1^*+(1-F_1)\alpha_2^*$	$\mathrm{CD}_{k\omega}$	$\max\left(\frac{\nabla k\cdot\nabla\omega}{\omega},10^{-20}\right)$
α_1^*	1	κ	0.41
α_2^*	1	E'	9.0
a_1	0.31	C_μ	0.09
S	$\left\|\frac{1}{2}(\nabla\mathbf{v}+\nabla\mathbf{v}^T)\right\|$		

doi:10.6342/NTU202104312

Appendix II

Control parameters and constants

$\widehat{\sum \dot{m}}^{*}$	10^{-4}
n_i	50
Δt (s)	$2 \cdot 10^{-5}$
$\omega_{\mathbf{v}}$	0.7
ω_p	0.3
ω_t	0.8
ω_E	0.5
ω_ϕ	1
$\omega_{\mathbf{A}}$	0.99
μ_0 (H/m)	$1.25664 \cdot 10^{-6}$
Pr_t	0.9
I_t	0.01
$(\mu_t/\mu_m)_{\text{in}}$	10

doi:10.6342/NTU202104312

References

[1] B. Selvan, K. Ramachandran, K. Sreekumar, T. Thiyagarajan, and P. Ananthapadmanabhan, "Numerical and experimental studies on DC plasma spray torch," *Vacuum,* vol. 84, no. 4, pp. 444-452, 2009.

[2] 徐少駒，*在不同背壓條件下非傳輸型井式陰極直流空氣電漿火炬內部流場模擬*，國立臺灣科技大學機械工程系碩士論文，2013。

[3] M. Hur and S. H. Hong, "Comparative analysis of turbulent effects on thermal plasma characteristics inside the plasma torches with rod-and well-type cathodes," *Journal of Physics D: Applied Physics,* vol. 35, no. 16, p. 1946, 2002.

[4] K. S. Kim, J. M. Park, S. Choi, J. Kim, and S. H. Hong, "Comparative study of two-and three-dimensional modeling on arc discharge phenomena inside a thermal plasma torch with hollow electrodes," *Physics of Plasmas,* vol. 15, no. 2, p. 023501, 2008.

[5] Z. Pan, L. Ye, S. Qian, Q. Sun, C. Wang, T. Ye, and W. Xia, "Comparison of Reynolds average Navier–Stokes turbulence models in numerical simulations of the DC arc plasma torch," *Plasma Science and Technology,* vol. 22, no. 2, 2020.

[6] J. Bauchire, J. Gonzalez, and A. Gleizes, "Modeling of a DC plasma torch in laminar and turbulent flow," *Plasma Chemistry and Plasma Processing,* vol. 17, no. 4, pp. 409-432, 1997.

doi:10.6342/NTU202104312

[7] S. W. Chau, C. M. Tai, and S. H. Chen, "Nonequilibrium modeling of steam plasma in a nontransferred direct-current torch," *IEEE Transactions on Plasma Science,* vol. 42, no. 12, pp. 3797-3808, 2014.

[8] V. Frolov, I. Murashov, and D. Ivanov, "Special aspects of dc air plasma torch's operating modes under turbulent flow conditions," *Plasma Physics and Technology Journal,* vol. 2, pp. 129-133, 2015.

[9] D. Scott, P. Kovitya, and G. Haddad, "Temperatures in the plume of a dc plasma torch," *Journal of Applied Physics,* vol. 66, no. 11, pp. 5232-5239, 1989.

[10] J. Coudert, M. Planche, and P. Fauchais, "Characterization of dc plasma torch voltage fluctuations," *Plasma Chemistry and Plasma Processing,* vol. 16, no. 1, pp. S211-S227, 1995.

[11] B. Selvan and K. Ramachandran, "Comparisons between two different three-dimensional arc plasma torch simulations," *Journal of Thermal Spray Technology,* vol. 18, no. 5, pp. 846-857, 2009.

[12] K. S. Kim, J. M. Park, S. Choi, J. Kim, and S. H. Hong, "Enthalpy probe measurements and three-dimensional modelling on air plasma jets generated by a non-transferred plasma torch with hollow electrodes," *Journal of Physics D: Applied Physics,* vol. 41, no. 6, p. 065201, 2008.

[13] R. Huang, H. Fukanuma, Y. Uesugi, and Y. Tanaka, "An improved local thermal equilibrium model of DC arc plasma torch," *IEEE Transactions on Plasma Science,* vol. 39, no. 10, pp. 1974-1982, 2011.

doi:10.6342/NTU202104312

[14] J. Trelles, J. Heberlein, and E. Pfender, "Non-equilibrium modelling of arc plasma torches," *Journal of Physics D: Applied Physics,* vol. 40, no. 19, p. 5937, 2007.

[15] J. M. Park, K. S. Kim, T. H. Hwang, and S. H. Hong, "Three-dimensional modeling of arc root rotation by external magnetic field in nontransferred thermal plasma torches," *IEEE Transactions on Plasma Science,* vol. 32, no. 2, pp. 479-487, 2004.

[16] J. L. Dorier, M. Gindrat, C. Hollenstein, A. Salito, M. Loch, and G. Barbezat, "Time-resolved imaging of anodic arc root behavior during fluctuations of a DC plasma spraying torch," *IEEE Transactions on Plasma Science,* vol. 29, no. 3, pp. 494-501, 2001.

[17] Z. Duan and J. Heberlein, "Arc instabilities in a plasma spray torch," *Journal of Thermal Spray Technology,* vol. 11, no. 1, pp. 44-51, 2002.

[18] A. Gleizes, J. J. Gonzalez, and P. Freton, "Thermal plasma modelling," *Journal of Physics D: Applied Physics,* vol. 38, no. 9, p. R153, 2005.

[19] M. I. Boulos, P. Fauchais, and E. Pfender, *Thermal plasmas: fundamentals and applications*. Springer Science & Business Media, 2013.

[20] V. Rat, A. Murphy, J. Aubreton, M.-F. Elchinger, and P. Fauchais, "Treatment of non-equilibrium phenomena in thermal plasma flows," *Journal of Physics D: Applied Physics,* vol. 41, no. 18, p. 183001, 2008.

doi:10.6342/NTU202104312

[21] M. J. Ni, R. Munipalli, N. B. Morley, P. Huang, and M. A. Abdou, "Validation case results for 2D and 3D MHD simulations," *Fusion Science and Technology,* vol. 52, no. 3, pp. 587-594, 2007.

[22] L. Niemeyer and K. Ragaller, "Development of turbulence by the interaction of gas flow with plasmas," *Zeitschrift für Naturforschung A,* vol. 28, no. 8, pp. 1281-1289, 1973.

[23] M. Shigeta, "Turbulence modelling of thermal plasma flows," *Journal of Physics D: Applied Physics,* vol. 49, no. 49, 2016.

[24] F. R. Menter, "Two-equation eddy-viscosity turbulence models for engineering applications," *AIAA Journal,* vol. 32, no. 8, pp. 1598-1605, 1994.

[25] D. C. Wilcox, *Turbulence modeling for CFD*. DCW industries La Canada, CA, 1998.

[26] B. E. Launder and D. B. Spalding, "Lectures in mathematical models of turbulence," 1972.

[27] J. l. Xu, H. Y. Ma, and Y. N. Huang, "Nonlinear turbulence models for predicting strong curvature effects," *Applied Mathematics and Mechanics,* vol. 29, no. 1, pp. 31-42, 2008.

[28] P. Durbin, "On the k-ε stagnation point anomaly," *Int. J. Heat and Fluid Flow,* vol. 17, pp. 9-90, 1996.

[29] S. Kenjereš, S. Gunarjo, and K. Hanjalić, "Contribution to elliptic relaxation modelling of turbulent natural and mixed convection," *International Journal of Heat and Fluid Flow,* vol. 26, no. 4, pp. 569-586, 2005.

doi:10.6342/NTU202104312

[30] R. Bolot, V. Monin, M. Imbert, and C. Coddet, "Mathematical modeling of a plasma jet impinging on a flat structure," in *Thermal Spray: Meeting the Challenges of the 21st Century*, 1998, pp. 439-444.

[31] T. Craft, A. Gerasimov, H. Iacovides, and B. Launder, "Progress in the generalization of wall-function treatments," *International Journal of Heat and Fluid Flow,* vol. 23, no. 2, pp. 148-160, 2002.

[32] J. H. Ferziger, M. Perić, and R. L. Street, *Computational methods for fluid dynamics*. Springer, 2002.

[33] E. Fares and W. Schröder, "A differential equation for approximate wall distance," *International Journal for Numerical Methods in Fluids,* vol. 39, no. 8, pp. 743-762, 2002.

[34] P. G. Tucker, "Differential equation-based wall distance computation for DES and RANS," *Journal of Computational Physics,* vol. 190, no. 1, pp. 229-248, 2003.

[35] F. Moukalled, L. Mangani, and M. Darwish, *The finite volume method in computational fluid dynamics*. Springer, 2016.

[36] P. G. Tucker, C. L. Rumsey, P. R. Spalart, R. E. Bartels, and R. T. Biedron, "Computations of wall distances based on differential equations," *AIAA Journal,* vol. 43, no. 3, pp. 539-549, 2005.

[37] Plasma Taiwan Innovation Corporation. http://www.plasmati.com.tw (accessed 10/27, 2021).

doi:10.6342/NTU202104312

[38] D. L. Lin, S. H. Chen, and C. C. Tzeng, "Characteristics of a Non-Transferred Plasma Torch Operated in a Positive Pressure Environment", *INER-8651R,* 2011. (in Chinese)

[39] M. Benilov and A. Marotta, "A model of the cathode region of atmospheric pressure arcs," *Journal of Physics D: Applied Physics,* vol. 28, no. 9, p. 1869, 1995.

[40] Y. P. Raizer and J. E. Allen, *Gas discharge physics*. Springer Berlin, 1997.

[41] C. Kimblin, "Erosion and ionization in the cathode spot regions of vacuum arcs," *Journal of Applied Physics,* vol. 44, no. 7, pp. 3074-3081, 1973.

[42] V. Aubrecht and M. Bartlova, "Net emission coefficients of radiation in air and SF6 thermal plasmas," *Plasma Chemistry and Plasma Processing,* vol. 29, no. 2, pp. 131-147, 2009.

[43] L. F. Richardson, "The approximate arithmetical solution by finite differences of physical problems involving differential equations, with an application to the stresses in a masonry dam," *Philosophical Transactions of the Royal Society of London. Series A, Containing Papers of a Mathematical or Physical Character,* vol. 210, no. 459-470, pp. 307-357, 1911.

[44] K. Hsu, K. Etemadi, and E. Pfender, "Study of the free-burning high-intensity argon arc," *Journal of applied physics,* vol. 54, no. 3, pp. 1293-1301, 1983.

doi:10.6342/NTU202104312